The Novel Two-Dimensional van der Waals Crystal InSe and its Magnetic Doping

Mahabub Alam Bhuiyan

Thesis submitted to the University of Nottingham
for the degree of Doctor of Philosophy
February 2019

Abstract

This thesis focusses on the electronic properties of the novel two dimensional (2D) van der Waals (vdW) crystal InSe. It examines the integration of InSe in graphene-based field effect transistors (FETs) and the incorporation of transition metals in InSe to create new magnetic materials.

InSe is employed in graphene-based FETs as an electrically and optically active capping layer to "modulation-dope" and photosensitise an adjacent graphene layer. This leads to a "giant" quantum Hall (QH) plateau at a filling factor $\nu = 2$ in the magnetoresistance of graphene that persists over a wide range of magnetic fields. Furthermore, the optical excitation of the FETs changes the resistance of the graphene layer. The sign of the Hall voltage and of the $\nu = 2$ QH plateau persists over a wide range of temperatures of up to $T \sim$ 200K and can be controlled by an appropriate combination of gate voltages and optical illumination. These phenomena involve the charge transfer at the InSe/graphene interface, offering opportunities for optoelectronics and quantum metrology.

Also, we studied a new hybrid material system, which comprises InSe and ferromagnetic Fe-islands. We observed that unlike many traditional semiconductors, the electronic properties of pristine InSe are largely preserved after the incorporation of Fe. Also, this system exhibits ferromagnetic resonances and a large uniaxial magnetic anisotropy at room temperature, offering opportunities for the development of functional devices that integrate magnetic and semiconducting properties within the same material system.

Acknowledgments

First and foremost, I would like to express my heartfelt gratitude to my supervisor Professor Amalia Patanè. Her guidance, strong support and motivation encouraged me to carry out my PhD research successfully. I am incredibly grateful for the valuable time and enormous patience that she has invested on me throughout the last three years. I will never forget these years and will always be proud that I was her student.

Secondly, my deepest gratitude goes to my supervisor Dr. Oleg Makarovsky. Every discussion with Oleg helped me to understand and overcome difficulties encountered during the measurements. Without his indispensable supports and suggestions, this work would have not been possible.

I am extremely grateful to Prof. Laurence Eaves for useful discussions regarding some theoretical aspects of my work on the quantum Hall effect.

I am very grateful to Dr. Zakhar R. Kudrynskyi and Dr. Fabrizio Moro for their kind and cooperative supports throughout this work, and continuous guidance during the fabrication of the samples and their study by different experimental techniques. Also, I would like to thank my dear co-workers, friends and visitors of the Wendy house, Dr. Lyudmila Turyanska, Dr. Nilanthy Balakrishnan, Dr. Anton Velychko, Dr. Natalia Alexeeva, Garry W. Mudd, Davide Maria Di Paola, Jake D. G. Greener, Debarati Mazumder, Chengxi Zhang, Nathan Cottam, J. Sutcliffe, Dr. Evgenii Vdovin and Masahiro Matsuura for all the good times and discussions that I had with them.

I would like to express my sincere gratitude to Prof. P. H. Beton, Dr. C. J. Mellor, Dr. M. Wang, D. Pattnaik, Dr. V. Korolkov, J. Chauhan, D. Tylor, C.

R. Staddon; Dr. M. W. Fay, Dr. C. Parmenter, Dr. E. Steer (Nanoscale and Microscale Research Centre, The University of Nottingham) for their invaluable supports.

I would like to acknowledge our collaborators, Prof. K. S. Novoselov, Dr. Y. Cao, Dr. A. Mishchenko, Dr. A. J. Fielding, M. Nazarova (The University of Manchester); R. Puttock, Dr. O. Kazakova (National Physical Laboratory); Dr. B. A. Piot, Dr. I. I. Lobanova (Laboratoire National des Champs Magnétiques Intenses Grenoble); Prof. J. van Slageren, M. Kern (Universität Stuttgart); Prof. Z. D. Kovalyuk (Institute for Problems of Materials Science at the National Academy of Sciences of Ukraine); Dr. G. Yusa (Tohoku University); A. J. Marsden, Dr. N. R. Wilson (University of Warwick) for their supports.

I express my sincere thanks to the staff members, C. Pallender, S. Taak, Dr. P. Hawker, M. Parker, W. Brennan, M. Stretton, M. Thomas, D. Bonnar, A. Gasiorowska, P. Davies, S. Warburton for technical, administrative and financial support.

I acknowledge the support of The University of Nottingham, Engineering and Physical Sciences Research Council (EPSRC), EU Graphene Flagship project and the Commonwealth Scholarship Commission.

I would like to express my heartfelt gratitude to my parents and younger brother for their encouragements, and continuous support to my wife and son in my absence. My deepest thank goes to my wife Mehenaz Tabassum. Without her understanding and self-sacrificing help, it would have not been possible to continue my study. Finally, I would like to thank my lovely son Rashdan

Bhuiyan Nokkhotro for his long waiting. I deeply appreciate both their endurance and patience.

List of publications

1. Z. R. Kudrynskyi, M. A. Bhuiyan, O. Makarovsky, J. D. G. Greener, E. E. Vdovin, Z. D. Kovalyuk, Y. Cao, A. Mishchenko, K. S. Novoselov, P. H. Beton, L. Eaves, A. Patanè, "Giant quantum Hall plateau in graphene coupled to an InSe van der Waals crystal", *Physical Review Letters* **119**, 157701 (2017).

2. F. Moro, M. A. Bhuiyan, Z. R. Kudrynskyi, R. Puttock, O. Kazakova, O. Makarovsky, M. W. Fay, C. Parmenter, Z. D. Kovalyuk, A. J. Fielding, M. Kern, J. van Slageren, A. Patanè, "Room temperature uniaxial magnetic anisotropy induced by Fe-islands in the InSe semiconductor van der Waals crystal", *Advanced Science* **5**, 1800257 (2018).

3. M. A. Bhuiyan, Z. R. Kudrynskyi, D. Mazumder, J. D. G. Greener, O. Makarovsky, C. J. Mellor, E. E. Vdovin, B. A. Piot, I. I. Lobanova, Z. D. Kovalyuk, M. Nazarova, A. Mishchenko, K. S. Novoselov, Y. Cao, L. Eaves, G. Yusa, A. Patanè, "Photoquantum Hall effect and light-induced charge transfer at the interface of graphene/InSe heterostructures", *Advanced Functional Materials* **29**, 1805491 (2019).

4. M. A. Bhuiyan, J. Sutcliffe, Z. R. Kudrynskyi, O. Makarovsky, Z. D. Kovalyuk, L. Eaves, Amalia Patanè, "Band gap bowing, electron-phonon interaction, and quantum confinement in $SnSe_{2(1-x)}S_{2x}$ van der Waals alloys". (In preparation)

5. Weak localisation and Coulomb scattering in InSe/graphene heterostructures. (In preparation)

List of conference abstracts

1. Z. R. Kudrynskyi, M. A. Bhuiyan, F. Moro, O. Makarovsky, Z. D. Kovalyuk, L. Eaves, P. H. Beton, M. W. Fay, M. Matsuura, A. Patanè, Magnetic and semiconducting properties in van der Waals InSe layered crystals incorporating transition metals. *Graphene Week 2016*, Warsaw, Poland, 13-17 June, (2016).

2. M. A. Bhuiyan, F. Moro, Z. R. Kudrynskyi, O. Makarovsky, M. W. Fay, C. Parmenter, Z. D. Kovalyuk, A. Patanè, Magnetic and non-magnetic two-dimensional van der Waals InSe crystals. *Graphene Week 2017*, Athens, Greece, 25-29 September, (2017).

3. M. A. Bhuiyan, F. Moro, Z. R. Kudrynskyi, R. Puttock, O. Kazakova, O. Makarovsky, M. W. Fay, C. Parmenter, Z. D. Kovalyuk, A. J. Fielding, M. Kern, J. V. Slageren, A. Patanè, Fe-induced magnetism in van der Waals InSe semiconductor crystals. *UK Semiconductors 2018*, Sheffield, United Kingdom, 4-5 July, (2018).

4. M. A. Bhuiyan, F. Moro, Z. R. Kudrynskyi, R. Puttock, O. Kazakova, O. Makarovsky, M.W. Fay, C. Parmenter, Z. D. Kovalyuk, A. J. Fielding, M. Kern, J. V. Slageren, A. Patanè, Fe-induced magnetism in van der Waals InSe semiconductor crystals. *ICPS 2018-34th International Conference on the Physics of Semiconductors*, Montpellier, France, 29 July-03 August, (2018).

5. M. A. Bhuiyan, F. Moro, Z. R. Kudrynskyi, R. Puttock, O. Kazakova, O. Makarovsky, M.W. Fay, C. Parmenter, Z. D. Kovalyuk, A. J. Fielding, M. Kern, J. V. Slageren, A. Patanè, Fe-induced magnetism in van der Waals InSe semiconductor crystals. *Graphene Week 2018*, San Sebastian, Spain, 10-14 September, (2018).

Physical constants

Quantity	Symbol	Value	Unit
Boltzmann constant	k_B	1.38065×10^{-23}	JK^{-1}
Electron charge	e	1.60218×10^{-19}	C
Electron mass in vacuum	m_e	9.10938×10^{-31}	kg
Permittivity in vacuum	ε_0	8.85419×10^{-12}	Fm^{-1}
Planck constant	h	6.62607×10^{-34}	Js
Reduced Planck constant ($h/2\pi$)	$\hbar$	1.05457×10^{-34}	Js
Speed of light in vacuum	c	2.99792×10^{8}	ms^{-1}

List of Contents

Chapter 1

Introduction

For many decades, semiconductor materials such as Si and III-V compounds have been at the heart of condensed matter physics research and several technologies. However, since traditional Si-based devices have now reached the scaling limit, scientists are looking for a new class of materials, which can create new routes to digital electronics beyond Moore's law,[1] spintronics, quantum optics for fast, secure communications, and quantum detection and imaging for sensing applications.[2] After the discovery of graphene in 2004,[3] it was believed that graphene could replace Si in many technologies due to its exceptional properties, such as massless Dirac fermions, linear energy dispersion, truly two-dimensional (2D) nature, high carrier mobilities, *etc.*[4] However, the gapless nature of pristine graphene and poor photoresponsivity make graphene unsuitable for digital electronics and optoelectronics.[5,6] Several strategies have been explored to overcome these limitations.[7-9] In particular, this has also led to the investigation of new graphene-like 2D van der Waals (vdW) layered materials such as the wide-gap insulator hexagonal boron nitride (hBN),[10,11] the narrow band gap semiconductor black phosphorus (bP)[12,13] and transition metal dichalcogenides (TMDCs, *e.g.* MoS_2, WS_2, *etc*.).[14,15] Among these, metal chalcogenides (InSe, In_2Se_3, GaSe, *etc.*)[16-20] have attracted wide interest and enriched the current library of 2D materials.[11,21] In these layered materials, the weak interlayer interactions make possible to isolate either single or few layers by mechanical[22] or chemical[23,24] exfoliation.

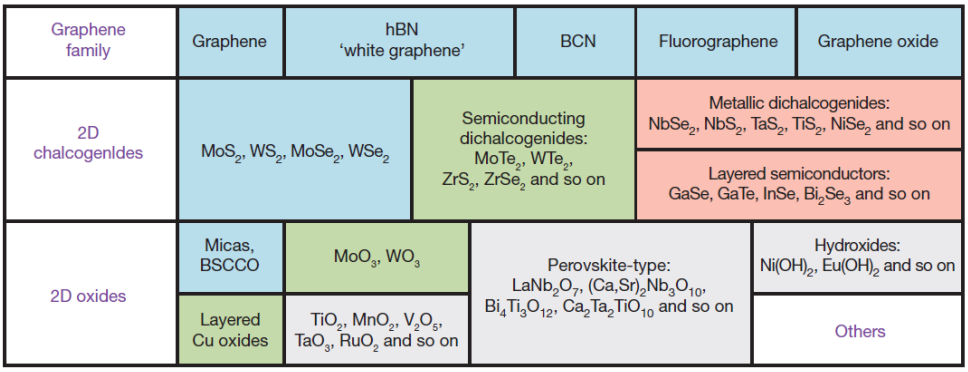

Figure 1.1 Current 2D library. Monolayers that are stable under ambient conditions are shaded in blue; those probably stable in air are shaded in green; and those unstable in air but that may be stable in inert atmosphere are shaded in pink. Recent studies showed that cleaved InSe surface is chemically stable under ambient conditions Ref [25]. Gray shading indicates 3D compounds that have been successfully exfoliated down to monolayers. After intercalation and exfoliation, the oxides and hydroxides may exhibit stoichiometry different from their 3D parents. 'Others' indicates that many other 2D crystals (including borides, carbides, nitrides *etc.*) have been or can be isolated. Figure adapted from Ref [10].

Along with fundamental research on graphene and graphene-like 2D materials, different techniques have been developed to fabricate or grow stable films down to the monolayer thickness and transfer them on specific substrates. Recent advances have enabled the fabrication of vdW heterostructures by stacking different layered materials,[26-28] thus overcoming limitations of traditional semiconductor heterojunctions, such as incompatibility of the active layer and substrate due to lattice mismatch, defective interfaces, *etc.*[10] In these heterostructures, the in-plane stability of the 2D crystals arises from the strong covalent bonds, whereas the multiple stacks remain together due to the weak vdW forces.[10] The electronic properties of these heterostructures can be modified by the careful selection of stacking materials, built-in strain and relative orientation of the layers.[29] These atomically thin layers and their heterostructures offer unique opportunities to explore novel band structures, and manipulate the transfer of electronic charge at the interface of different

materials, offering prospects for fundamental and applied research and the realisation of high-performance multi-functional devices for photonics and electronics.[11] An interesting aspect of current research is the controlled manipulation of the spin and charge of electrons in a 2D semiconductor. This can create new routes to spintronics, which can require the development of magnetic nanostructured materials that integrate both semiconducting and magnetic properties within the same crystal. To date, the integration of magnetic properties within a semiconductor crystal has proven to be challenging. Attempts to create magnetic semiconductors have often led to a significant deterioration of the crystal quality, but also led to material systems with new interesting magnetic and electronic properties.[30-32]

Among the current 2D materials, the "post-transition" metal monochalcogenide InSe has received increasing attention because of its small in-plane electron effective mass,[33] tuneable band gap,[34] high photoresponsivity with a broad spectral range from the near infra-red to the visible region,[29,35] and large current on/off ratios ($\approx 10^8$)[36] and high electron mobilities ($\sim 10^3$ cm^2/Vs)[17] at room temperature. Furthermore, along with the compatibility of InSe with other materials, this 2D crystal possesses unique features: it has an almost flat, slightly inverted 'Mexican-hat' valence band dispersion with one dimensional van Hove singularities in the density of states,[37] offering exciting opportunities to explore strong correlation phenomena[18] and phase instabilities, such as ferromagnetism.[38] The interaction and band alignment between InSe and other 2D layers, dielectric screening, electron-phonon interactions, *etc.* are still largely unknown. However, the lack of dangling bonds in stacked layers could

enable the realisation of new structures and the investigation of new phenomena.

Motivated from this burgeoning research, one of the objectives of my PhD project was to fabricate and investigate InSe/graphene heterostructures and their integration in graphene-based field effect transistors (FETs). Of particular interest is the charge transfer at the interface between InSe and graphene, and the controlled modification of the electronic properties of graphene. This has led to the discovery of a "giant" quantum Hall plateau in the magnetoresistance of InSe-capped graphene. Another aim of this project was to explore the doping of InSe with transition metals. This has led to the discovery of a new hybrid material system, which comprises InSe and ferromagnetic Fe-inclusions. This new system possesses room temperature ferromagnetism with a large uniaxial magnetic anisotropy perpendicular to the plane of the vdW layers. Also, it preserves the semiconducting properties of pristine InSe.

1.1 Thesis overview

This thesis is organized as follows:

Chapter 2 provides a review of the literature on different 2D materials, highlighting the unique properties and key findings on graphene and InSe. Also, it includes a review of recent works on low dimensional magnetic semiconductors.

Chapter 3 presents the theory and basic principles underlying the original work presented in this thesis. We start with discussing the theory of electronic transport in 2D materials. Then we move to describe different magnetic phenomena and the basic principles of electron spin resonance.

Chapter 4 describes the sample preparation and different experimental techniques used in this work.

Chapter 5 presents the transport properties of InSe capped graphene-based FETs. A "giant" QH plateau is reported and the magnetic field and electric field effect-induced transfer of charge carriers between InSe and the adjacent graphene layer is discussed.

Chapter 6 investigates the light induced charge transfer at the InSe/graphene interface and its role on the transport properties of InSe/graphene hybrid phototransistors. A light induced sign reversal of the QH voltage and the persistence of the $h/2e^2$ QH plateau up to $T \sim 200$K are discussed.

Chapter 7 discusses the semiconducting and magnetic properties of a new hybrid material system comprising the InSe semiconductor and ferromagnetic Fe-inclusions. It focusses on the large room temperature uniaxial magnetic anisotropy and the semiconducting properties of this new magnetic system.

Chapter 8 concludes the thesis with a summary of the key results and provides an outlook for further research directions.

Chapter 2

Non-magnetic and magnetic van der Waals crystals

This chapter describes recent research on two-dimensional (2D) materials. Also, it describes recent work on low dimensional magnetic semiconductors.

2.1 Family of 2D materials

The discovery of graphene has generated huge interest in other 2D layered materials with diverge optical and electronic properties, enabling the discovery of new phenomena and the fabrication of new functional devices.[10,14,39-42] Due to the significant interest in this field, the family of 2D materials has expanded in the last decade. This section describes some of the unique properties of graphene and of the "post-transition" metal chalcogenide InSe, which are the 2D systems studied in this thesis. Other 2D materials like hBN, transition metal dichalcogenides (TMDCs) and black phosphorus (bP) are discussed briefly, but their study is beyond the scope of this thesis.

2.1.1 Graphene

Graphene consists of a single layer of carbon atoms arranged into a honey-comb structure. Each carbon atom forms σ-bonds with three nearest carbon atoms by sp^2 hybridisation and the remaining out of plane un-hybridised electronic orbital (p_z) of each atom forms a π-bond. The in-plane localised strong σ-bonds are responsible for the strength and extreme mechanical

properties of graphene, whereas the delocalised electrons in π-bonds play a critical role in the electronic properties of graphene.

The unit cell of graphene comprises of two atoms, A and B, periodically arranged in a triangular lattice with the primitive vectors in real space given by

$$\overrightarrow{a_1} = \left(\frac{\sqrt{3}a_0}{2}, \frac{a_0}{2}\right) = \frac{a}{2}(3, \sqrt{3}), \quad \text{and} \quad \overrightarrow{a_2} = \left(\frac{\sqrt{3}a_0}{2}, -\frac{a_0}{2}\right) = \frac{a}{2}(3, -\sqrt{3}), \quad (2.1)$$

where $a_0 = |\overrightarrow{a_1}| = |\overrightarrow{a_2}|$ is the lattice constant and $a = a_0/\sqrt{3}$ ≈1.42Å is the inter-atomic distance between the two sublattice sites A and B (Figure 2.1). In reciprocal space, the lattice vectors and the coordinates of the K and K' points are

$$\overrightarrow{b_1} = \frac{2\pi}{3a}(1, \sqrt{3}), \quad \overrightarrow{b_2} = \frac{2\pi}{3a}(1, -\sqrt{3}); \quad (2.2)$$

$$\vec{K} = \frac{2\pi}{3a}\left(1, \frac{\sqrt{3}}{3}\right), \qquad \overrightarrow{K'} = \frac{2\pi}{3a}\left(1, -\frac{\sqrt{3}}{3}\right). \quad (2.3)$$

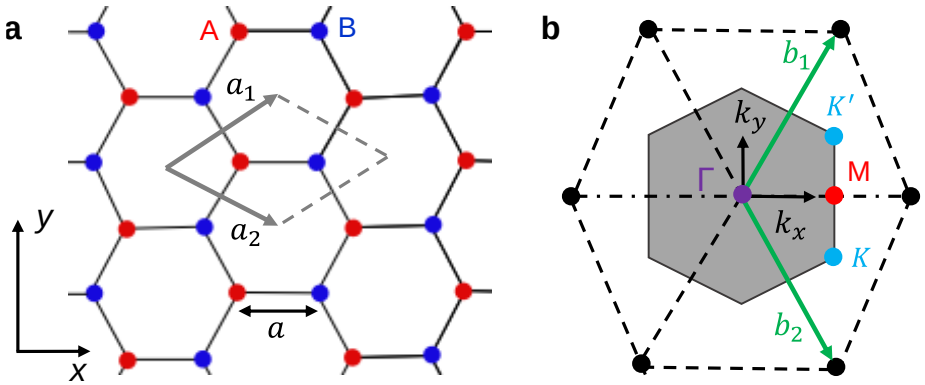

Figure 2.1 a) The honeycomb lattice structure of graphene in real space. Two sublattice sites are labelled A and B. The unit cell is marked by the lattice vectors $\vec{a}_1$ and $\vec{a}_2$. (b) The reciprocal lattice of graphene with the first Brillouin zone shaded.

In 1947, Philip Wallace calculated the band structure of graphene using the tight binding approximation.[43] The tight binding Hamiltonian is

$$\hat{H}_k = \begin{pmatrix} 0 & tS_k \\ tS_k^* & 0 \end{pmatrix}, \quad (2.4)$$

where $S_k = \sum_n e^{i\vec{k}.\vec{n}} = 2e^{-\frac{ik_x a}{2}}\cos(\frac{\sqrt{3}}{2}k_y a) + e^{ik_x a}$ and $t \sim 2.8$ eV is the hopping parameter.[44] The result of the tight-binding calculation is given by (2.5), the details derivation of which can be found elsewhere[45]

$$E_k = \pm t|S_k| = \pm t\sqrt{3 + 2\cos(\sqrt{3}k_y a) + 4\cos\left(\frac{\sqrt{3}}{2}k_y a\right)\cos(\frac{3}{2}k_x a)}. \quad (2.5)$$

Using (2.5), one can draw the band structure of graphene, as shown in Figure 2.2. The conduction band minima touch the valence band maxima at six corners (K and K') known as "Dirac points". Since the low energy physics in graphene is solely related to these Dirac points, it's important to examine the nature of the band structure and eigenenergies in the vicinity of the Dirac points. To this purpose, it is convenient to define the wave vector as $\vec{q} = \vec{k} - \vec{K}$ (or $\vec{K}'$) assuming $|\vec{q}| \ll |\vec{K}|$ (or $|\vec{K}'|$) and then expanding tS_k around $q = 0$. This gives

$$\Delta q = -\frac{3ta}{2}e^{-iK_x a}(iq_x - q_y) = \hbar v_F(q_x + iq_y)(1 + O(q/K)^2), \quad (2.6)$$

where $v_F = \frac{3ta}{2\hbar}$. Then the Hamiltonian takes the following form

$$\hat{H} = \hbar v_F \begin{pmatrix} 0 & q_x + iq_y \\ q_x - iq_y & 0 \end{pmatrix} = \hbar v_F \vec{\sigma}\cdot\vec{q}, \quad (2.7)$$

where $\vec{\sigma} = (\sigma^x, \sigma^y)$ is defined in terms of the Pauli matrices

$$\sigma^x = \begin{pmatrix} 0 & 1 \\ 1 & 0 \end{pmatrix} \quad \text{and} \quad \sigma^y = \begin{pmatrix} 0 & i \\ -i & 0 \end{pmatrix}. \quad (2.8)$$

Equation (2.7) resembles the Dirac equation for relativistic massless particles except that the velocity of light, *c*, is replaced by the Fermi velocity $v_F = \frac{3ta}{2\hbar} \cong 1 \times 10^6$ m/s, which is ~ 300 times smaller than *c*. The eigenenergies for this well-known Hamiltonian are given by

$$E(q) = \pm\hbar v_F|q|. \quad (2.9)$$

These results show that around the points K and K', the energy dispersion for graphene is linear and similar to the Einstein's relativistic dispersion relation for massless particles. As a consequence, the quasiparticles in graphene are called massless Dirac fermions and the points (K and K') at which the conduction bands and valence bands meet are called Dirac points. Due to this linear energy dispersion and massless Dirac fermions, graphene shows many exceptional properties, which includes ambipolar conduction,[46] charge carrier tunability,[47] high carrier mobility, *etc.*[48] These exceptional properties have opened a new playground for physicists and engineers to observe and exploit many new physical phenomena.

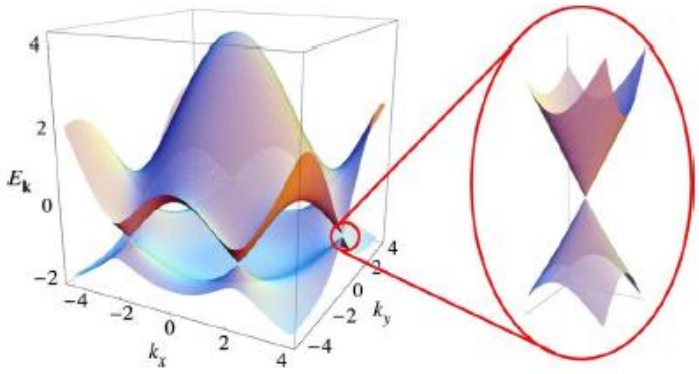

Figure 2.2 Energy (E_k) - momentum ($k_{x,y}$) dispersion of graphene and representation of the band structure around the Dirac point in the Brillouin zone. Figure adapted from Ref [44].

We now examine the density of states, carrier density and mobility in graphene. Based on the 2D nature of graphene and its linear energy dispersion, one can find that the density of states can be expresses as $D(E) = \frac{2E}{\pi\hbar^2 v_F^2}$, and that the carrier density at T = 0K is $n(E_F) = \frac{E_F^2}{\pi\hbar^2 v_F^2}$.

For graphene on a SiO_2/Si substrate, the carrier density can be tuned by electrostatic gating according to the following relation

$$dn = \frac{\varepsilon_0 \varepsilon}{de} dV_g, \tag{2.10}$$

where ε_0 and ε are the permittivity in free space and relative permittivity of the SiO_2 layer, respectively, d is the thickness of the oxide layer and V_g is the applied gate voltage on the Si substrate, as shown in inset of Figure 2.3. Depending on the applied gate voltage (V_g), the Fermi level also moves up or down through the Dirac point according to $E_F = \pm\hbar v_F\sqrt{\pi n}$. As the density of charge carrier changes with V_g, the resistance also changes with a maximum value at a particular gate voltage at which the Fermi level aligns with the Dirac point, as shown in Figure 2.3.

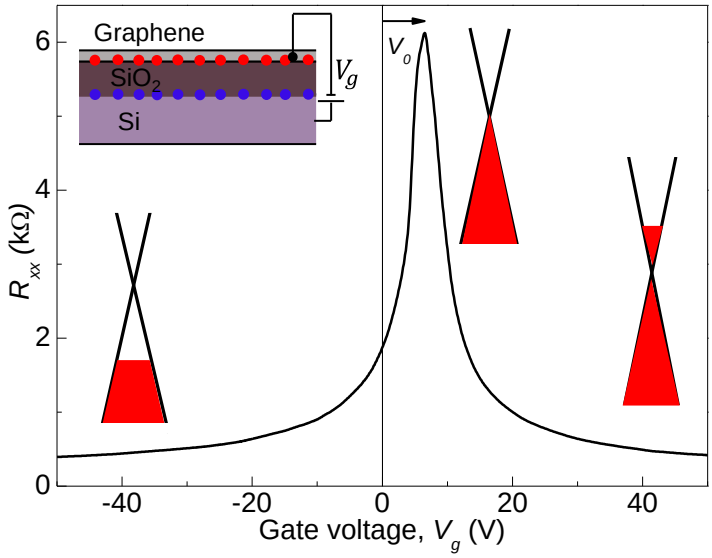

Figure 2.3 Longitudinal resistance as a function of applied gate voltage (V_g) in graphene on a SiO_2/Si substrate (inset). V_0 denotes the gate voltage at which the Fermi level aligns with the Dirac cone. For $V_g > V_0$ ($V_g < V_0$), the Fermi level is in the conduction (valence) band and the carriers are electrons (holes).

Another important parameter is the mobility. This can be determined from the dependence of the resistivity, ρ, on V_g, *i.e.* $\mu = 1/en\rho$, and from Hall measurements of the carrier density, n, which is discussed in section 3.1.1. Previous studies have found that the carrier mobility can be affected by many factors such as surface roughness of the substrate, impurity scattering, ripples in the graphene layer, strain, temperature, *etc.*[49-55] To maximise the carrier

mobility, different substrates and fabrication techniques have been employed in the last few years.[48,49,56] Among those, the encapsulation of exfoliated graphene by hBN on a hBN/SiO_2 substrate has enabled mobilities of up to 1×10^6 cm^2/Vs at $T = 1.7K$.[48]

2.1.2 hBN

Boron nitride (BN) is a chemical compound, which can exists in different crystalline forms, like hexagonal, cubic and wurtzite. The most stable, studied and useful form of BN for semiconducting technologies is the hexagonal (hBN) form. Although it was widely used as lubricant, only recently it has been demonstrated that single or a few layers of hBN can be extracted from bulk crystals.[57] These layers have no dangling bonds and contain a small density of charge traps,[58,59] providing an excellent dielectric material for graphene electronics.[27,60] Other important features of hBN are its strong resistance to mechanical manipulation and chemical interactions,[61] large band gap (~ 6 eV)[62] and optical transparency over a wide range of wavelengths.[63] These properties have made it an ideal candidate for the encapsulation of graphene or other 2D materials, which are unstable in ambient conditions.[64] Also, hBN has been used as tunnel barrier in tunnelling transistors.[65-67]

2.1.3 Metal chalcogenides: focus on InSe

Metal chalcogenides are III-VI semiconducting crystals with the stoichiometry MX or M_aX_b, where M is a metal (Ga, In, *etc.*) and X is a chalcogen (*e.g.* S, Se, Te, *etc.*). Similar to graphite, these crystals possess strong in-plane covalent bonds in each layer and the layers interact through weak van der Waals forces. However, in contrast to graphite, metal chalcogenides exhibit

a wide variety of polytypes, for example β, γ and ε for InSe[68-70], α, β, γ, δ and κ for In_2Se_3,[70,71] and β, ε, γ and δ for GaSe,[72] depending on the stacking sequence of the layers. Earlier studies of these bulk crystals focussed on their anisotropic mechanical, optical and electronic properties, which made them good candidates for applications in photovoltaic,[73-76] non-linear optics[77-81] and THz generators.[80,82,83]

The discovery of graphene and its zero bandgap stimulated further research on metal chalcogenides, which possess a tuneable band gap. Table 2.1 summarises the band gaps of the most intensively studied bulk metal chalcogenides.[84] Here we focus on the γ-polytype phase of InSe crystals grown by the Bridgman method.

Table 2.1 Bandgaps of bulk metal chalcogenides at T = 300K. Reproduced and modified from Ref [84].

Material	Bandgap E_g at T = 300K (eV)	Remarks	Ref.
GaTe	1.7	Direct	[85]
GaSe	2.11	Direct at 2.13 eV	[20]
GaS	2.59	Direct at 3.05 eV	[86]
InSe	1.26	Direct	[29]
α-In_2Se_3	1.3	Direct	[19]

The Bridgman grown γ-polytype InSe crystals contain an excess of interstitial In atoms, thus leading to an unintentional *n*-type doping. The concentration of electrons is $n = 10^{15}$ cm^{-3}.[87] Also, *p*-type InSe can be grown by introducing Zn or Cd atoms during the growth of the crystal. The hole concentration achieved in *p*-type InSe is $p = 10^{13}$ cm^{-3}.[87]

The γ- polytype InSe has a rhombohedral crystal structure (Figure 2.4a). The primitive unit cell contains three layers each of which has a thickness of *L*

= 0.8320 nm (N = 1 layer). The lattice parameter is c = 2.4961 nm along the c-axis. Each layer consists of four closely packed, covalently bonded, monoatomic sheets in the sequence Se-In-In-Se. Within each plane, atoms form hexagons with lattice parameter a = 0.4002 nm. The layers interact by weak van der Waals forces, resulting in anisotropic electronic properties[88,89] and can be cleaved by mechanical exfoliation. The non-metallic Se atoms form the surface of the exfoliated InSe nanoflakes and hinder oxidation, providing a high chemical stability under ambient conditions.[90,91] This enables to obtain high quality interface when InSe is stacked with other 2D materials like graphene.

In its bulk form, InSe has a direct band gap E_g = 1.26 eV at room temperature.[92] Earlier studies revealed that the carriers have anisotropic effective masses and a small effective mass ($m_{e/\!/c}$ = 0.08m_e and $m_{e\perp c}$ = 0.14m_e) in the conduction band.[33] It has been demonstrated that with reducing the layer thickness of InSe, E_g undergoes a strong blue shift from the near infrared to the visible region due to strong quantum confinement of electrons along the c-axis, in agreement with a simple 2D quantum well model (Figure 2.4b).[34,37,93,94] Also, InSe undergoes a direct-to-indirect band gap crossover as the number of layers is reduced to ~ 10 layers, but remains optically active (Figure 2.4c).[37,95] The analysis by G. W. Mudd *et al.*[37] revealed that the in-plane electron and exciton masses are quite small compared to those in transition metal dichalcogenides (TMDCs)[96] and weakly dependent on the layer thickness. Also, low temperature optical studies on exfoliated InSe nanoflakes revealed that the binding energies of donor states increases significantly with decreasing number of layers due to the compression of the carrier wavefunction perpendicular to the plane of the flakes.[97]

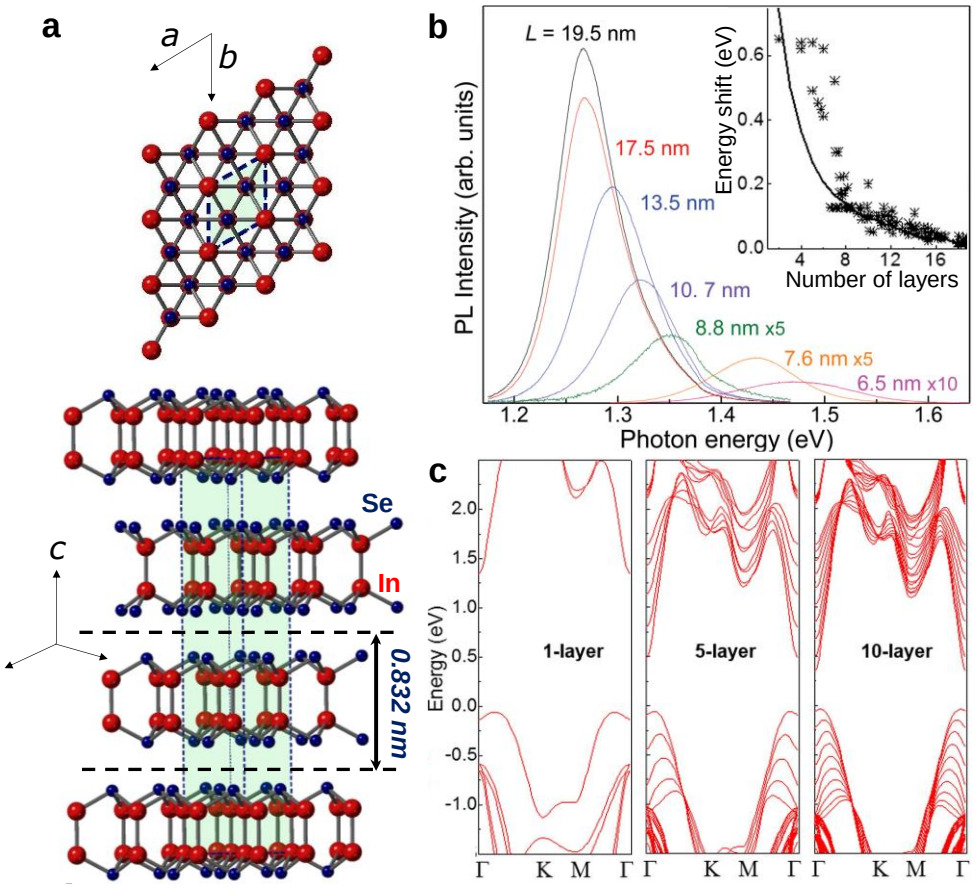

Figure 2.4 (a) Schematic of the crystal structure of rhombohedral InSe. The unit cell is indicated in green. The lattice constant along the c-axis is $c = 2.4961$ nm and the in-plane lattice constant is $a = b = 0.4002$ nm. The thickness of a single layer is $L = c/3 = 0.8320$ nm. (b) Typical μPL spectra of InSe layers at T = 300K with peak energy strongly dependent on the layer thickness L (P = 0.1 mW and λ = 633 nm). Inset: DFT (lines) and measured (symbol) energy increase of the band gap of InSe with decreasing number of layers. (c) Band structure of InSe for 1, 5 and 10 layers. Figure (b) and (c) are adapted from Ref [34] and [37].

S. R. Tamalampudi *et al.*[35] demonstrated bendable photodetectors using few layer InSe on a flexible polyethylene terephthalate (PET) film. However, the fabrication of phototransistors with broadband spectral response and high photoresponsivity is generally challenging. G. W. Mudd *et al.*[29] demonstrated a broad photoresponsivity and values of responsivity of up to $\approx 10^5$ AW^{-1} at 633 nm in graphene/*n*-InSe/graphene photodetectors (Figure 2.5). The photoresponsivity in these devices is the highest ever reported for any 2D vdW

crystal. This arises from the favourable band alignment of graphene and InSe for injection and extraction of carriers at the graphene/InSe interface. This phenomenon is further discussed in chapter 5.

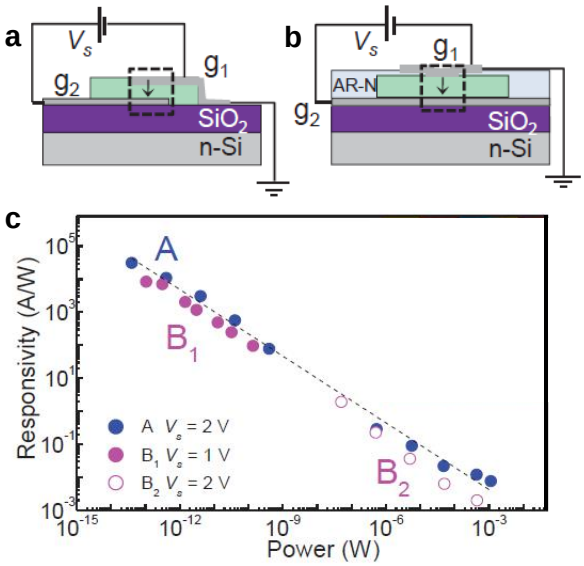

Figure 2.5 Schematic structure of graphene/n-InSe/graphene vertical devices fabricated by two different processes (a) type A (using exfoliated graphene) and (b) type B (using CVD graphene). (c) Photoresponsivity versus laser power at T = 300K and λ = 633 nm for device A (blue) and devices B (magenta). Devices B_1 and B_2 are based on InSe flakes of thickness t = 130 and 80 nm, respectively. Figure taken from Ref [29].

Multi-layer InSe FETs on a bilayer dielectric of poly-methyl methacrylate (PMMA)/Al_2O_3 with a room temperature field effect mobility $\mu > 10^3$ cm^2/Vs and high current on/off ratios (10^8) have been reported by W. Feng *et al.*[36] The PMMA/Al_2O_3 dielectric bilayer reduces the scattering of carriers by interfacial impurities and surface polar phonons, enabling a high mobility at room temperature. Recently, D. A. Bandurin *et al.*[17] fabricated few layer InSe FETs: the encapsulation of InSe by hBN enables to achieve electron mobilities exceeding 10^3 cm^2/Vs and 10^4 cm^2/Vs at room temperature and liquid helium temperatures, respectively. This has also enabled the observation of Shubnikov de Haas (SdH) oscillations and a fully developed quantum Hall effect (Figure

2.6b and c). The room temperature electron mobility in 6*L* InSe ($\mu \sim 10^3$ cm^2/Vs) is higher than the highest electron mobility reported in any TMDC,[98,99] which is consistent with the smaller in-plane effective mass of electrons in InSe.[33] Very recently, one dimensional quantisation of electrons by electrostatic gating has been reported in few layer InSe.[18]

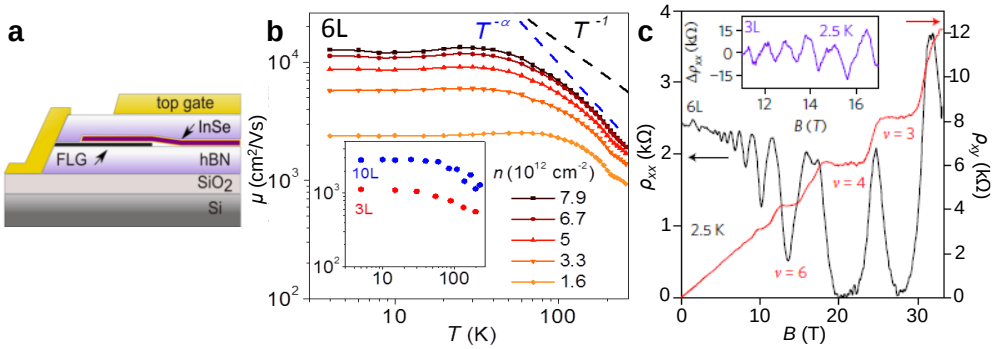

Figure 2.6 (a) Cross-sectional schematic of InSe FETs. (b) *T*-dependence of the Hall mobility μ for a 6*L* device. The dashed black line shows the dependence expected taking into account electron scattering by acoustic phonons. Inset: μ (*T*) for 3 and 10*L* at high electron densities *n* (*n* = 8.3 and 7.7 $\times 10^{12}$ cm^{-2}, respectively). (c) Low-*T* ρ_{xx} and ρ_{xy} for a 6*L* device; *n* = 2 $\times 10^{12}$ cm^{-2}. Inset: SdH oscillations in 3*L* InSe; *n* = 8.9 $\times 10^{12}$ cm^{-2}. Figure adapted from Ref [17].

In summary, the quasi-direct band gap of InSe down to few layer, its tuneability by layer thickness, the small in-plane electron effective mass and high room temperature electron mobility make InSe a promising 2D material for the next generation of functional semiconducting devices.

2.1.4 Other 2D materials

Another important group of layered materials comprises the transition metal dichalcogenides (TMDCs), which have stoichiometry MX_2, where M is a transition metal element (*e.g.* Mo, W, *etc.*) and X is a chalcogen (*e.g.* S, Se, *etc.*). In particular, molybdenum (Mo) and tungsten (W) based TMDCs have been extensively studied due to their distinctive electronic and optical properties

and high stability under ambient conditions. For example, bulk MoS_2 is an indirect band gap (1.2 eV) semiconductor with a weak photoluminescence, whereas the monolayer MoS_2 has a direct band gap of 1.9 eV and an intense photoluminescence.[100] Similar indirect to direct band gap transitions with reducing the layer thickness have been reported for $MoSe_2$, WS_2 and WSe_2.[101,102] The strong photoluminescence from the single layers has enabled the fabrication of optoelectronic devices.[103] Also, the splitting of the valence band due to spin-orbit interactions[104] and spin-valley coupling[105] make TMDCs promising candidates for valleytronics and spintronics.[10,106-110]

Earlier work on single layer TMDC field effect transistors (FETs) showed very low carrier mobilities (*e.g.* $\mu \sim 174$ cm^2/Vs for monolayer MoS_2 at $T = 4$K).[111,112] With the growing interest in TMDCs, this limitation has been partially overcome by the use of hexagonal boron nitride (hBN) as a substrate, as done for graphene,[113] by the exfoliation of TMDC layers in a glove box and their encapsulation with hBN.[98] Also, the fabrication of good ohmic contacts by using graphene electrodes has helped to improve the mobility in TMDCs.[114] Thus low temperature mobilities exceeding 10^4 cm^2/Vs have been achieved in MoS_2, WS_2 and WSe_2 FETs[98,99,113,114] and has enabled to observe SdH oscillations and the quantum Hall effect.[98,99,113,114] However, carrier scattering by optical phonons at room temperature limits the mobility to $\mu < 10^2$ cm^2/Vs,[98,114] restricting the application of TMDCs as a main channel for high performance transistors.

Another 2D layered material known as black phosphorus (bP) has received increasing attention. It shows layer dependent band gap from 0.33 eV (bulk) to 1.5 eV (monolayer).[115,116] Multi-layer bP has demonstrated much

higher electron mobility (~ 1000 cm^2/Vs) at room temperature compared to TMDCs. However, bP is less stable in ambient conditions. A mobility of $\mu >$ 4000 cm^2/Vs at liquid helium temperatures has made possible to observe SdH oscillations and the quantum Hall effect.[64,117-119] In monolayer and bi-layer bP, the mobility drops to ~ 1 and 80 cm^2/Vs, respectively.[64] Due to the stability and high mobility in thicker layers, most research has been carried out on bulk bP crystals rather than on 2D bP.

2.2 Low dimensional magnetic semiconductors

2D materials have already stimulated new applications in electronics and optoelectronics. To extend their application in spintronic devices, the development of new magnetic 2D layers is of great interest. Recently, both diluted and intrinsic magnetic 2D semiconductors have been investigated theoretically, but only few of them have been synthesized and studied. This section describes some of these recent works.

Recent theoretical work has shown that 3d transition metals in single layer InSe can modify electronic and magnetic properties of the crystal.[120,121] In particular, a large magnetic moment (~ 5 μ_B) can be achieved when Fe-atoms substitute In-atoms (Figure 2.7a). The calculated density of states demonstrates the asymmetry between spin-up and spin-down states (Figure 2.7b) due to the *p-d* hybridisation between the Fe dopants and its neighbouring In (Se) atoms. As a result, Fe-doped InSe is a ferromagnetic material, but also retains its semiconducting properties. Similar theoretical work has been reported by other groups for Cr in single layer InSe.[122]

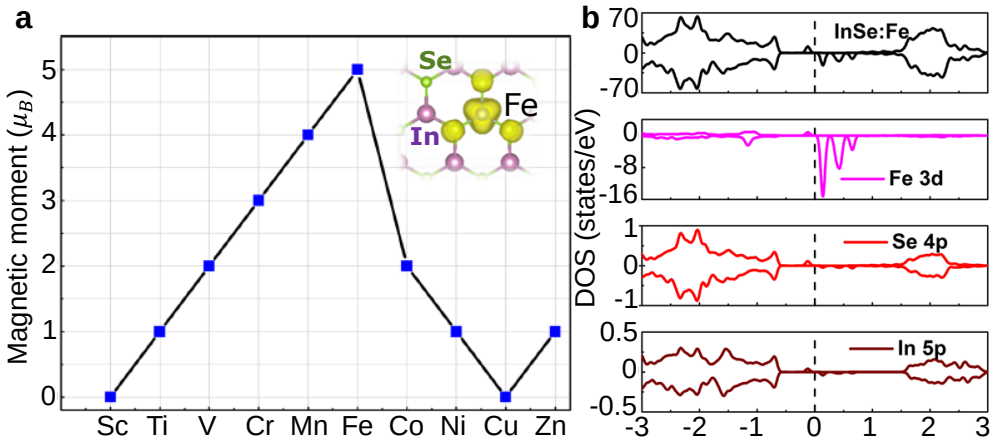

Figure 2.7 (a) Magnetic moment of different transition metals in single layer InSe. Inset: spin density for a single Fe-atom in InSe. (b) Total and partial density of states for Fe-doped InSe. The vertical black dashed line indicates the Fermi level. Figure reproduced from Ref [121].

Z. Fu *et al.*[123] investigated the electronic and magnetic properties of single layer InSe containing interstitial and substitutional boron (B) atoms using first-principles calculations. At low concentrations (up to 12.5%) interstitial B can induce antiferromagnetism in InSe. However, the induced magnetism disappears at high B content (~ 25%) at which InSe shows a metallic behaviour. On the other hand, no magnetism was observed for B-substitutional. Their studies revealed that both the doping content and location of the dopant have significant influence on the electronic and magnetic properties of InSe.

Besides the diluted magnetic InSe semiconductors, there is another class of magnetic 2D materials called intrinsic magnetic semiconductors, which are difficult to obtain experimentally. One example is the ferromagnetic ternary compound $CrSiTe_3$. Earlier studies showed that bulk $CrSiTe_3$ is an intrinsic ferromagnetic layered semiconductor with an out-of-plane easy axis and Curie temperature of $T_c = 32$K.[124,125] Recent theoretical investigations revealed the feasibility of exfoliation of this layered material, which has a cleavage energy (43.7 meV per atom)[126,127] comparable to that of graphite (61 meV per atom).[128]

More interestingly, the exfoliated few layers and single layer $CrSiTe_3$ inherit the ferromagnetic and semiconducting properties of the parent 3D crystal. Also, the Curie temperature of thin layers is larger than that of bulk crystals.[126,127] Furthermore, it has been demonstrated theoretically that the 2D ferromagnetism can be enhanced by applying a moderate tensile strain.[126]

Like ternary magnetic semiconductors, transition metal di- and trihalides are also promising layered materials.[129] Among them CrI_3 is the most promising magnetic semiconductor. It has a band gap of 1.2 eV at T = 300K, a relatively high Curie temperature ($T_c = 68$K),[130] and strong magnetic anisotropy.[131] Theoretical studies predicted that the ferromagnetism may persists in single layer CrI_3.[132] This was demonstrated experimentally: monolayer CrI_3 possesses ferromagnetism with an out-of-plane easy axis.[133] More interestingly, the ferromagnetism in CrI_3 is layer thickness dependent. Although the reported Curie temperature for monolayer CrI_3 crystal is slightly lower (45K) than that of bulk crystals (68K), it is foreseen that this value could be enhanced by applying an external electric field.[129]

Chapter 3

Electronic and magnetic properties of semiconductors

This chapter describes the basic theory of electronic transport in two-dimensional (2D) materials, different types of magnetism and the basic principles of electron spin resonance (ESR).

3.1 Electronic transport in 2D materials

Transport measurements in the presence of a magnetic field can provide a vast amount of information about a 2D electron gas (2DEG) system. In the following section, I discuss the motion of electrons in a magnetic field and the quantum Hall effect.

3.1.1 Quantum Hall effect

The quantum Hall effect (QHE) is a transport phenomenon that can be observed in a 2DEG subject to a quantising magnetic field, perpendicular to the plane of the 2DEG. To describe it, we consider a Hall bar of length L and width W based on a 2D semiconductor in an electric field $\boldsymbol{E} = [E_x, E_y, 0]$ and magnetic field $\boldsymbol{B} = [0, 0, B]$. Then the equation of motion for a charge carrier $q(\pm e)$ with effective mass m^* and drift velocity $\boldsymbol{v}$, subject to scattering with collision time τ is

$$m^* \frac{d\boldsymbol{v}}{dt} + \frac{m^* \boldsymbol{v}}{\tau} = q(\boldsymbol{E} + \boldsymbol{v} \times \boldsymbol{B}). \tag{3.1}$$

In steady state, $\frac{d\boldsymbol{v}}{dt} = 0$. Then (3.1) becomes

$$\boldsymbol{v} = \frac{q\tau}{m^*}(\boldsymbol{E} + \boldsymbol{v} \times \boldsymbol{B}). \tag{3.2}$$

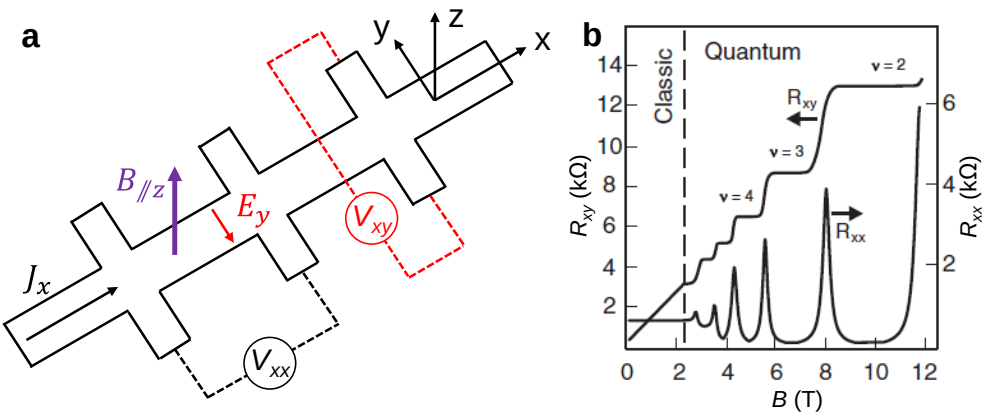

Figure 3.1 (a) Schematic of magneto-transport measurements in a Hall bar. (b) Classic (quantum) Hall effect at low (high) magnetic fields in a conventional semiconductor-based 2D system. Figure (b) taken from Ref [134].

For a system with a density of carriers, n, the 2D current density is $\boldsymbol{J} = nq\boldsymbol{v} = (J_x, 0, 0)$, and the Hall voltage ($V_H$) and the Hall coefficient (R_H) are

$$V_H \equiv V_y = \frac{I_x B}{nq}, \tag{3.3}$$

and

$$R_H \equiv \frac{E_y}{J_x B} = \frac{1}{nq}. \tag{3.4}$$

The current density $\boldsymbol{J}$ can be expressed in terms of the conductivity and resistivity tensors as follows:

$$\boldsymbol{J} = [\sigma]\boldsymbol{E}, \tag{3.5}$$

where $[\sigma]$ is the conductivity tensor, $[\sigma] = \begin{pmatrix} \sigma_{xx} & \sigma_{xy} \\ \sigma_{yx} & \sigma_{yy} \end{pmatrix}$,

and $[\rho]$ is the resistivity tensor, $[\rho] = [\sigma]^{-1} = \begin{pmatrix} \rho_{xx} & \rho_{xy} \\ \rho_{yx} & \rho_{yy} \end{pmatrix}$,

with the longitudinal and Hall resistivity given by

$$\rho_{xx} = \rho_{yy} = \frac{\sigma_{xx}}{\sigma_{xx}^2 + \sigma_{xy}^2} \equiv \frac{E_x}{J_x} = \frac{W}{L}\frac{V_x}{I_x} = \frac{1}{nq\mu}, \tag{3.6}$$

$$\rho_{xy} = -\rho_{yx} = \frac{\sigma_{xy}}{\sigma_{xx}^2 + \sigma_{xy}^2} \equiv \frac{E_y}{J_x} = \frac{B}{nq}. \tag{3.7}$$

Here $\mu = q\tau/m^*$ is the mobility of the charge carriers.

This classic Hall effect picture breaks down at low temperature and high magnetic field.[134] The Hall resistivity ρ_{xy} becomes quantised into integer multiple of h/e^2, where h is the Planck constant. Simultaneously, the longitudinal resistivity ρ_{xx} vanishes. This effect is called quantum Hall effect (QHE) and the quantized value h/e^2 is known as Klitzing constant since its discovery by Klaus von Klitzing in 1980.[135,136]

The QHE can be understood by taking into account the Landau level (LL) quantisation of the electron motion.[137] For a 2DEG system with a parabolic energy band dispersion, the Hamiltonian for the charge carriers in the presence of electric and magnetic fields can be written as

$$\hat{H} = \frac{1}{2m^*}(\hat{p} + e\hat{A})^2, \tag{3.8}$$

where $\hat{p}$ is the momentum operator and $\hat{A}$ is the magnetic vector potential, *e.g.* $\boldsymbol{B} = \boldsymbol{\nabla} \times \boldsymbol{A}$. By choosing the Landau gauge $\hat{A} = (0, B\hat{x}, 0)$, the Hamiltonian can be rewritten as

$$\hat{H} = \frac{p_x^2}{2m^*} + \frac{1}{2m^*}(\hat{p}_y + eB\hat{x})^2$$

$$\hat{H} = \frac{p_x^2}{2m^*} + \frac{1}{2}m^*\omega_c^2(\hat{x} + \frac{\hbar k_y}{m^*\omega_c})^2, \tag{3.9}$$

where $\hat{x}$ is the position operator and $\omega_c = \frac{eB}{m^*}$ is the cyclotron frequency. Equation (3.9) is the Hamiltonian of a harmonic oscillator in the *x*-direction centred at $x = -\frac{\hbar k_y}{m^*\omega_c}$. The eigenenergies for this well known one dimensional harmonic oscillator are

$$E_N = \hbar\omega_c\left(N + \frac{1}{2}\right), \tag{3.10}$$

where $N = 0, 1, 2, ...$ These quantised energy levels are known as Landau levels (LLs). For non-relativistic fermions with a parabolic energy band dispersion, the LLs are equally spaced by $\Delta E_{LL} = \hbar\omega_c$. Each LL has a degeneracy

$$n_{LL} = \frac{eB}{h} \tag{3.11}$$

and the LL filling factor is

$$\nu = \frac{density\ of\ carriers\ n}{degeneracy\ n_{LL}} = \frac{nh}{eB}. \tag{3.12}$$

Thus, the Hall resistivity can be written as

$$\rho_{xy} = \frac{B}{nq} = \frac{h}{\nu e^2}. \tag{3.13}$$

Depending on the value of ν, the QHE is termed as integer quantum Hall effect (IQHE) (when ν is an integer) or the fractional quantum Hall effect (FQHE) (when the value of ν is a fraction).[135,138]

However, graphene is different from conventional two dimensional systems, such as GaAs/AlGaAs 2DEGs. For example, the charge carriers in graphene are massless Dirac fermions with a linear energy band dispersion. The Hamiltonian for such massless Dirac fermions is

$$\widehat{H} = \gamma v_F \begin{pmatrix} 0 & \Pi_x - i\Pi_y \\ \Pi_x + i\Pi_y & 0 \end{pmatrix}, \tag{3.14}$$

where $\Pi = \hat{p} + e\hat{A}$ is the gauge invariant kinetic momentum.[139] The Landau levels for graphene are

$$E_N = sgn\ (N)\sqrt{2\hbar eBv_F^2|N|}, \tag{3.15}$$

where the integer N corresponds to electrons for $N > 0$ and holes for $N < 0$; $N = 0$ corresponds to the electron-hole degenerate level at the so-called Dirac point.[140-143]

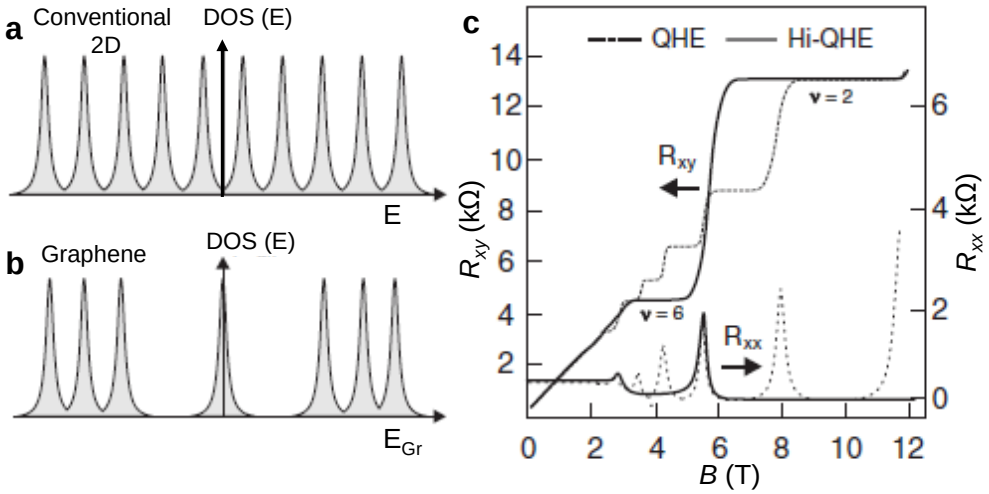

Figure 3.2 Sequence of LLs in (a) conventional 2D systems and (b) single layer graphene. (c) Comparison of QHE (dashed lines) in conventional 2D systems and the Half-integer-QHE (solid lines). Figures adapted from Ref [134].

The LLs in graphene are different from those in conventional 2DEGs in several aspects (Figure 3.2). Firstly, the LL energy spacing in graphene is $\Delta E_{LL-Gr} = v_F\sqrt{2\hbar eB}[\sqrt{N+1}-\sqrt{N}]$, whereas for conventional 2DEG, $\Delta E_{LL} = \frac{\hbar eB}{m}$. Secondly, the LLs are unevenly spaced in graphene and the largest energy spacing is between the $N = 0$ and $N = +1$ or -1 LLs, whereas they are equally spaced in conventional 2DEGs. Moreover, the lowest LL $N = 0$ at $E = 0$ is independent of magnetic field and is equally shared by electrons and holes. Along with these special features, each LL in graphene can take twice as many carriers with compared to that of other conventional 2DEGs due to its valley degeneracy (K and K'). Thus, the hole density n (Fermi level $E_F < 0$) corresponding to N filled LLs in graphene is

$$n = N\frac{2eB}{h}|_K + N\frac{2eB}{h}|_{K'} + \frac{2eB}{h}|_{E=0} = \frac{4eB}{h}\left(N+\frac{1}{2}\right). \qquad (3.16)$$

Then the Hall resistivity can be written as $\rho_{xy} = \frac{B}{ne} = \frac{h}{4e^2(N+\frac{1}{2})}$, named as half-integer quantum Hall effect (Hi-QHE). All of these special features are due to the unique nature of massless Dirac fermions in graphene.

The simple derivation of the QH resistance described above explains the quantised value of the Hall resistance at particular magnetic fields when an integer number of LLs are completely filled. But experimentally the Hall plateaux and the zero longitudinal resistance ($\rho_{xx} = 0$) extend over a range of magnetic field. This can be understood by considering disorder effects (Figure 3.3). In the presence of disorder, the LLs are broadened due to spatial fluctuations of the potential in the 2DEG. The mean value of the potential is centred at the middle of the LL, corresponding to extended states, and the upper and lower tails correspond to localised states. When, under a varying *B*, the Fermi level scans through the localised states between one LL and an adjacent one, the carriers in localised states (E_{F1}) do not contribute to the conduction. Correspondingly the Hall resistance (ρ_{xy}) and longitudinal resistance (ρ_{xx}) remain unchanged. When the Fermi level (E_{F2}) is in the extended states close to the LL centres (Figure 3.3), the carriers are allowed to move across the sample and hence ρ_{xx} and ρ_{xy} increase.

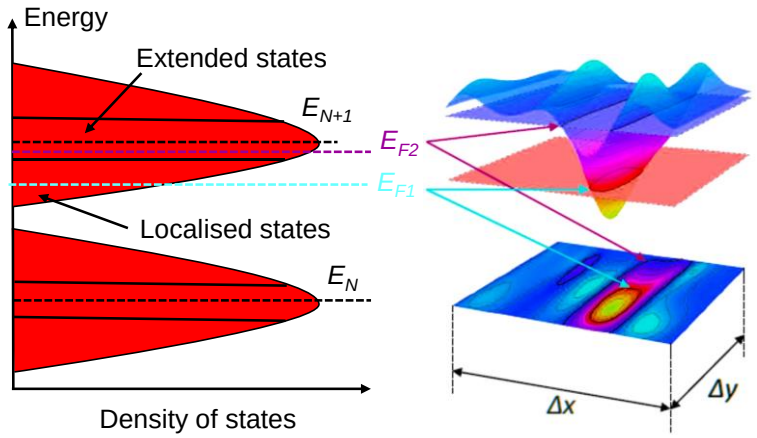

Figure 3.3 Spatial potential fluctuations in a real disordered 2DEG and corresponding LLs.

There is another alternative way of measuring the quantum Hall effect, which is often used to observe the QH plateaux. In this method, the Fermi level

is swept by changing a gate voltage, but keeping the magnetic fields at a fixed value. Figure 3.4 shows the QHE for massless Dirac fermions in monolayer graphene measured in this way at a particular magnetic field B = 14T. Here the Hall conductivity is quantised at filling factors $4(N+1/2)$.[143]

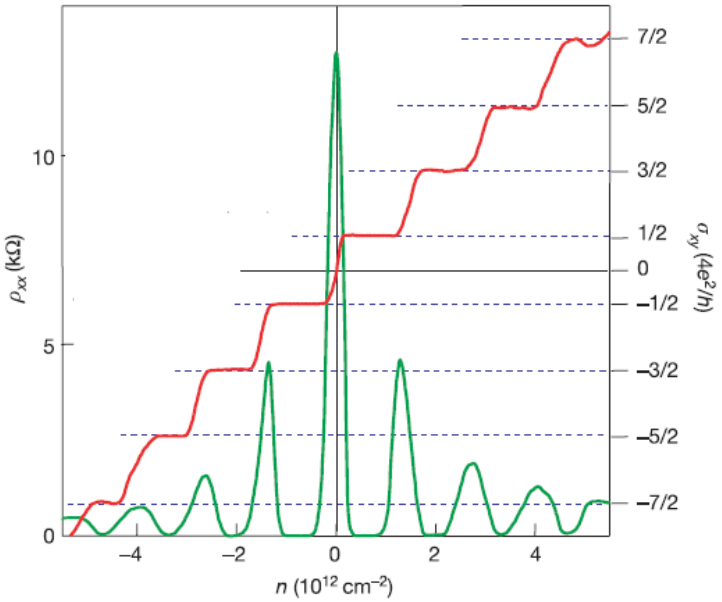

Figure 3.4 Hall conductivity σ_{xy} (red line) and longitudinal resistivity ρ_{xx} (green line) of graphene as a function of carrier concentration (gate voltage) at B = 14T and T = 4K. Figure adapted from Ref [143].

It has been demonstrated that the QHE plateaux are robust at low temperature, high magnetic field and small current density.[144] With increasing temperature and/or low magnetic field, the longitudinal resistivity increases due to thermal excitation of carriers out of the localised states and inelastic scattering. Also, an abrupt increase in the longitudinal resistivity and a deviation of Hall resistivity from the quantised value have been reported when the current is higher than a critical value.[145,146] This phenomenon known as QHE breakdown has been investigated theoretically and experimentally.[147-155] Among various models, the Komiyama and Kawaguchi's bootstrap-type electron heating (BSEH) model has successfully explained several observations of QHE breakdown with the predicted $B^{3/2}$dependence of the critical Hall

field.[154] But the exact nature of the QHE breakdown is still not completely clear and a better theory needs to be developed.

For quantum metrology, the robustness of the quantum Hall state is crucial. The correct h/ve^2 value should be insensitive to variations in experimental parameters. In particular, it is desirable to achieve a robust Hall plateau at low magnetic fields and room temperature. Along with these two factors, to obtain the desire signal to noise ratio, the current density should be sufficiently large.

Baker *et al.*[156,157] found that the charge carriers in graphene can lose their energy very efficiently to the lattice. Thus the hot electron relaxation time is at least one order of magnitude shorter than that of traditional GaAs devices over a wide range of temperature. This shorter electron relaxation time along with the large cyclotron energy gap in graphene can support a breakdown current density as high as 43 Am^{-1} at high fields, which is 30 times larger than previously reported in traditional GaAs.[158] Along with this high breakdown current density, the magnetic field dependent charge transfer in epitaxial graphene on SiC produces a wide $\nu = 2$ quantum Hall plateau.[159] The QHE in graphene is more accurate than in GaAs (Figure 3.5a).[144] Moreover, epitaxial graphene showed a quantisation of ρ_{xy} up to at least T = 15K with good accuracy (ppb-level) (Figure 3.5b),[144] whereas for the best conventional GaAs/AlGaAs 2DEG, the operational temperature is generally below 2K.[136] These results are due to the larger energy spacing between the $N = 0$ and $N = \pm 1$ LLs in graphene, which is approximately 7 times larger than that of traditional GaAs/AlGaAs 2DEG at B = 10T.[144] In summary, it has been demonstrated that the robustness of the quantisation of ρ_{xy} in terms of

temperature, critical current and magnetic field is exceptional for graphene compared to conventional GaAs/AlGaAs 2DEGs.[156-161] Thus, epitaxially-grown graphene on SiC is likely to replace III-V compound heterostructures for the next generation QH resistance standards.[134,160-164]

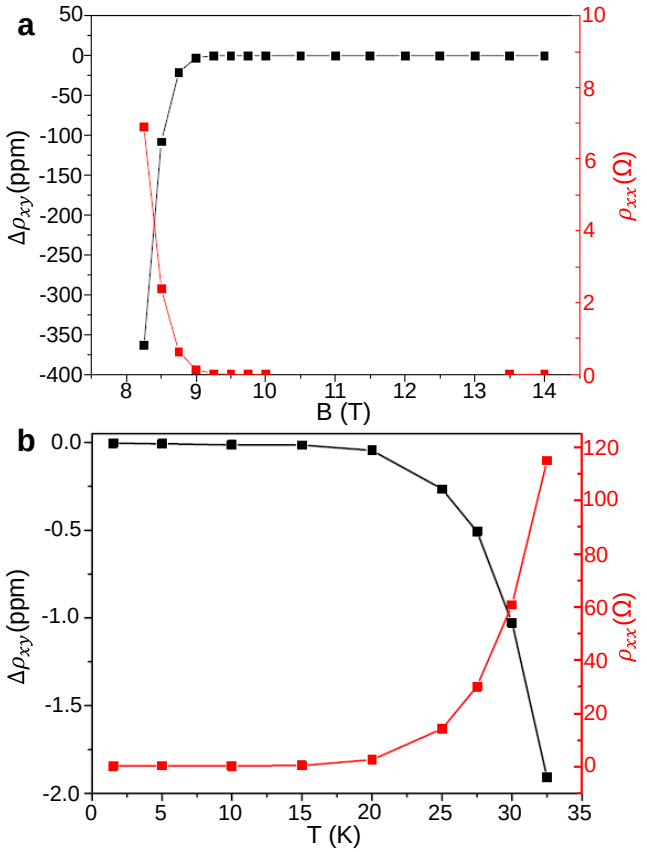

Figure 3.5 (a) Robustness of quantisation as a function of magnetic field. $\Delta\rho_{xy} = 2[\rho_{xy}^{Graphene}(B) - \rho_{xy}^{GaAs/AlGaAs}(B = 10.5\text{T})]/R_K$ and ρ_{xx} as a function of magnetic flux density in graphene at I = 60 μA. (b) Robustness of quantisation as function of temperature as in (a). B = 14T for graphene and B = 10.5T for GaAs/AlGaAs at I = 60 μA. Figure taken from Ref [144].

In chapter 5 and 6, we demonstrate that this quantum magnetoresistance phenomenon is not unique to graphene on SiC. We show that the magnetic, electric field- and photon-induced transfer of charge carriers between InSe and the degenerate Landau level states of an adjacent graphene layer leads to a giant quantum Hall plateaux at high temperature.

3.2 Magnetism

This section describes the underlying origin of magnetism and general mechanisms that explain different magnetic phenomena.[165-167] The magnetic properties of materials are fundamentally the results of the motion of electrons in atoms. Each atom contains many electrons with orbital and spin angular motion. The magnetic dipole moment (normal to the plane of the orbit) associated with the orbital angular motion is $\mu_l = \mu_B\sqrt{l(l+1)}$ and the magnetic dipole moment (parallel to the axis of motion) due to the spin angular motion is $\mu_s = \mu_B\sqrt{s(s+1)}$, where $\mu_B = \frac{e\hbar}{2m_e}$ is the Bohr magneton.[165] The total magnetic moment for each atom is the vector sum of all of these electronic moments, $\mu_j = \mu_B\sqrt{j(j+1)}$.

For an individual atom with completely filled electron shells or subshells, the total orbital and spin angular momentum cancel out since the electrons are in pair, giving a zero net magnetic moment. Thus materials with completely filled electron shells or subshells are not capable of being permanently magnetised and are called diamagnetic. But there are few materials into which individual atoms have unpaired electrons and a non-zero magnetic moment. In the absence of magnetic fields, the atoms are arranged in such a way that the macroscopic resultant atomic dipole moment is zero. But a net magnetic moment can arise in an applied magnetic field. These materials are called paramagnetic. In the absence of any external magnetic field, only a very small number of materials show a non-zero magnetic moment, which arises from the collective spontaneous ordering of the atomic magnetic moments. These materials are called ferromagnetic. In addition, there are other two types of materials: antiferromagnetic and ferrimagnetic. These are considered as a

subclass of ferromagnetic materials. Figure 3.6 shows the magnetic ordering of the dipole moments of these five types of magnetism and a brief description of them is in the following sections.

3.2.1 Diamagnetism

In diamagnetic substances, all the electronic orbital shells are filled and there are no unpaired electrons so that the atoms have no net magnetic moment.[166] However, a magnetic field modifies the effective current produced by the non-cooperative orbiting electrons and changes the magnetic moment. This causes an induced magnetic moment and a negative magnetisation (Lenz's law). The magnetic susceptibility, $\chi = M/H$, determines the degree to which the magnetisation (M) responds to an applied field (H). The susceptibility for diamagnetic materials is usually one or two order of magnitude weaker than for paramagnetic materials. The other characteristic behaviour of diamagnetic materials is that the susceptibility is temperature independent. Different materials such as C, Si, N_2 and most organic compounds are diamagnetic.[166]

3.2.2 Paramagnetism

In paramagnetic substances, each atom possesses a net magnetic moment due to the incomplete cancelation of unpaired electron's spin and/or orbital angular moment. These magnetic dipole moments are independent and non-interacting with each other. In the absence of an external magnetic field, these non-zero magnetic dipole moments are randomly oriented due to thermal fluctuations and hence the macroscopic magnetisation is zero. However, in the presence of a magnetic field, the dipole moments tend to align along the direction of the applied magnetic field to minimise the energy, giving rise to a

positive magnetic susceptibility and a net magnetisation. When all magnetic dipoles are aligned parallel to the external magnetic field, the magnetisation reaches its maximum value termed as saturation magnetisation (M_s).

For a paramagnetic material system with one type of atoms, the energy levels in the presence of an applied magnetic field $\boldsymbol{H}$ ($\boldsymbol{B} = \mu_0 \boldsymbol{H}$) are

$$U = -\boldsymbol{\mu} \cdot \boldsymbol{B} = m_J g \mu_B B, \tag{3.17}$$

where $\boldsymbol{\mu} = -g\mu_B \boldsymbol{J}$ is the magnetic moment of an atom or ion in free space, m_J is the azimuthal quantum number with values *J*, *J-1*, …, *- J;* g is the Landé g-factor given by the Landé equation

$$g = 1 + \frac{J(J+1)+S(S+1)-L(L+1)}{2J(J+1)}, \tag{3.18}$$

and $\mu_B = \frac{e\hbar}{2m}$ is the Bohr magneton.[167]

For a single spin with no orbital moment, $m_J = \pm\frac{1}{2}$ and $g = 2$. Then (3.17) becomes

$$U = \pm\mu_B B. \tag{3.19}$$

If we consider that the system has only two levels, then at $T = 0$ K, only the lowest level will be occupied. However, at $T \neq 0$ K, the upper level will become occupied. If N_1 and N_2 are the populations of the lower and upper levels, respectively, and $N = N_1 + N_2$ is the total number of atoms, then at equilibrium the fractional populations of these two levels are

$$\frac{N_1}{N} = \frac{\exp(\mu B/\tau)}{\exp(\mu B/\tau)+\exp(-\mu B/\tau)} \quad \text{and} \quad \frac{N_2}{N} = \frac{\exp(-\mu B/\tau)}{\exp(\mu B/\tau)+\exp(-\mu B/\tau)}, \tag{3.20}$$

where we have used $\tau = k_B T$. Then the resultant magnetisation M is proportional to the net spin imbalance per unit volume:

$$M = (N_1 - N_2)\mu = N\mu.\frac{e^x - e^{-x}}{e^x + e^{-x}} = N\mu \tanh x, \tag{3.21}$$

where $x = \frac{\mu B}{k_B T}$. For $x \ll 1, \tanh x \cong x$ and equation (3.21) can be written as

$$M \cong N\mu x = N\mu(\mu B/k_B T). \tag{3.22}$$

The general quantum mechanical case is not limited to $J = \pm\frac{1}{2}$. In a magnetic field an atom with angular momentum quantum number J has $2J$+1 equally spaced energy levels. Then the magnetisation is given by

$$M = NgJ\mu_B B_J(x), \tag{3.23}$$

where $x = gJ\mu_B B/k_B T$ and $B_J(x)$ is the Brillouin function defined by

$$B_J(x) = \frac{2J+1}{2J}\operatorname{cotanh}\left(\frac{(2J+1)x}{2J}\right) - \frac{1}{2J}\operatorname{cotanh}\left(\frac{x}{2J}\right). \tag{3.24}$$

For $x = \frac{\mu B}{k_B T} \ll 1$, we have

$$\operatorname{cotanh} x = \frac{1}{x} + \frac{x}{3} - \frac{x^3}{45} + \cdots \tag{3.25}$$

For $\operatorname{cotanh} x \approx \frac{1}{x}$, equation (3.23) can be written as

$$M = NgJ\mu_B B_J(x) \cong NgJ\mu_B \frac{(J+1)}{3J}\frac{Jg\mu_B B}{k_B T} = \frac{NJ(J+1)g^2\mu_B^2\mu_0 H}{3k_B T}. \tag{3.26}$$

Then the magnetic susceptibility is

$$\chi = \frac{M}{H} = \frac{N\mu_0 J(J+1)g^2\mu_B^2}{3k_B T} = \frac{C}{T}. \tag{3.27}$$

The constant $C = \frac{N\mu_0 J(J+1)g^2\mu_B^2}{3k_B}$ is known as the Curie constant and the relationship (3.27) is known as the Curie law. O_2 and NO are two examples of paramagnetic materials.[167]

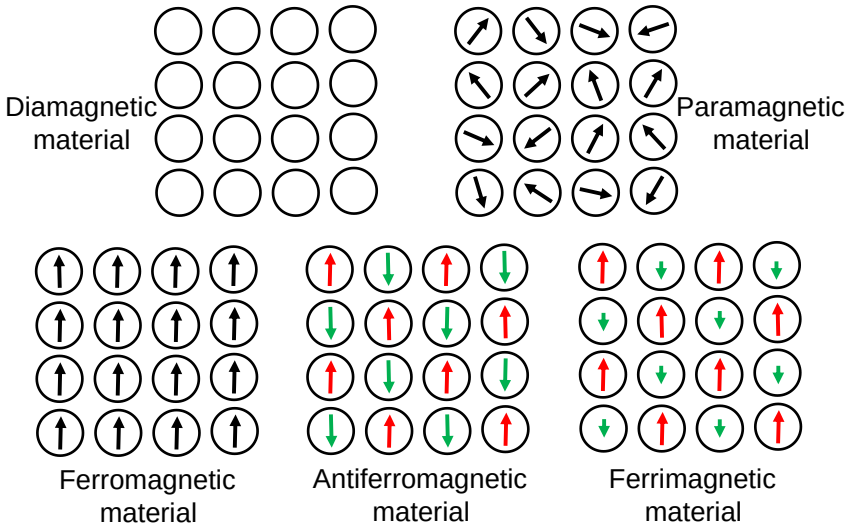

Figure 3.6 Illustration of magnetic dipole moments in five types of magnetic materials in zero external magnetic field.

3.2.3 Ferromagnetism

Ferromagnetic materials differ from diamagnetic and paramagnetic materials in several ways. In the absence of an external magnetic field, they show spontaneous magnetisation and obey the Curie-Weiss law instead of the Curie law (3.27). Weiss proposed that the magnetic moments interact with each other. This interaction can be described in terms of a fictitious internal field, called the molecular field or exchange field H_E, which is directly proportional to the magnetisation, *i.e.*

$$H_E = \lambda M, \tag{3.28}$$

where λ is the molecular field constant, independent of temperature.[166-168]

If we consider the paramagnetic phase, then an applied field H_a will cause a finite magnetisation and this in turn will cause a finite exchange field H_E. Then the magnetisation can be expressed as

$$M = \chi_p(H_a + H_E), \tag{3.29}$$

where χ_p is the paramagnetic susceptibility:

$$\chi_p = \frac{C}{T}. \tag{3.30}$$

Substituting (3.28) in (3.29) and using (3.30), we obtain $MT = C(H_a + \lambda M)$ and a susceptibility

$$\chi = \frac{M}{H_a} = \frac{C}{T - C\lambda} = \frac{C}{T - T_C}, \tag{3.31}$$

where $T_C = C\lambda$ is called the asymptotic or paramagnetic Curie temperature. The relation (3.31) is known as the Curie-Weiss law. This law applies to systems of interacting atoms or ions. The Curie law (3.27) describes instead the behaviour of an ideal paramagnetic system where there are no exchange or dipolar interactions among the magnetic moments. The Curie-Weiss law explains the divergence of the magnetic susceptibility (χ) at $T = T_C$ rather than $T = 0$. The divergence of the susceptibility at this temperature implies that there exists a nonzero magnetisation in a zero applied field (H_a), which corresponds to the definition of the Curie temperature (T_C). Below this temperature ($T < T_C$), the internal field dominates thermal effect and the magnetic moments are in an ordered state (ferromagnetic). At $T > T_C$, the thermal energy ($k_B T$) overcomes the interaction energy, randomising the moments and leading to a transition from a ferromagnetic to a paramagnetic state.

In order to explain the demagnetised condition of a ferromagnetic substance, Weiss proposed that the demagnetised state is divided into a number of spontaneously magnetised small regions called domains. These domains are magnetised in different directions in such way that as a whole the net magnetisation is zero. When an external field is applied, then the domains start to rotate and align with the applied field.

Even though the Weiss molecular field theory can describe the spontaneous magnetisation and different magnetisation states successfully, the physical origin of the molecular field is still unstated. In 1928 Heisenberg showed that the exchange interaction, which involves large (Coulomb) electrostatic energies, is responsible for the large molecular field.[166] The exchange energy between two adjacent spins S_i and S_j at an angle φ can be expressed as

$$E_{ex} = -2J_{ex}S_iS_j = -2JS_iS_jcos\varphi, \tag{3.32}$$

where J_{ex} is the exchange integral or overlap integral.[166] This exchange interaction decays exponentially with distance, but it is very strong to orient neighbouring magnetic moments at room temperature. For ferromagnetism to occur, J_{ex} should be positive. This reaches a minimum when the spins are all aligned. Some well-known ferromagnetic materials that exhibit easily detectable magnetic properties (to form magnets) are nickel, iron, cobalt, gadolinium and their alloys.[169]

3.2.4 Antiferromagnetism

If the exchange integral is negative, *i.e.* $J_{ex} < 0$, then the exchange energy is minimized when the neighbouring magnetic moments are aligned antiparallel with respect to their nearest neighbours, yielding no net

macroscopic magnetisation below a certain critical temperature. This magnetic behavior is called antiferromagnetism. An antiferromagnet can be described in terms of two interpenetrating sublattices (*e.g.* A and B) with magnetic moments pointing in opposite directions, giving a zero magnetisation below a critical temperature. The susceptibility increases as temperature decreases but goes through a maximum at a critical temperature called Néel temperature (T_N) and follow the Curie-Weiss law but with a negative value of θ:

$$\chi_m = \frac{C}{T-(-\theta)}. \tag{3.33}$$

Below the Néel temperature (T_N), the thermal energy is low, so the moments tend to align antiparallel even in the absence of an external magnetic field. This tendency of the spins to align antiparallel becomes stronger as the temperature decreases further. At absolute zero temperature each sublattice aligns perfectly antiparallel to reach a minimum net magnetisation. Common examples of materials with antiferromagnetic ordering include MnO, FeO, CoO and NiO.[165,169,170]

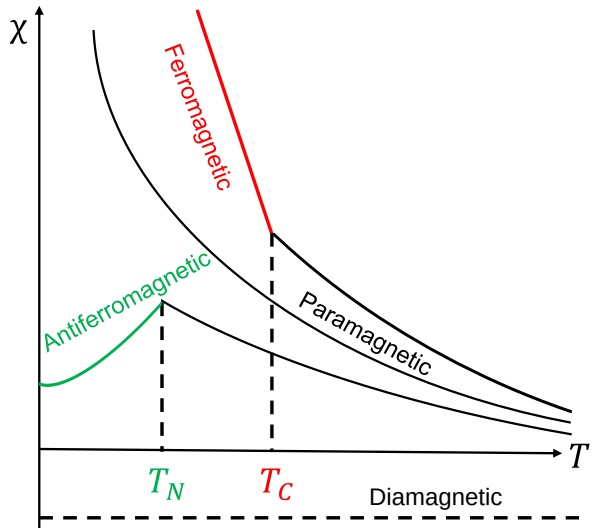

Figure 3.7 Dependence of the magnetic susceptibility (χ) on temperature for different types of magnetic materials.

3.2.5 Ferrimagnetism

When two sublattices are aligned antiparallel with each other and the magnitude of their magnetisation is different, then the net magnetization is non-zero. This phenomenon is known as ferrimagnetism. Ferrimagnetic materials consist of magnetic domains and exhibit magnetic saturation and hysteresis like ferromagnets. Above a certain critical temperature, their spontaneous magnetisation disappears and they become paramagnetic. The temperature at which this occurs is called Curie temperature (T_C). However, the temperature dependence of the magnetisation can be complicated since the temperature dependence of the spontaneous magnetisation for the individual sublattices can be quite different. Therefore, the magnetic susceptibility does not follow the Curie-Weiss law.[165] Ferrimagnetism mainly occurs in magnetic oxides known as ferrites with the chemical formula $MOFe_2O_3$, where M is a divalent cation (*e.g.* Zn^{2+}, Co^{2+}, Ni^{2+}, *etc.*).[165,169] Another family of ferrimagnets consists of garnets with the chemical formula $R_3Fe_5O_{12}$, where R is the trivalent rare earth atom.[165]

3.3 Magnetic anisotropy

The magnetisation of a magnetic material can have a preferential direction known as easy axis. Depending on the orientation of the applied magnetic field a lower (easy axis) or higher (hard axis) magnetic field can be required to reach the saturation magnetisation. This property is called magnetic anisotropy. There are several types of magnetic anisotropy: magnetocrystalline anisotropy, shape anisotropy, strain anisotropy, *etc.* due to the crystal symmetry, dipolar interactions between spins, geometry and shape of the sample, internal

and external strain, *etc*.[166] This section describes different types of magnetic anisotropy.

3.3.1 Magnetocrystalline anisotropy

Magnetic crystals possess a magnetic easy axis and a hard axis. Along certain crystallographic directions, it is easy to magnetise the crystal (easy axis). The difference in energy of a state between the easy direction and the hard direction is called the magnetocrystalline anisotropy energy.

The magnetic anisotropy energy for a material with a single easy axis perpendicular to the hard axis is often expressed as

$$E_a = \sum_{n=1}^{\infty} K_{un} sin^{2n}\theta = K_{u1} sin^2\theta + K_{u2} sin^4\theta + \cdots \approx K_{u1} sin^2\theta, \quad (3.34)$$

where θ is the angle between the magnetisation and the easy axis, and K_{un} are the anisotropy constants in the unit of J/m^3.[166]

A quantitative measure of the strength of the magnetocrystalline (or any other) anisotropy is the anisotropy field H_a, defined as the field needed to saturate the magnetisation of a uniaxial crystal along the hard direction. If a magnetic field (H) is applied to a ferromagnetic material system perpendicular to the easy axis, then the total energy can be expressed as

$$E = K_u sin^2\theta + HM_s \cos\left(\frac{\pi}{2} - \theta\right) = K_u sin^2\theta + HM_s \sin\theta, \quad (3.35)$$

where M_s is the saturation magnetisation. The anisotropy field can be expressed as

$$H_a = \frac{2K_u}{M_s}. \quad (3.36)$$

The magnetocrystalline anisotropy energy is smaller in lattices with higher symmetry and larger in lattices with lower symmetry and is usually in the range $10^2 – 10^7$ J/m^3.[165]

3.3.2 Shape anisotropy

Shape anisotropy is a magnetostatic phenomenon wherein the direction of the magnetisation is determined by the magnetostatic energy. In the case of a spherical shape specimen with no net crystal anisotropy, an applied field can magnetise the specimen in any direction. Thus there is no shape anisotropy for a spherical shaped object. However, it is easier to magnetise a non-spherical shape specimen along a long axis than a short axis since the demagnetising field along the long axis is weaker than along a short axis. Thus the shape of the sample can be a source of magnetic anisotropy and the sample is said to exhibit shape anisotropy. This anisotropy attempts to minimise the magnetic field outside the sample. Thus the magnetisation would prefer to orient along the long side of the sample. In the case of a thin sample, since the out of plane magnetisation would cause a high density of demagnetising field, the shape anisotropy leads to an energetic saving by keeping the magnetisation in the plane of the sample.

The shape anisotropy arises from dipole interactions at the surfaces of the sample. Quantitatively, the magnetostatic or self-energy of a sample in its demagnetising field (H_d) is given by[166]

$$E_{ms} = -\frac{1}{2}\int_V \mu_0 \boldsymbol{H_d}.\boldsymbol{M} dv, \tag{3.37}$$

where dv is an incremental volume. Equation (3.37) can be expressed as

$$E_{ms} = \frac{1}{2}\mu_0 N_d M^2 \ \ (\text{J/m}^3), \tag{3.38}$$

where $H_d = N_d M$ and N_d is the demagnetising coefficient.

For a prolate spheroid magnetised to a value M at an angle θ to the semi-major axis c, the shape anisotropy energy can be expressed as

$$E_{ms} = \frac{1}{2}\mu_0 M^2 N_c + \frac{1}{2}\mu_0 (N_a - N_c) M^2 sin^2\theta, \tag{3.39}$$

where N_c and N_a are the demagnetising coefficients along the semi-major axis (c) and semi-minor axis (a) of the prolate spheroid, respectively. This magnetostatic energy has an angle dependent term of exactly the same form as the uniaxial crystal anisotropy energy (3.34). Here the semi-major axis plays the same role as the easy axis of the crystal. The shape anisotropy constant is

$$K_s = \frac{1}{2}\mu_0 (N_a - N_c) M^2 \quad \text{J/m}^3. \tag{3.40}$$

Equation (3.40) is often written as

$$K_s = \frac{1}{2}\mu_0 \Delta N M^2 \quad \text{J/m}^3. \tag{3.41}$$

The magnetisation is easy along the c-axis and hard along any other axis perpendicular to it. It can be seen that for a spherical shape specimen for which $c = a$, then $N_c = N_a$, thus $K_s = 0$ *i.e.* the shape anisotropy disappears.

3.3.3 Strain anisotropy

When a magnetic material is exposed to a magnetic field, it is subjected to a change in its crystal lattice. This effect is called magnetostriction and causes a change in the magnetic properties of the material due to spin-orbit coupling. The energy associated with this change in the dimension of the material is called

the magnetoelastic anisotropy energy. This energy depends on a constant called magnetostriction coefficient (λ) expressed as

$$\lambda = \frac{\Delta l}{l}, \tag{3.42}$$

where Δl is the change in length (l) of the material in the presence of magnetic field while maintaining the volume constant.[166] Very often the value of λ is measured at the saturation of the magnetic field from the ideal demagnetised state and then is called the saturation magnetostriction (λ_{si}). Since the magnetostriction is an anisotropic property, the value of λ_{si} is different in different directions of the crystal axes and can be positive or negative. For the ideal demagnetised state along the magnetisation direction in a uniaxial crystal, the magnetostriction is expressed as[166]

$$\lambda_{si} = \lambda_A[(1-\alpha_3^2)^2 - (1-\alpha_3^2)\alpha_3^2] + 4\lambda_D(1-\alpha_3^2)\alpha_3^2, \tag{3.43}$$

where λ_A and λ_D are the magnetostriction constants, and α_3 is the direction cosine of the saturation magnetisation relative to the crystal c-axis.

3.4 Magnetisation dynamics

In the presence of a magnetic field $\boldsymbol{B_{eff}}$, the magnetisation $\boldsymbol{M}$ of a ferromagnetic material experiences a torque given by

$$\boldsymbol{\tau} = \boldsymbol{M} \times \boldsymbol{B_{eff}}. \tag{3.44}$$

According to Newton's classical equation of motion, the rate of change of the angular momentum is

$$\frac{d\boldsymbol{L}}{dt} = \boldsymbol{\tau} = \boldsymbol{M} \times \boldsymbol{B_{eff}}. \tag{3.45}$$

The magnetisation $\boldsymbol{M}$ and the angular momentum $\boldsymbol{L}$ are related by

$$\boldsymbol{M} = \gamma \boldsymbol{L}, \tag{3.46}$$

where $\gamma = \frac{g\mu_B}{\hbar}$ =1.75×10^{11} s^{-1}T^{-1} is the gyromagnetic ratio. Using (3.46), the equation of motion for the free, undamped precession of the magnetisation around the effective field can be rewritten as

$$\frac{d\boldsymbol{M}}{dt} = -\gamma\left(\boldsymbol{M} \times \boldsymbol{B_{eff}}\right). \tag{3.47}$$

Thus the magnetisation precesses around the effective field with the classical Larmor frequency

$$\nu = \left|\frac{\gamma B_{eff}}{2\pi}\right|. \tag{3.48}$$

If there is no loss or damping, then the magnetisation only precesses about the field and never aligns with the field. However, in reality, after a sufficient time, the magnetisation aligns with the field due to damping. To account for this damping, Gilbert extended the Landau-Lifshitz equation of motion to[171]

$$\frac{d\boldsymbol{M}}{dt} = -\gamma\left(\boldsymbol{M} \times \boldsymbol{B_{eff}}\right) + \frac{\alpha}{M_s}\left(\boldsymbol{M} \times \frac{d\boldsymbol{M}}{dt}\right). \tag{3.49}$$

Equation (3.49) is known as Landau-Lifshitz-Gilbert (LLG) equation, where α is the phenomenological damping constant or Gilbert damping parameter, which accounts for different dissipative processes.

The first term in (3.49) describes the precession of $\boldsymbol{M}$ around the effective field $\boldsymbol{B_{eff}}$, which includes the external ($\boldsymbol{B_{ext}}$), anisotropy ($\boldsymbol{B_{ani}}$) and microwave ($\boldsymbol{B_{MW}}$) fields as

$$\boldsymbol{B_{eff}} = \boldsymbol{B_{ext}} + \boldsymbol{B_{ani}} + \boldsymbol{B_{MW}}. \tag{3.50}$$

The second term in (3.49) represents the damping term, which describes the damping of the precessional motion of $\boldsymbol{M}$. Due to this damping, the precessing magnetisation spiral in towards the effective field direction and thus changes its angular momentum. The damping can arise from phonon drag mechanisms, magnon scattering, induction of eddy currents due to the precessional motion, etc.[172,173]

3.5 Electron spin resonance (ESR)

This section describes the basic principles of electron spin resonance (ESR) based on the absorption of microwave radiation by unpaired electron spins aligned with a magnetic field.

For a system with one unpaired electron ($S = 1/2$), there are two spin states with spin quantum number $m_s = +1/2$ and $m_s = -1/2$, which are non-degenerate when placed in an applied magnetic field. The interaction between the spin and the magnetic field is described by the Zeeman effect:

$$E = g_e \mu_B B, \tag{3.51}$$

where g_e is the electron's g-factor, μ_B is the Bohr magneton, and B is the applied magnetic field.[174]

The magnetic field lifts the degeneracy of the spin states. The spin state with spin quantum number $m_s = +1/2$ rises in energy with increasing B. In contrast, the spin state with spin quantum number $m_s = -1/2$ decreases in energy with increasing B. When photons of energy $h\nu$ matches the energy separation of the two spin states, an absorption occurs. This absorption causes a transition between the two spin states, which is governed by the selection rules $\Delta m_s = \pm 1$ and $\Delta m_I = 0$, where m_I is the nuclear magnetic quantum number.

This transition can be detected in absorption studies when the resonance condition is met, *i.e.*

$$h\nu = g_e \mu_B B. \tag{3.52}$$

The field at which the resonance condition is met is called the 'resonance field'. However, an unpaired electron will respond not only to the applied magnetic field B but also to the local magnetic fields due to the surroundings atoms. Therefore, the effective magnetic field B_{eff} experienced by the unpaired electron is

$$B_{eff} = B(1 - \sigma), \tag{3.53}$$

where σ includes the local fields and can be either positive or negative. Therefore, the resonance condition can be rewritten as

$$h\nu = g_e \mu_B B(1 - \sigma) = g\mu_B B, \tag{3.54}$$

where $g = g_e(1 - \sigma)$ is called the g-factor.

So far we have considered the $S = 1/2$ spin system. However, for a system with $S = 3/2, 5/2, etc.$, there exists an extra magnetic interaction called zero-field interaction between the individual unpaired electrons, which is independent of the external field. The sub-levels of the spin multiplet group in pairs (called Kramer pairs) and are separated by an energy called zero-field splitting.[175] In the presence of an external field, the degeneracy between the pairs is lifted and the external field induces a splitting. Several ESR transitions within each Kramer's pair can be observed at different magnetic fields provided that selection rules are satisfied. Thus one might obtain more than one ESR transition and different g-values.

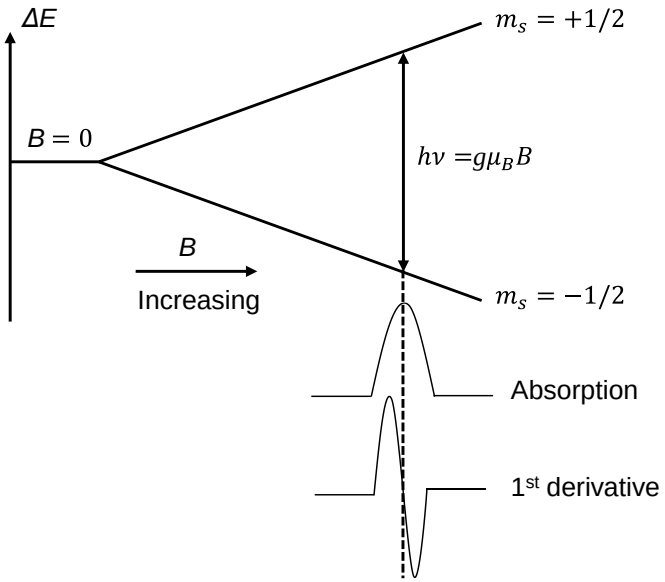

Figure 3.8 Sketch of the energy levels splitting for a single unpaired electron with magnetic field. The inset shows the typical absorption and the 1st derivative ESR signal when the resonance condition is met.

Equation (3.54) is used to determine the value of g by measuring the field and the frequency at which the resonance occurs. This can be done by either varying the photon frequency, keeping the field fixed, or varying the field, holding the photon frequency fixed by using an electron spin resonance spectrometer. The g value helps to distinguish and identify different types of magnetic behaviours.[174] More generally, the ESR is a very useful technique to study magnetic properties and identify magnetic phase transitions. Moreover, angular dependence ESR studies offer the opportunity to determine the magnitude and direction of the uniaxial magnetic anisotropy for ferromagnetic samples.[176] We have employed this technique to study magnetic properties of InSe crystals containing ferromagnetic Fe-islands, as discussed in chapter 7.

Chapter 4

Sample fabrication and characterisation techniques

This chapter describes the sample preparation and different experimental techniques used to study structural, optical, magnetic and transport properties.

4.1 Growth of bulk InSe

The bulk γ-polytype InSe layers with and without transition metals were grown by the Bridgman method from a polycrystalline powder of $In_{1.03}Se_{0.97}$ at the Institute for Problems of Materials Science, Ukraine by Professor Z. D. Kovalyuk and Dr. Z. R. Kudrynskyi. In the Bridgman method,[177] a polycrystalline powder of non-stoichiometric $In_{1.03}Se_{0.97}$ is placed inside a quartz ampoule and sealed under high vacuum. Then this ampoule is inserted into the Bridgman furnace and heated above the melting point of the polycrystalline powder. When the powder melts and becomes homogeneous, then the ampoule is slowly moved in the low temperature region of the furnace. Thus the melt starts cooling and crystallizing at the tip of the ampoule. The crystallised sample is left to cool for several days. For the Fe or Mn-doped InSe crystals, Fe or Mn-dopants (Fe/Mn) were incorporated during the Bridgman growth of InSe at a nominal concentration of 1 and 10% for Fe, and 0.5% for Mn. The distribution of the Fe/Mn impurities along the length of the ingot was inhomogeneous with the largest Fe/Mn content at the end of the ingot. Slices of the ingot were cut perpendicular to the growth axis at different positions to

achieve different concentrations of Fe/Mn. The slices from the end of the ingots were used in the experiments.

An alternative method of incorporating transition metals (*e.g.* Ni) in InSe is by electrochemical intercalation.[178] In this case, the pristine InSe grown by the Bridgman method was immerged in an electrolyte containing a saturated aqueous solution of a transition metal (Ni) ion salt. The InSe crystal acted as a cathode. A magnetic field was applied parallel to the vdW planes of the InSe crystal. Due to the presence of magnetic field gradient, the transition metal ions were pulled inside the InSe layers from the electrolyte solution, becoming localised in the vdW gaps.

The crystal structure of the crystals was studied by X-ray diffraction (XRD) using a DRON-3 X-ray diffractometer that uses monochromatic Cu-Kα radiation of wavelength λ = 1.5418 Å.

4.2 Mechanical exfoliation of InSe

Discovery of monolayer graphene by mechanical exfoliation has opened up the door to the exfoliation of many other vdW semiconductor crystals, enabling the observation of their two-dimensional properties and fabrication of different types of heterostructures.[3] The exfoliation technique makes use of a low residue adhesive tape to peel the nanoflakes from a bulk crystal. In our work, InSe and InSe:Fe vdW bulk crystals were exfoliated either using a low residue adhesive tape or a polydimethylsiloxane (PDMS) polymer, depending on their further uses. To characterise the exfoliated flakes by atomic force microscope (AFM), photoluminescence (PL) and Raman spectroscopy, adhesive tape was used for the exfoliation and the exfoliated flakes were directly

transferred onto a SiO_2/Si substrate. Figure 4.1 illustrates the mechanical exfoliation technique and an optical image of InSe flakes. To fabricate InSe/graphene/hBN/SiO_2/Si hybrid devices, graphene/hBN layers were exfoliated by mechanical exfoliation using a low residue adhesive tape or a PDMS polymer and then transferred onto a desired SiO_2/Si substrate. Also, to fabricate these devices we used graphene grown on copper foil by chemical vapour deposition (CVD). Before the fabrication of the devices, the CVD graphene was transferred from copper foil to a SiO_2/Si substrate, as described in section 4.3.1. In both cases, single layer graphene was patterned into multi-terminal Hall bars (described in section 4.3.2). To complete the desired device structures (graphene capped by InSe), InSe nanoflakes were exfoliated using a PDMS polymer and then an isolated flake of InSe was transferred onto half of a pre-patterned graphene Hall bar by dry transfer, as described in section 4.3.3.

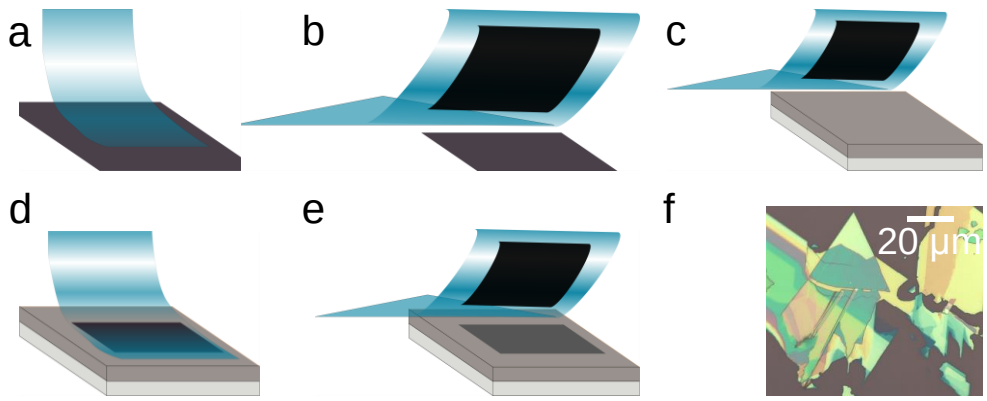

Figure 4.1 (a)-(e) Different steps during the mechanical exfoliation of vdW crystals using low adhesive tape. (f) Optical image of exfoliated nanoflakes.

4.3 Device fabrication

Graphene layers grown on copper foil by a chemical vapour deposition (CVD) technique were supplied by A. J. Marsden and Dr. N. R. Wilson from the University of Warwick, Dr. A. Mishchenko from the University of

Manchester, and Graphenea. All the graphene-based InSe/graphene heterostructure devices were fabricated by Dr. Z. R. Kudrynskyi and myself at the University of Nottingham, except for the exfoliated graphene-based devices, which were provided by Professor K. S. Novoselov from the University of Manchester. About 50 devices were fabricated by using the techniques described below.

4.3.1 Transfer of CVD graphene

The graphene surface of the graphene-copper stack was spin coated by a single layer of poly (methyl methacrylate) resin (PMMA) (5% in anisole) at 4000 rpm for 60s and left on a preheated hot plate at T = 180 ^{o}C for 10 minutes to partially bake the PMMA. The PMMA-graphene-copper stack was then left to cool to room temperature for a few minutes. This stack was placed on the surface of an $FeCl_3$ etchant (Transene, CE-100), which removed the copper substrate from the PMMA-graphene stack. PMMA provided the support to the graphene to float on the etchant surface. The PMMA-graphene film was then placed in an HCl bath and then rinsed many times in deionised water for few hours. The floating PMMA/graphene film was scooped out of water by an ultrasonically cleaned SiO_2/Si substrate, which was already pre-patterned with gold alignment marks. The PMMA/graphene film on the substrate was left to dry for 1-2 days under ambient conditions.

The dried PMMA-graphene-SiO_2/Si substrate was immersed in acetone at T = 60 ^{o}C for 10 minutes and rinsed by isopropyl alcohol (IPA) to remove the PMMA layer from the stack and dried by air blow. The graphene layer on the SiO_2/Si substrate then became ready for the patterning of graphene Hall bars (Figure 4.2).

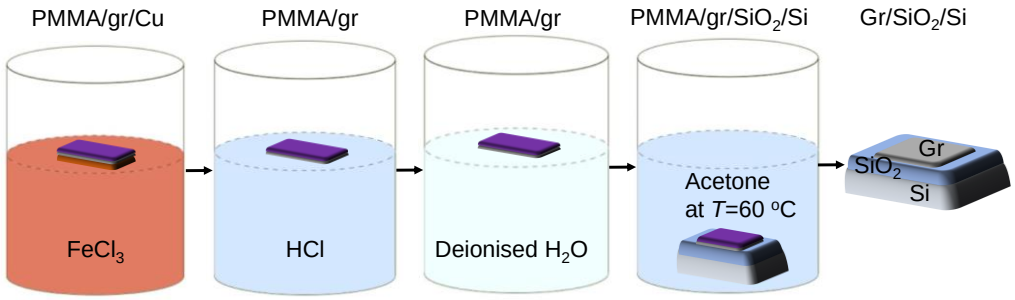

Figure 4.2 Flow chart of CVD graphene transfer onto a SiO_2/Si substrate.

4.3.2 Patterning graphene Hall bar and making contacts

Multi-terminal Hall bars were fabricated using exfoliated graphene on hBN/SiO_2/Si and CVD graphene on SiO_2/Si. In both cases, the graphene-substrate stack was spin coated first by PMMA (8% in anisole) at 4000 rpm for 30s and baked partially on a preheated hot plate at T = 180 ^oC for 10 minutes and then left to cool to room temperature before further spin coated by PMMA (2% in anisole) with the same parameters. This bi-layer of PMMA was used as a high resolution positive resist for electron beam lithography (EBL) of multi-terminal graphene Hall bars. The electron beam exposure breaks the polymer chains and those broken and shorter chain molecules are removed by development in an IPA:deionised water (70:30) solution, leaving unaffected the unexposed PMMA-graphene. The sample was etched by oxygen plasma to remove any graphene from the exposed area and left in acetone at T = 60 ^oC to remove the unexposed PMMA layer from the top of graphene, producing a multi-terminal graphene Hall bar.

After patterning the graphene as a multi-terminal Hall bar by EBL and oxygen plasma etching, a dual layer of PMMA was formed by spin coating PMMA (8% and 2% in anisole respectively). This dual layer PMMA acted as a positive resist to the electron beam exposure for patterning the electrode contacts. The exposure was followed by development in IPA:deionised water

(70:30) solution, which removed the polymer from the exposed region and left the unexposed PMMA. This unexposed PMMA acted as a mask for the conventional metal deposition by a thermal evaporation technique.

The metal deposition was carried out by loading the masked graphene/substrate into an Edwards Auto 305 thermal evaporator. At a typical deposition rate of 0.30-0.45 nms^{-1}, a Au/Ti (100/10 nm) bilayer was deposited and left for several minutes to cool to room temperature. The deposition of Au/Ti bilayer was followed by the lift-off procedure. The Au/Ti/PMMA/graphene/substrate was immersed in acetone at $T = 60\ ^{o}C$ for ~1-2 hours to remove unexposed PMMA as well as the excess Au/Ti. The Au/Ti/graphene/substrate was then further rinsed by IPA and dried by air blow. Immediately before forming the InSe/graphene heterostructures, the Hall bar device was annealed in an Ar:H (95:5) mixture at 200-400 ^{o}C for 3-4 hours to remove the remaining residues of the electron-beam resist.

4.3.3 Dry transfer of InSe on graphene

A deterministic transfer set up was constructed to fabricate heterostructures, see Figure 4.3. InSe nanoflakes were exfoliated by using a PDMS polymer, which was adhered on a microscope glass slide by a two sided tape. An isolated flake was identified by the optical microscope. This was followed by the photoluminescence (PL) measurements (discussed in section 4.5) to determine the thickness of the flake from the PL peak energy. The microscope glass slide was attached to a moveable transfer arm with the flakes facing down above the graphene Hall bar. A double-sided polymide tape was used to mount the substrate on top of a copper plate. The copper plate was mounted on top of a motorised translational and rotational stage. This enabled

to align and control the position of the substrate precisely, as required. Also, the alignment of the exfoliated isolated flake was carried out by the hand controlled *x*-, *y*- and *z*- micrometer of the transfer arm and observed through an optical microscope. When both the substrate and the desired flake on the microscope glass slide were aligned in the *xy*-plane, the desired exfoliated flake was brought into contact with the substrate very slowly by adjusting the *z*-micrometer. The *z*-micrometer was then adjusted to peel the stamp from the substrate and complete the transfer of the desired isolated flake from the stamp onto the target graphene Hall bar on the substrate.

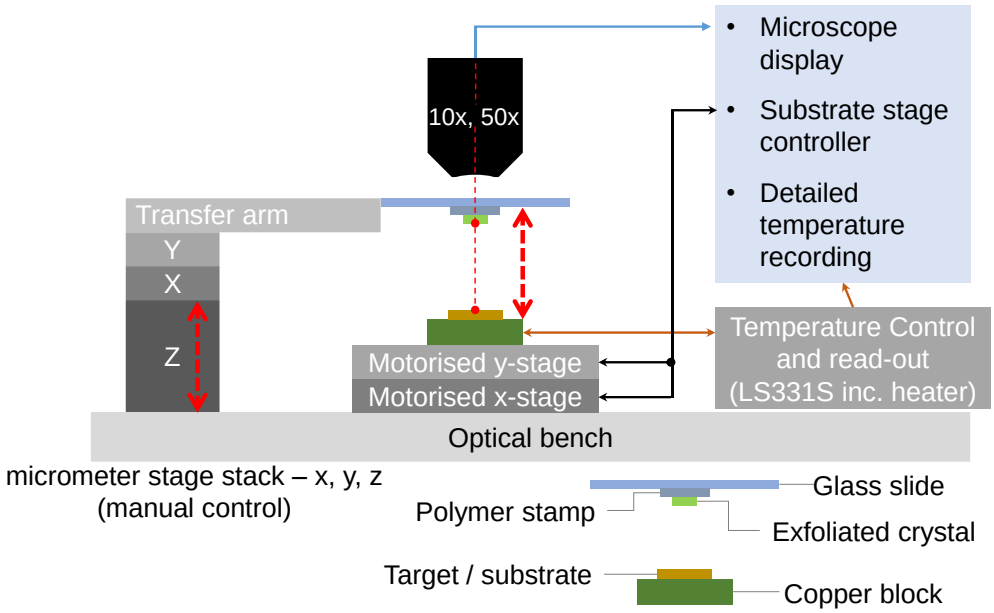

Figure 4.3 Diagram of the deterministic transfer set-up. The target substrate is placed on a copper plate mounted on a motorised xy-stage. The exfoliated flakes on PDMS are attached on a microscope glass slide fixed with the transfer arm. The alignment of the target substrate and the flake underneath the optical microscope can be controlled manually or through a software.

In the assembled InSe/graphene heterostructure, only half of the graphene 10-terminal Hall bar device was capped with an InSe flake and the rest of it remained uncapped. The voltage probes on the uncapped half of the graphene layer provide us with a "control sample". The two halves of the device

are in a "series" resistance configuration with the same electrical current flowing through both of them. Such configuration made it possible to conduct optoelectronic and magneto-transport measurements on each part of the device independently in order to reveal the effect of the InSe flake on the properties of graphene. A typical InSe/graphene hybrid structure is shown in Figure 4.4a (schematic) and 4.4b (optical image). The device was then mounted on a suitable header and wire-bonded. We have fabricated a series of devices with InSe layers of thickness between 10 to 50 nm.

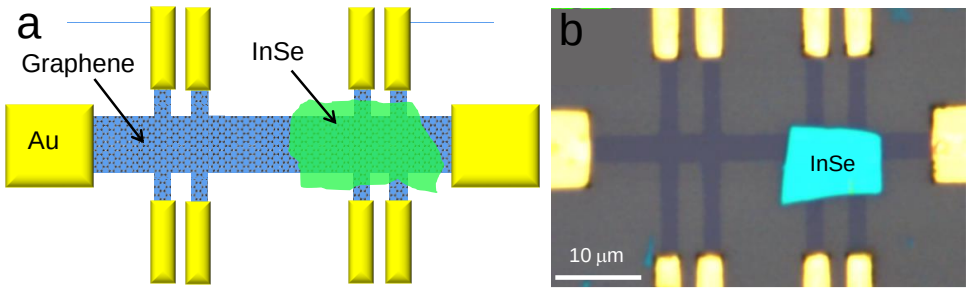

Figure 4.4 (a) Schematic and (b) optical image of a multi-terminal graphene Hall bar device. One half (right) of the Hall bar is capped by an InSe layer.

4.4 Transmission electron microscopy (TEM) and energy dispersive X-ray (EDX) spectroscopy

Transmission electron microscopy (TEM) experiments were conducted by Dr. M. W. Fay and myself in the Nanoscale and Microscale Research Centre (nmRC) at the University of Nottingham using a JEOL 2100F microscope operating at 200 kV, equipped with a Gatan Orius camera and Oxford Instruments X-Max 80 60x detector. For these studies, we used thin layers of InSe crystals with and without Fe prepared by Dr. C. Parmenter and myself using Focused Ion Beam (FIB) Scanning Electron Microscope, SEM (FEI Quanta 3D) at the nmRC. To prepare the thin sample, a layer of Pt was deposited on top of the cross-section of the bulk sample using methylcyclopentadienyl

platinum trimethyl from a gas injector. Three sides of the bulk material around the deposited Pt layer were etched by tilting the sample by up to 52° such that these three sides of the chosen region (lamella) were cut and detached from the bulk part of the material. A micromanipulator (omniprobe) was inserted and positioned onto one of the detached sides of the lamella so that it touched the corner of the lamella. Pt was deposited in order to weld the omniprobe to the lamella. The uncut side of the sample was then etched by using a Ga ion beam to fully detach the lamella from the bulk material and the micromanipulator with the lamella was retracted, which completed the lift-out. The lift-out was then followed by the transfer of the lamella to a suitable TEM support grid. The lamella welded to the micromanipulator was brought into contact with the commercially available TEM grid especially designed to be used with *in situ* micromanipulator. Then the sample was welded to the grid via Pt deposition and the link between the omniprobe and the lamella was cut. Finally, the attached lamella to the TEM grid was thinned down (~ 100 nm) by using a Ga ion beam at 30 kV and a current of ~ 30 to 200 pA.

SEM Energy-dispersive X-ray (EDX) studies were performed on the crystals using a FEI Quanta 650 operating at 20 kV, equipped with an Oxford Instruments X-Max 150 detector. A high energy focused electron beam was shone on the surface of thin layers. In addition to the transmitted electron beam, the interaction between the high energy electrons and atoms of the sample create backscattered electrons and X-rays, which were collected and analysed to probe topological, morphological and compositional properties (Figure 4.5).

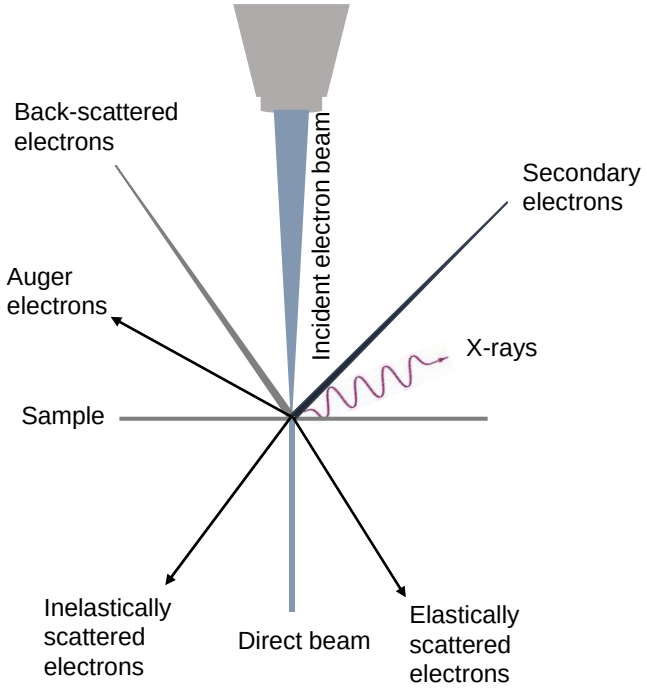

Figure 4.5 Signals generated from the interaction between a high energy electron beam and a very thin electron transparent sample. Picture reproduced from Ref [179].

4.5 Micro-photoluminescence and Raman spectroscopy

Micro-Photoluminescence (μ-PL) is an essential tool for the investigation of optical processes in a semiconductor sample. If the sample is excited by a laser with an energy greater than the bandgap, electron-hole pairs are generated. These electron-hole pairs can recombine via various available paths. For example, in an ideal semiconductor, with no energy levels inside the forbidden energy gap, electrons and holes recombine from the bottom edge of the conduction band and top of valence band, respectively, as shown in Figure 4.6a. The energy of this band to band transition is equal to the energy gap of the material whenever the Coulomb interaction in an electron-hole pair, or excitonic interaction, is weak.[179] However, in most semiconductors, this interaction is not negligible and the dominant feature in the PL spectrum is associated with the recombination of free excitons, as shown in Figure 4.6b. Along with these

transitions, the presence of defects, impurities and bound excitons can result in the formation of new energy states within the forbidden gap, resulting in additional optical transitions (Figure 4.6c, d and e). In these recombination processes, the electrons return to the ground state by emitting photons of energy $h\nu$. The intensity of each transition versus energy $h\nu$ represents the photoluminescence spectrum.

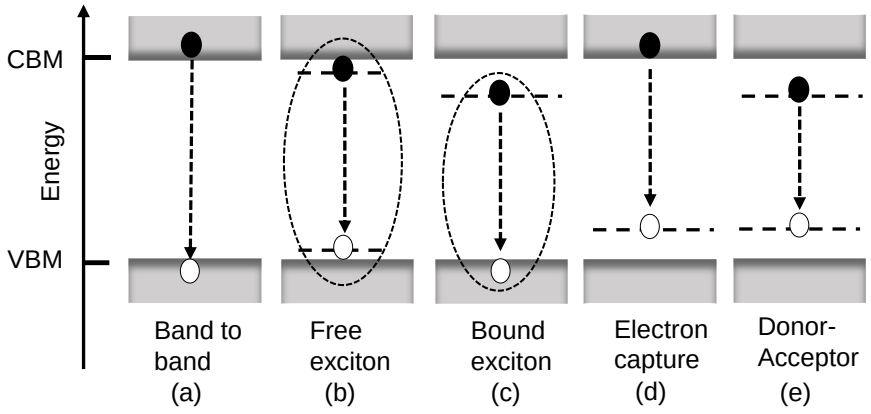

Figure 4.6 Main recombination processes in photoluminescence for (a) band-to-band; (b) free exciton; (c) bound exciton; (d) electron capture and (e) donor-acceptor transitions. Figure reproduced from Ref [179].

Micro-Photoluminescence (μ-PL) and Raman spectroscopy measurements were performed on our samples using a LabRAM HR-UV spectrometer equipped with a confocal microscope, excitation laser optics and a *XYZ* motorized stage (Figure 4.7a). The samples were mounted on the *XYZ* motorized stage and excited either by a He-Ne (λ = 633 nm) or frequency doubled Nd:YVO4 (λ = 532 nm) laser. The laser beam was focused by an objective of focal length 1.8 mm and numerical aperture 0.9 with 100x optical magnification, which provided a beam diameter of $<$ 1 μm on the sample surface. The same objective collected the photo excited light from the sample and sent it through an adjustable pinhole aperture. This pinhole aperture blocked the signal from the area outside the sampling area and focal plane, thus allowing

high spatial resolution in the optical imaging studies. The μ-PL signal was dispersed by a grating of either 150 g/mm or 1200 g/mm depending on the required wavelength range and spectral resolution, and was detected by a Si charge coupled device (CCD) (detection range from λ = 350 nm to 800 nm) or a liquid nitrogen cooled (InGa)As (detection range from λ = 800 nm to 1600 nm) array photodetector.

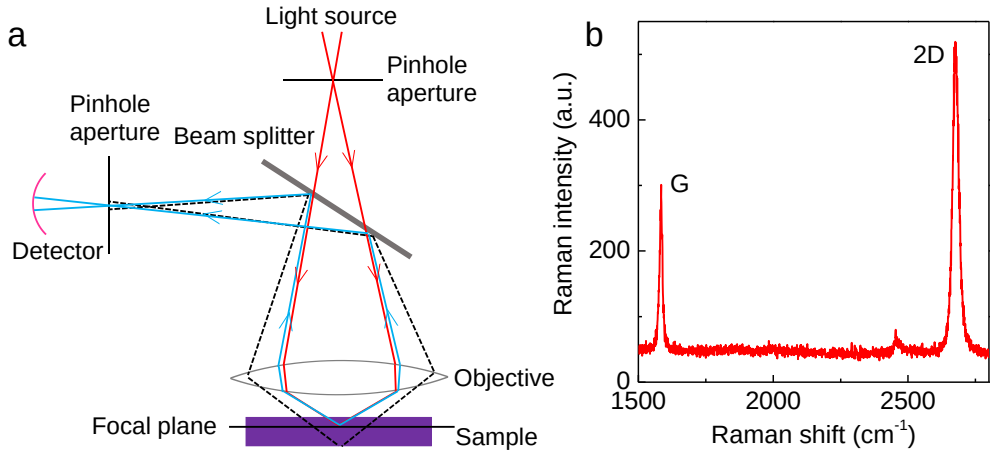

Figure 4.7 (a) Confocal microscope for micro-photoluminescence and micro-Raman spectroscopy studies. (b) Typical micro-Raman spectrum of single layer graphene showing the G-mode and the 2D-mode.

The motorized *XYZ* stage allows μ-PL maps of the samples to be constructed by two different modes: *XYZ* motorized mode and *XYZ* scanlab. In the motorized mode, the stage moves point by point with a resolution of 0.1 μm with respect to the laser beam; in the second mode, the laser beam moves on the sample while the stage remains in the same position. The scanlab mode is useful for the samples in a fixed cryostat at low temperature but the range of mapping is limited due to the loss of focus when laser beam is tilted. We used the *XYZ* motorized mode to acquire μ-PL maps at room temperature.

Raman spectroscopy is based on the inelastic light scattering by phonons within a crystalline material. This enables the observation of vibrational and

rotational frequency modes of the crystal. In the scattering process, an incident photon excites a system from its lowest rotational and vibrational level to a virtual energy state for a short period of time. Upon relaxation, a photon is emitted along with the absorption or emission of a phonon. The resulting inelastically scattered photon can be of either lower or higher energy than the incident photon. Therefore, the energy of the emitted photon is shifted away from the excitation energy.

We use Raman spectroscopy to study single layer graphene and flakes of pristine InSe and InSe doped with transition metals. Figure 4.7b shows typical Raman spectra of single layer graphene. For these studies, we used the same μ-PL set up. The Raman peaks tend to be very sharp and close to the laser excitation energy. Thus a spectrometer grating of 1200 groove/mm was used for resolving low frequency Raman modes with high energy resolution. Usually, only 1 in 10^6 incident photons undergo inelastic scattering. The remaining photons undergo Rayleigh scattering, which produce an intense signal at the laser line. Thus to observe the weak Raman signal due to inelastic scattering, the laser line need to be filtered out. In our set up, this was achieved using an edge filter.

4.6 Atomic force microscopy (AFM)

The surface topography of nanoflakes transferred on a SiO_2/Si substrate were acquired in tapping mode under ambient condition using an MFP-3D AFM system. This AFM system has a sub-angstrom resolution in the *Z* direction and nanometer resolution in the *XY* plane. It consisted of a low spring constant ($k =$ 0.7-3.8 Nm^{-1}) cantilever with a sharp tip (radius=7-10 nm) at the end of the

cantilever, an infra-red laser and a four quadrant photodiode deflection sensor (Figure 4.8a). The cantilever oscillates up and down at its resonance frequency $\omega_0 =$ 50-90 kHz using a piezoelectric while the cantilever tip scans the sample surface. The frequency and amplitude of the driven signal can be kept constant, corresponding to a constant amplitude of the cantilever oscillation. The focused laser beam on the backside of the cantilever was reflected onto the photodiode, enabling to measure the oscillation of the tip and its distance from the surface. When the cantilever tip comes close to the sample surface, forces between the tip and the sample surface lead to a change in the amplitude of the cantilever oscillation, which can be monitored and controlled by the feedback system. A voltage is applied to the *Z* piezoelectric to return the tip to the reference height above the sample. This feedback voltage corresponds to a calibration factor, which enables to obtain a topographical map of the sample surface (Figure 4.8b).

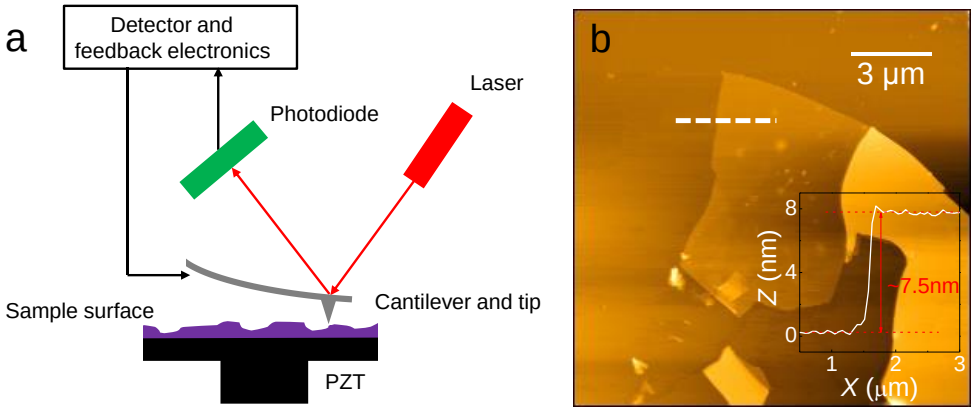

Figure 4.8 (a) Schematic diagram of an AFM system. (b) Acquired AFM image and corresponding *Z*-profile of an exfoliated InSe:Fe nanoflake.

4.7 Magnetic force microscopy (MFM)

Magnetic force microscopy (MFM) measurements were performed on a Dimension Icon (Bruker) scanning probe microscope (SPM) at the National

Physical Laboratory (NPL) by R. Puttock and Dr. O. Kazakova. The MFM probe (Nanosensor PPP MFMR) has a typical spring constant k = 2-3 N/m and curvature radius r < 30 nm. The measurements were conducted in the thermally demagnetized state of the crystals using a two-pass method and a CoCr-tip magnetized along the tip axis. During the first-pass, the SPM was operated in the atomic force microscopy mode to determine the topography. During the second-pass, the topography line obtained during the first-pass was retraced while oscillating the probe at a frequency f = 69.56 kHz (free-space amplitude $A_f \approx 200$ nm), maintaining a set distance of h = 25-50 nm between the probe and sample, and recording the cantilever phase change due to probe-sample magnetic interactions.[180,181] The scan across the sample was conducted at a rate of 0.7 Hz.

4.8 Electron spin resonance (ESR)

Continuous wave (CW) electron spin resonance (ESR) spectroscopy studies were performed in Q-band ($\nu = 34.229$ GHz) on a commercial Bruker EMX and E580 spectrometers by Dr. F. Moro and myself at the Photon Science Institute at the University of Manchester. The major components of this spectrometer are: a microwave generator, a sample cavity, an electromagnet and a detector (Figure 4.9a). The microwaves were supplied from the microwave bridge at a controlled frequency and power, and were transmitted to the sample cavity via a waveguide. The sample was placed in the sample cavity and irradiated with microwaves, which were critically coupled into the cavity via a hole called iris. The microwave field in the excitation of the TE mode was perpendicular to the dc magnetic field generated by an electromagnet. It was

possible to vary the magnetic field linearly over different magnetic field ranges in a controlled way. Along with the dc magnetic field, a smaller oscillating magnetic field was generated in the cavity via a Zeeman modulation coil. Thus the signal response from the cavity was modulated at the Zeeman modulation frequency. The ideal way to perform the ESR experiments would be to apply a fixed magnetic field and vary the microwave frequency. However, microwave generators are only tuneable over very limited frequency ranges. Thus the microwave frequency was fixed and the applied magnetic field was swept. When the sample absorbed microwave energy, then the coupling changed and therefore, the cavity was no longer critically coupled. Thus the microwaves were reflected back to the detector in the microwave bridge, resulting in an ESR signal (Figure 4.9b). This modulated signal containing the ESR information was fed directly into a computer for storage and subsequent data analysis.

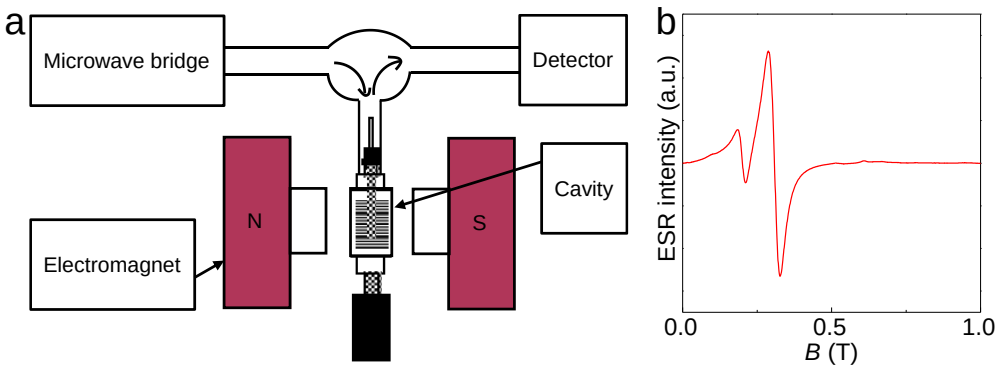

Figure 4.9 (a) Block diagram of a typical CW ESR spectrometer. (b) Typical ESR spectrum of bulk InSe:Fe crystal in *Q*-band (ν =34.229 GHz).

4.9 Magneto-transport measurements

Transport measurements were carried out by myself using a superconducting magneto-cryostat at magnetic fields *B* up to 14T at the University of Nottingham. Also, high magnetic field studies were carried out by

Dr. O. Makarovsky and Dr. Z. R. Kudrynskyi using a resistive magnet with B up to 30T at the European Magnetic Field Laboratory (EMFL, Grenoble).

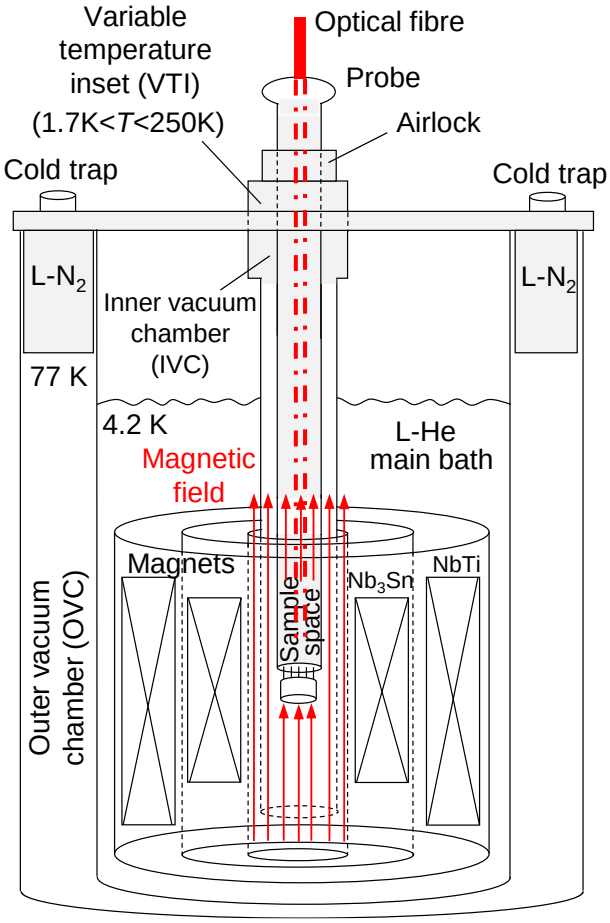

Figure 4.10 Sketch of the superconducting magneto-cryostat used for transport measurements.

The superconducting magneto-cryostat (Cryogenic Ltd) is capable of producing a field B up to 14T, see Figure 4.10. The core of the cryostat contains the superconducting magnet consisting of two coils, an inner section wound from a niobium-tin (Nb_3Sn) wire and an outer section consisting of a niobium-titanium (NbTi) wire. The magnet sits in the main bath, which is filled with liquid helium (L-He) at a constant temperature of $T = 4.2$K. The coils are superconducting at this L-He temperature with a current limit of 100 A, enabling to achieve $B = 14$T. The L-He main bath is insulated from the environment by an outer vacuum chamber (OVC) kept at $T = 77$K by cold traps filled with

liquid nitrogen (L-N_2). The sample space is located in the centre of the cryostat and is insulated from the main bath by an inner vacuum chamber (IVC) with an airlock system, which isolates the sample space from the environment and allows to insert the device into the centre of the magnet via the sample probe. The sample space is connected to the main bath via a needle valve, which can control the flow of helium. With the addition of a heater in the sample space, the temperature of the sample space can be controlled in the range $1.7\text{K} < T < 250\text{K}$ by using a LakeShore controller and the heater in the variable temperature inset (VTI). For the optical illumination, an optical fibre is connected at the end of the probe, which allows to transmit external light sources to the device inside the cryostat.

The resistive magnet at the EMFL (Grenoble) can generate magnetic fields B up to 30T in a 50 mm diameter bore with the homogeneity of 860×10^{-6} in 1 cm^3. A long probe is used to mount and insert the sample into a bath of liquid helium in the bore of the magnet. The magnet is cooled down by a closed loop of deionised and deoxygenated water with a flow rate of $\sim$1000 m^3/h. The magnet requires a maximum of 24 MW power to achieve 30T.

Figure 4.11 shows the block diagram of the experimental set up used to study InSe/graphene Hall bars using the superconducting magneto-cryostat. The devices were placed inside the cryostat in a variable temperature with pressure of about 10 mbar monitored by a 340 LakeShore temperature controller and a vacuum gauge. A Keithley 2400 was used as a constant direct current source for the source-drain current. The gate voltage V_g was applied by using a Keithley 2400 DC voltage source, which was also used to measure the gate leakage current (I_g) of the devices (Figure 4.11). Rear terminals (Term 2) of HP DC

voltmeters were used to study the longitudinal (V_{xx}) and Hall (V_{xy}) voltages of the devices. The magnetic field was applied perpendicular to the graphene layer and monitored by the power supply current. For the longitudinal voltage (V_{xx}) and Hall volatege (V_{xy}) measurements at a constant gate bias, the magnetic field was swept from -2T to +14T keeping V_g fixed, whereas for the gate dependent studies of the longitudinal voltage (V_{xx}) and Hall voltage (V_{xy}) measurements, the gate voltage was applied over a wide range (*e.g.* -100 V < V_g < +100 V) keeping the magnetic field constant (*e.g.* B=0, 5, 10, 14T). For the magneto-transport experiments under optical illumination, we used an unfocused He-Ne laser beam of wavelength λ = 632.8 nm, power, P, up to 13 mW/mm^2, and spot diameter d ~ 1 mm. The experimental data were acquired by using a computer running Labview program.

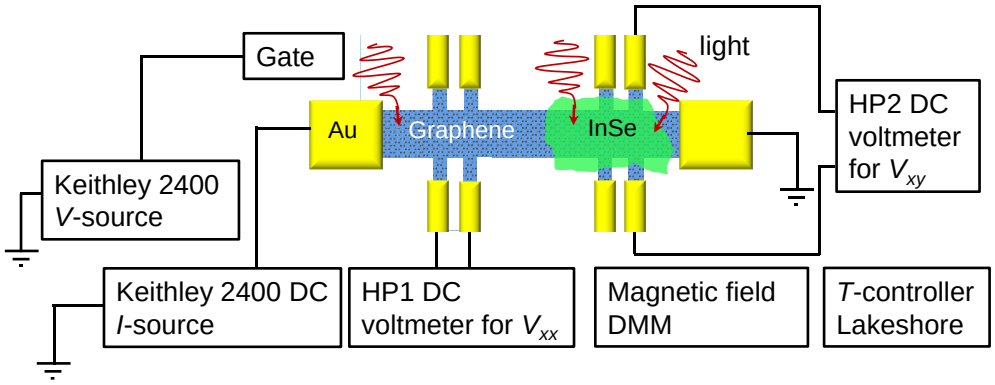

Figure 4.11 Block diagram of transport measurements using superconducting magneto-cryostat.

Chapter 5

Electron transport in InSe/graphene heterostructures

This chapter describes the magneto-transport properties of InSe/graphene heterostructure devices. We show that InSe can be employed in graphene-based FETs as an electrically active capping layer to "modulation-dope" graphene and enhance the carrier mobility of graphene grown by chemical vapour deposition (CVD). Also we report on a "giant quantum Hall plateau" effect in InSe-capped graphene. Results presented in this chapter were published in *Physical Review Letters*, **119**, 157701 (2017).

5.1 Introduction

A focus of low dimensional condensed matter physics is the search of quantum systems that can outperform conventional materials and devices. An example is graphene grown on silicon carbide in which the magnetic field-induced transfer of electrons between the two materials leads to a "giant" quantum Hall (QH) effect plateau.[164] This epitaxially-grown single layer graphene on SiC is a two-dimensional electron gas system that is likely to replace III-V compound heterostructures for the next generation QH resistance standards.[134,160-164] In this chapter we demonstrate that this quantum magnetoresistance phenomenon is not unique to graphene on SiC. In our field effect transistor, single layer graphene is capped by a layer of the van der Waals (vdW) crystal InSe. We use a gate electrode to control the charge transfer at the InSe/graphene vdW interface, which gives rise to an enhancement of the carrier mobility in the graphene layer and the appearance of a giant quantum Hall

plateau in the Hall resistance. We show that this arises from the close alignment of the conduction band edge of InSe with the Dirac point of graphene. This property enables the magnetic field and electric field effect-induced transfer of charge carriers between InSe and the adjacent graphene layer.

5.2 "Modulation doping" and field effect in InSe/graphene

To study the magneto-transport properties of InSe/graphene heterostructures, several samples were fabricated. In these structures only one half of the graphene 10-terminal Hall bar device was capped with an InSe flake and the rest of it remained uncapped. The schematic and optical image of a multi-terminal Hall-bar with distinct regions containing uncapped and InSe-capped graphene are shown in Figure 5.1. Whereas it is difficult to achieve gate voltage control of graphene on SiC, the design of our device on a conventional SiO_2/Si substrate, provides a means of controlling and studying charge transfer across the InSe-graphene interface by applying a gate voltage to the *n*-Si substrate.

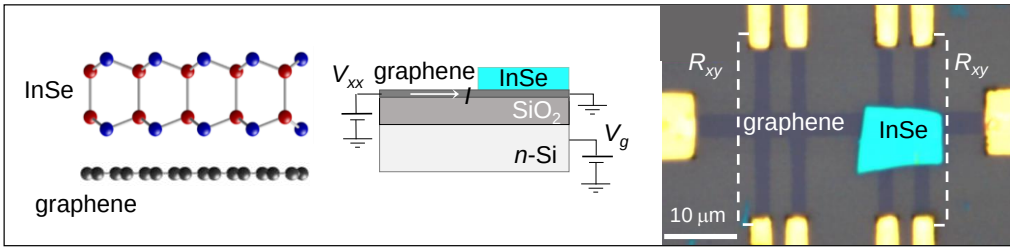

Figure 5.1 Left: Crystal structure of InSe and graphene along the axis perpendicular to the layer plane. Right: schematic and optical image of a multi-terminal Hall-bar containing uncapped and InSe-capped graphene.

Figure 5.2a shows the gate voltage dependence of the low temperature (T = 2K) magnetoresistance, R_{xx}, of the uncapped and InSe-capped graphene measured at B = 0 over a wide range of V_g from -60 V to 140 V. In both cases,

R_{xx} reaches a maximum at a large positive gate voltage, as expected for the *p*-type character of CVD graphene on SiO_2.[182] For InSe-capped graphene, the maximum of $R_{xx}(V_g)$ occurs at a lower gate voltage, shifted by ΔV_g = -15 V relative to the peak for the uncapped graphene layer. The maximum of $R_{xx}(V_g)$ corresponds to the alignment of the Fermi energy, E_F , with the Dirac point of graphene's band structure. For V_g values beyond this maximum, the sign of the Hall voltage is reversed, corresponding to *n*-type conduction.

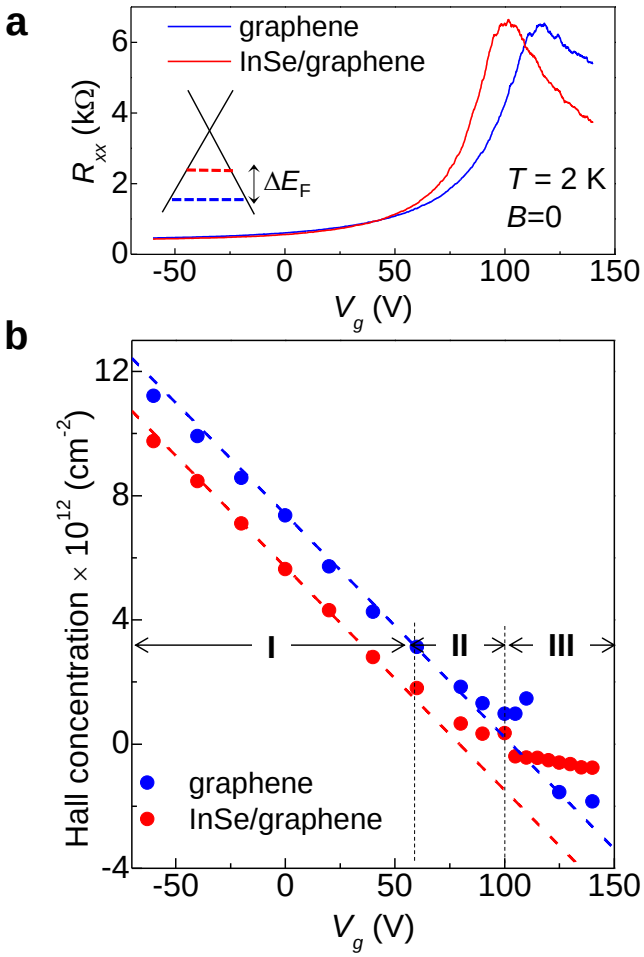

Figure 5.2 (a) Resistance R_{xx} of the graphene and InSe-capped graphene as a function of V_g at zero magnetic field and T = 2K. Inset: band diagram of graphene showing the upward shift, ΔE_F, of the Fermi level, E_F, following the capping of graphene by an InSe layer. (b) Hall carrier concentration in graphene and InSe/graphene Hall-bars as a function of gate voltage V_g at zero magnetic field and T = 2K. Regions I, II and III indicate different regimes of applied gate voltages. Blue and red lines correspond to the carrier density calculated from the capacitance equation (5.1) in the text.

We have measured the Hall resistance (R_{xy}) and magnetoresistance (R_{xx}) at low magnetic field and low temperature for different gate voltages. At low temperature (T = 2K), all measured R_{xy} vs B curves are linear in the low field region ($0 < B < 2$T) for each applied gate voltage, which is consistent with a single carrier type in a single band. These Hall voltage data at low magnetic field and low temperature (T = 2K) are used to plot the gate voltage dependence of the carrier density, n, for both the pristine graphene and the InSe-capped graphene layer (Figure 5.2b). Over the range of gate voltage from -60 V to +60 V, indicated as region I in Figure 5.2b, the measured hole carrier density in both the uncapped and InSe-capped graphene decreases linearly with the gate voltage in good agreement with the capacitance equation

$$n = C\Delta V_g/q + n_0. \tag{5.1}$$

Here n is the measured carrier sheet density, q = -e is the electron charge, $C = \varepsilon\varepsilon_0/t$ =115 μF/m^2 is the "classical" capacitance per unit area of the graphene/SiO_2/Si heterostructure, t = 300 nm is the SiO_2 layer thickness, $\varepsilon = 3.9$ is the relative dielectric constant of SiO_2, ε_0 is the permittivity of free space, and n_0 = 7.4x10^{12} cm^{-2} and 5.7x10^{12} cm^{-2} are the hole sheet densities at V_g = 0 for the uncapped and capped graphene, respectively. Thus the hole density for InSe-capped graphene, deduced from Hall measurements at V_g = 0, is significantly smaller (Δn = 1.7x10^{12} cm^{-2}) than for the uncapped control layer, indicating a "modulation doping" effect in which electrons are transferred from InSe to graphene. In contrast, over the range +60 V < V_g < +100 V (region II in Figure 5.2b), the Hall effect measurements show that the sheet density of the InSe-capped graphene deviates from the linear dependence on gate voltage in

equation (5.1), indicated by the dashed red line in Figure 5.2b. Furthermore, in region III (V_g > +100 V), the conduction changes from *p*- to *n*-type and the electron density becomes weakly dependent on V_g.

In order to understand the electron transfer process in our device, we consider the band alignment and electron transfer at the InSe/graphene interface taking into account the electron affinities and work functions of InSe and graphene. For simplicity, we assume that the effect of impurities and/or defects at the InSe/graphene interface is negligible. This assumption is reasonable, as the cleaved surface of InSe contains a low-density of surface states and the layers are functional both optically and electrically down to a few atomic layers.[17] Nevertheless, we do not exclude that a small density of defects may form during the device fabrication and that this may affect the charge transfer.

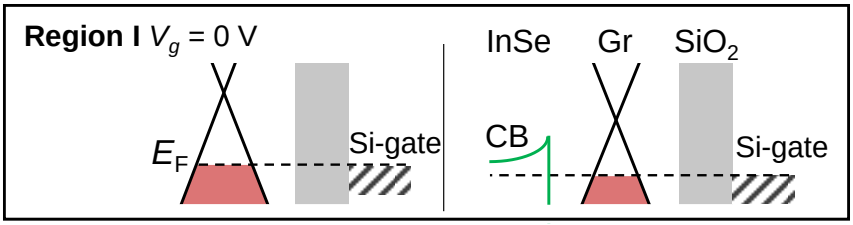

Figure 5.3 Energy band diagram of the graphene/SiO_2/Si and InSe/graphene/SiO_2/Si heterostructure at V_g = 0 V corresponding to region I. The red coloured regions indicate states filled with electrons. The green curve indicates the conduction band (CB) bending in the InSe layer.

The electron affinity of graphene (χ_{Gr} = 4.5 eV) is only slightly smaller than that of bulk InSe (χ_{InSe} = 4.6 eV).[29,183] These values of χ and the measured concentration of carriers in bulk InSe (electron density ~ 10^{15} cm^{-3}) and the uncapped graphene (hole density ~ $7x10^{12}$ cm^{-2}) indicate that at V_g = 0 the work function of our CVD graphene on SiO_2 ($\phi_{Gr} \approx$ 4.8 eV) is larger than that of the *n*-type InSe ($\phi_{InSe} \approx$ 4.7 eV). At V_g = 0, equilibrium is achieved by transfer of electrons from the *n*-InSe to graphene. This induces a depletion layer and an

upward bend of the InSe conduction band edge near its interface with graphene, shown schematically in Figure 5.3.

The charge transfer at the InSe/graphene interface is also proved optically. Figure 5.4 shows representative PL spectra of InSe flakes with different layer thickness. The PL spectra were acquired before (black lines) and after (red lines) the transfer of the flakes onto CVD-graphene. It can be seen that the PL intensity is always reduced after the transfer of the InSe nanosheets onto graphene, suggestive of a charge transfer at the InSe/graphene interface.

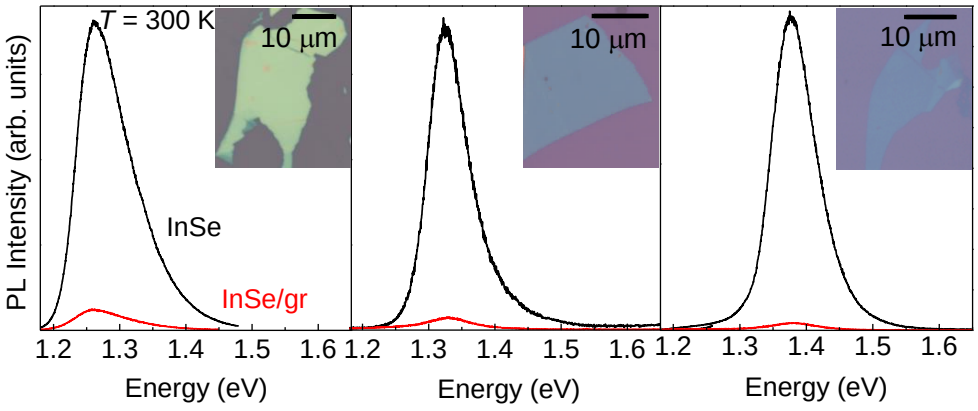

Figure 5.4 Representative PL spectra for InSe nanosheets on a polymer (black) and on CVD graphene (red) at T = 300K. The insets show optical images of the nanosheets on graphene. The nanosheets have thickness L from L > 20 nm (left) to ~ 10 nm (centre) and ~ 7 nm (right).

We use the equivalent circuit shown in Figure 5.5 (lower right inset) to model the electrostatics of the device, noting that the chemical potentials of the graphene and InSe layers remain aligned in the heterostructure at all applied gate voltages and magnetic fields because no bias voltage is applied between them. The total capacitance, C_t, of the InSe/graphene/SiO_2/Si heterostructure, is a series combination of the classical capacitance, C_c, of the SiO_2 and the InSe depletion layer, and the quantum capacitance, C_q, of graphene: $C_t^{-1} = C_c^{-1} + C_q^{-1}$. The quantum capacitance accounts for the non-classical dependence of

graphene's carrier density, *n*, on the applied gate voltage when the Fermi energy, E_F, is close to the low density of states at the Dirac point, *i.e.* $C_q = e^2(dn/dE_F) = 2e^2 E_F/\pi\hbar^2 v_F^2$. When the Fermi level is far from the Dirac point of the graphene's band structure (region I, Figure 5.3), the effect of the quantum capacitance becomes negligible, and the carrier density in graphene varies with V_g according to the simple capacitance equation (5.1), *i.e.* $qdn = C_c dV_g$, as observed experimentally in region I of Figure 5.2b. In contrast, when the positive gate voltage is sufficiently large so that the Fermi level approaches the Dirac point of graphene, the total capacitance is reduced due to the small quantum capacitance, leading to a weaker variation of the carrier density with V_g.

The slope of the measured $n(V_g)$ dependence for InSe-capped graphene changes twice between V_g = +60 V and +100 V (*i.e.* beginning and end of region II, Figure 5.2b). This behavior indicates a regime in which the upward bend of the InSe conduction band edge is reduced due to the positive space charge of ionized donors, and electrons start to fill donor states below the conduction band edge of the InSe layer (region II, Figure 5.5a). The change in the slope of $n(V_g)$ tends to saturate for V_g > +100 V (region III, Figure 5.2b). We attribute this to the movement of the Fermi level into the high density of states in the conduction band continuum of InSe, leading eventually to the formation of an electron accumulation layer at high positive V_g (region III, Figure 5.5). Since the density of states of graphene at energies close to the Dirac point is much lower than in the conduction band of the InSe layer, the chemical potential tends to remain pinned near the InSe conduction band edge.

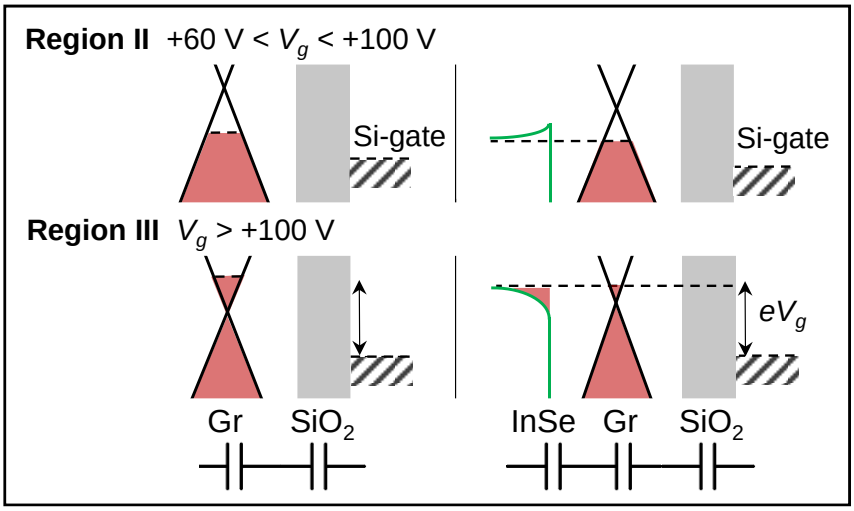

Figure 5.5 Energy band diagram of the graphene/SiO_2/Si and InSe/graphene/SiO_2/Si heterostructure at different applied gate biases corresponding to regions II (+60 V < V_g < +100 V) and III (V_g > 100 V) in Figure 5.2b. The red coloured regions indicate states filled with electrons. The green curves indicate the band bending in InSe. The bottom inset illustrates the capacitance contributions to the total capacitance of the heterostrucures.

The slope of the measured $n(V_g)$ dependence for InSe-capped graphene changes between V_g = +60 V and +100 V (region II, Figure 5.2b) and the Fermi energy E_F aligns with the Dirac point at $V_g \approx$ +100 V (Figure 5.2a). This behaviour suggests a regime in which electrons start to fill donor states below the CB edge of InSe at V_g = +60 V, which are close to the Dirac point at $V_g \approx$ +100 V. We use the $n(V_g)$ dependence to calculate the dependence of E_F on V_g. In Figure 5.6a data points are obtained using the measured values of $n(V_g)$ and equation (5.2):

$$E_F = v_F \hbar \sqrt{\pi n} \tag{5.2}$$

where $v_F = 10^6$ m/s is the Fermi velocity in graphene and E_F is measured relative to the Dirac point. The continuous curve is calculated using equation (5.2) and the $n(V_g)$ curve defined by equation (5.1). The data points in Figure 5.6a reveal

a change of E_F of $W \sim 0.15$ eV between $V_g = +60$ V and +100 V. Thus the donor level E_d is at an energy of 0.15 eV relative to the Dirac point (Figure 5.6b). Using the electron affinity of graphene and InSe (χ = 4.5 and 4.6 eV, respectively), we estimate that E_d is ~ 50 meV below the CB edge of InSe. This result is in qualitative agreement with results of optical studies on *n*-type InSe flakes.[97]

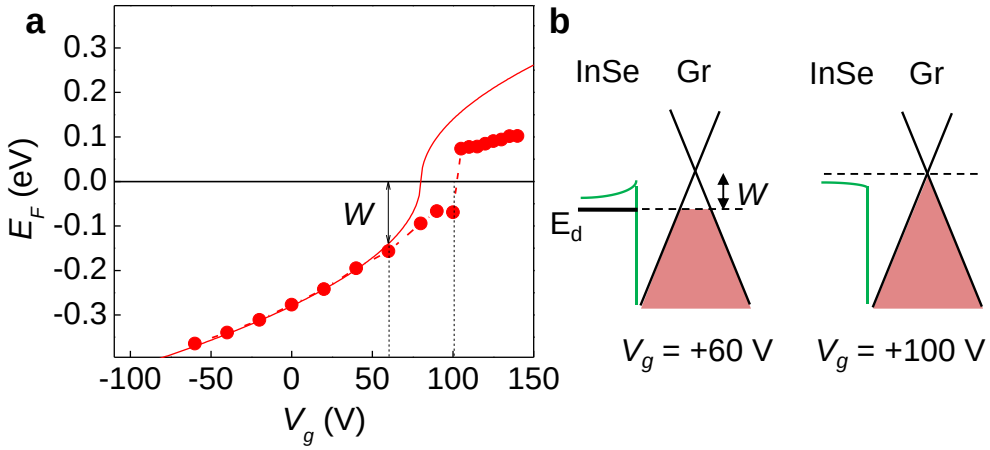

Figure 5.6 a) Fermi energy in InSe-capped graphene versus V_g. Data points are calculated using the measured Hall density and equation (5.2). The continuous curve is calculated using equation (5.2) and the $n(V_g)$ curve defined by equation (5.1). b) Schematic energy band diagram of InSe-capped graphene at V_g = +60 V and +100 V.

We now examine the effect of InSe on the mobility of graphene. The field effect mobility, μ_F, for graphene and InSe-capped graphene is calculated from

$$\mu_F = \frac{1}{e}\frac{\Delta\sigma/\Delta V}{\Delta n/\Delta V}, \tag{5.3}$$

where σ is the conductance, $\Delta\sigma/\Delta V$ is obtained from the linear fit of the $\sigma(V_g)$ curve (Figure 5.7) and $e\Delta n/\Delta V = C$.

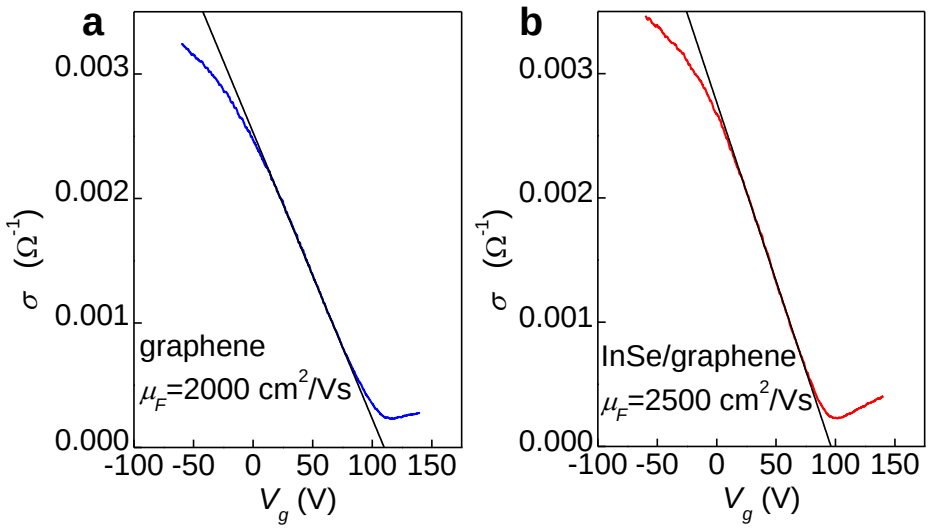

Figure 5.7 Linear fits of the conductance, σ, vs V_g for pristine graphene (a) and InSe/graphene (b) devices measured at B = 0, T = 2K, I = 0.2 μA (the same data as $R_{xx}(V_g)$ in Fig. 5.2a). The fits were used to estimate the field effect mobility for graphene and InSe/graphene: μ_F = 2000 cm^2/Vs and 2500 cm^2/Vs, respectively.

From the measured conductance σ at B = 0 and the Hall resistance R_{xy}, we obtain the Hall mobility, μ_H, using the relation $\mu_H = \sigma R_{xy}$, where R_{xy} is extracted for low B (-2T < B < 2T) at different V_g, $\sigma = f/R_{xx}(V_g)$ and f = 1.5 is the length-width ratio of the Hall bar. The gate voltage dependence of μ_H and the field effect mobility μ_F are shown in Figure 5.8. The data demonstrate that for region I (V_g < 60 V), the measured values of the field-effect mobility $\mu_F = \sigma/en$ and the Hall mobility $\mu_H = \sigma R_{xy}$ are in qualitative agreement with the classical capacitance model. The InSe capping layer enhances significantly the carrier mobility in the graphene layer at all gate voltages, with an enhancement factor by up to ~ 3 at voltages that are close to the V_g-position of the peak in $R_{xx}(V_g)$. For InSe-capped graphene, the Hall mobility μ_H is also significantly larger than the field effect mobility estimated using $\mu_F = \sigma/en$, where $n(V_g)$ is given by the capacitance equation (5.1).

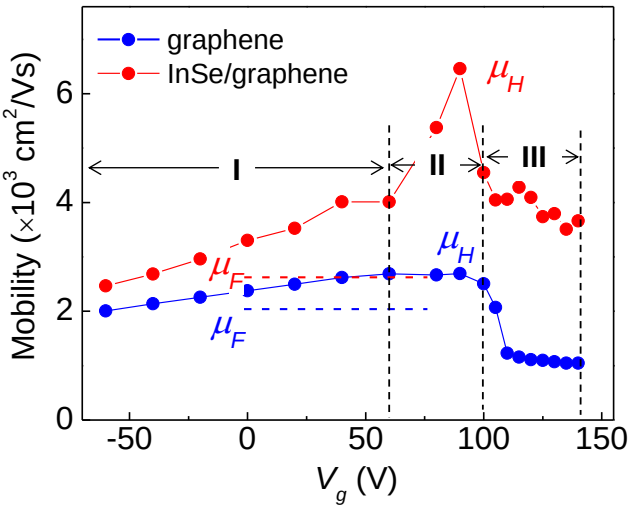

Figure 5.8 Hall mobility μ_H (dots) and field effect mobility μ_F (blue and red dashed lines) of uncapped and InSe-capped graphene Hall-bars at T = 2K. The Hall mobility μ_H is measured at different applied gate voltages V_g. The field effect mobility μ_F is estimated from a linear fit of the measured $R_{xx}(V_g)$ curve using the relation (5.3) in the V_g range shown in Figure 5.7. Continuous lines are guides to the eye.

The significant increase of carrier mobility in region II (Figure 5.8) can be explained by partial screening of the negatively charged (defect) acceptors at the SiO_2/graphene interface by positively charged donors in the InSe capping layer and by the dielectric screening due to the static dielectric constant of InSe ($\varepsilon_{InSe} \approx 10$).[92] In CVD graphene on SiO_2, the main mechanism limiting the carrier mobility is electron scattering by negatively charged acceptors. It has been described phenomenologically by the relation $\mu = \alpha \frac{N_0}{N}$, where N is the concentration of the charged acceptors, and N_0 and α are empirical parameters.[184] Our measured enhancement of mobility in the InSe-capped graphene layer indicates an electrostatic compensation of these charged acceptor impurities. This effect is analogous to that observed recently in *p*-type CVD graphene decorated with *n*-type quantum dots (QDs), where the largest increase of mobility is observed when the concentrations of donors in the QDs matches the concentration of impurities in graphene.[182]

5.3 Quantum Hall effect in InSe/graphene

The low temperature (T = 2K) Hall resistance, R_{xy}, and longitudinal magnetoresistance, R_{xx}, of the capped and uncapped graphene layers were measured up to magnetic fields B of 14T, applied perpendicular to the plane of the graphene layer and over a wide range of gate voltages V_g applied between the graphene and the Si substrate. As shown in Figure 5.9(a), the InSe-capped graphene layer reveals a broad, flat quantum Hall resistance plateau with R_{xy} = (12.9 ± 0.1) kΩ, which extends up to our maximum available magnetic field of 14T. This value is close to that of the resistance quantum, $h/2e^2$ = 12.906 kΩ, corresponding to a Landau level filling factor $\nu = 2$. In addition, at large positive gate voltage (*e.g.* V_g = +60 V, in Figure 5.9a), the $R_{xy}(B)$ curve exhibits a well-defined shoulder between 6 and 8T, with a resistance of around (4.3 ± 0.1) kΩ, close to the value $h/6e^2 = 4.302$ kΩ ($\nu = 6$). In stark contrast, for the uncapped section of graphene, the Hall resistance R_{xy} increases linearly with B up to 14 T. The $\nu = 2$ plateau persists up to a temperature of $T \sim 100$K (Figure 5.9b), though with a smaller value of R_{xy}. In the vicinity of the $\nu = 2$ plateau, the magnetoresistance $R_{xx}(B)$ approaches zero (Figure 5.9c).

The extended quantum Hall plateau with $\nu = 2$ observed in the InSe/graphene heterostructure (Figure 5.9a) is similar in form to the "giant QH plateau" reported for graphene grown epitaxially by the thermal decomposition of the surface layer of SiC.[134,160-164] Because graphene on SiC can maintain a quantum Hall state up to higher critical current densities and higher temperatures than GaAs-based heterostructures at comparable magnetic fields, it is regarded as an ideal candidate for the next generation of quantum Hall resistance standards.[161,164]

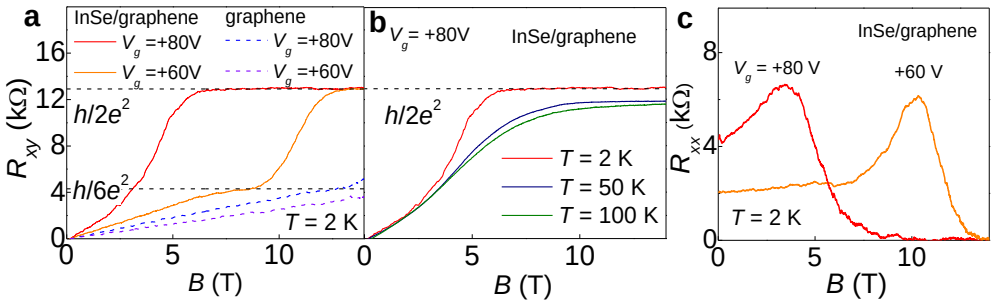

Figure 5.9 (a) Hall resistance, R_{xy}, for InSe/graphene and graphene versus magnetic field, B, for different gate voltages, V_g, at temperature T = 2K. (b) Hall resistance R_{xy}, for InSe/graphene section of the Hall-bar versus B at different temperatures T (V_g = +80 V and current I = 0.2 mA). (c) Magnetoresistance, R_{xx}, for InSe/graphene versus B for different V_g at T = 2K.

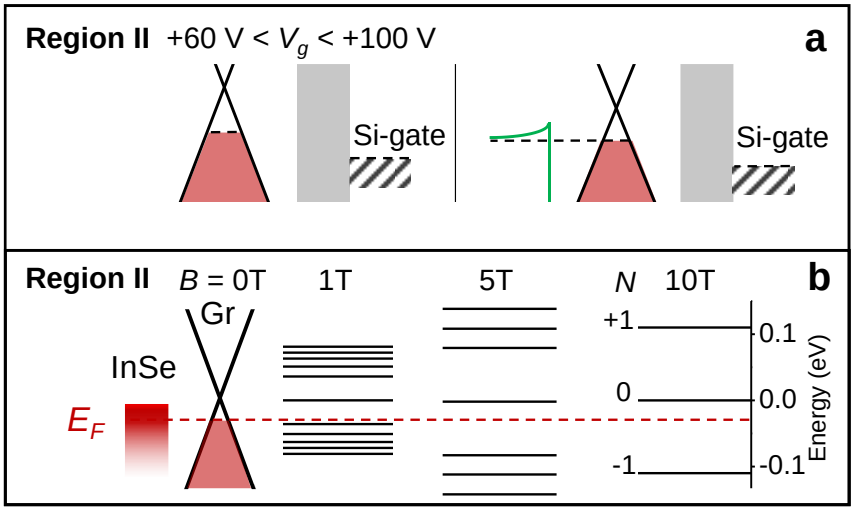

Figure 5.10 (a) Energy band diagram of the graphene/SiO_2/Si and InSe/graphene/SiO_2/Si heterostructure at applied gate biases +60 V < V_g < +100 V corresponding to regions II. The red coloured regions indicate states filled with electrons. The green curves indicate the band bending in InSe. (b) Landau levels (LLs) of graphene at B = 0, 1, 5 and 10T (region II). For InSe-capped graphene, the Fermi level is pinned between the N = 0 and N = -1 LLs over a wide range of B.

The remarkable "giant" ν = 2 QH plateau in graphene on SiC is also very useful for metrology as discussed in section 3.1.1 and has been explained in terms of the transfer of electrons from the underlying SiC substrate to the graphene layer, resulting in the pinning of the Fermi level (E_F) so that the Landau level at the Dirac point remains completely filled when its degeneracy,

$2eB/h$, increases with increasing B.[159,164] The favourable band alignment between InSe and graphene is an important factor that enables effective modulation doping of graphene over a wide range of gate biases. The appearance of the extended $\nu = 2$ quantum Hall plateau relies on this charge transfer and on the "pinning" of the chemical potential in the energy gap between the $N = 0$ and $N = -1$ Landau levels when their degeneracy increases with increasing B (Figure 5.10b).

As seen in Figure 5.9b, the $\nu = 2$ plateau persists up to a temperature of $T \sim 100$K, though with a smaller value of R_{xy}, which decreases with increasing temperature. We attribute this decrease to thermally-activated parallel conduction along the InSe capping layer. To examine the parallel conduction along the InSe layer, we model the Hall resistance R_{xy} in the high field and quantum limit as[185]:

$$R_{xy} = \frac{B}{en_{th}+2Be^2/h}. \tag{5.4}$$

where, n_{th} represents the thermally activated electron density in the InSe layer.

As shown in Figure 5.11a, at $T = 2$K, the quantized value of $R_{xy} = h/2e^2$ indicates that parallel conduction can be neglected at this temperature. However, with increasing T, R_{xy} decreases below its quantized value, thus indicating a thermally activated increase of the carrier density (n_{th}) and current leaking into the InSe layer. From the measured values of R_{xy} at various T, we find that n_{th} increases from about 10^9 cm^{-2} at 2K to a saturation value of $\sim 10^{11}$ cm^{-2} for T above 100K (Figure 5.11b); correspondingly the Hall resistance associated with the InSe layer decreases from ~ 90 MΩ to 90 kΩ. This behaviour was observed in different samples.

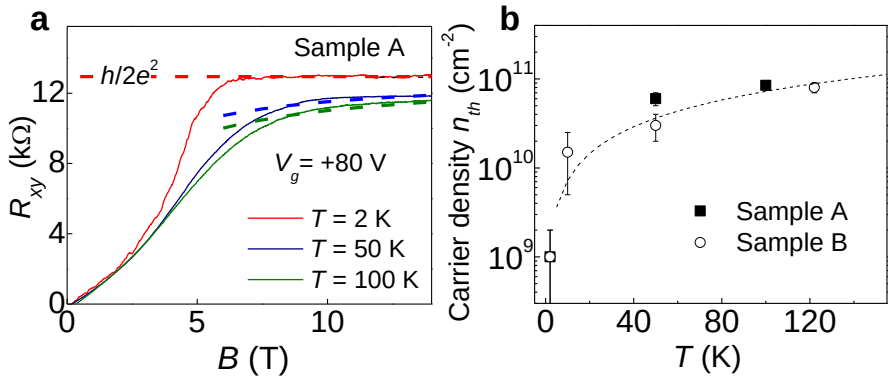

Figure 5.11 a) Hall resistance, R_{xy}, for the InSe/graphene section of the Hall-bar versus B for different T at V_g = +80 V and I = 0.2 mA. The dashed lines correspond to the Hall resistance calculated taking into account the parallel conduction along the InSe layer, as described by equation (5.4). b) Thermally activated carrier density in the InSe layer versus T, as derived from a fit to the measured values of R_{xy} to equation (5.4) for two samples (A and B).

5.4 Summary

We demonstrate that InSe can be employed in graphene-based FETs as an electrically active capping layer to "modulation-dope" single layer graphene, thus leading to a "giant" quantum Hall effect plateau and an enhancement of the carrier mobility in graphene. Low temperature measurements of the magnetoresistance of this InSe-capped graphene FET reveal the presence of a well-defined quantum Hall plateau at a filling factor $\nu = 2$ in the magnetic field-dependent Hall resistance, R_{xy}. The plateau extends over a wide range of magnetic field, B, from 6T to a maximum available field of 14T. Our measurements demonstrate that this quantum magnetoresistance phenomenon is not unique to epitaxially-grown graphene on SiC.[134,160-164] We show that the close alignment of the conduction band edge of InSe with the Dirac point of graphene enables the magnetic field and electric field effect-induced transfer of charge carriers between InSe and the degenerate Landau level states of the adjacent graphene layer, which is coupled by a van der Waals hetero-interface to the InSe.

Chapter 6

Photosensing with InSe/graphene heterostructures

This chapter describes the electronic properties of graphene capped with InSe and how these can be controlled by a combination of optical excitation and electrostatic gating. The light-induced transfer of charge between InSe and graphene offers an effective method to increase or decrease the carrier density in graphene. The effective charge transfer can induce a reversal of the sign of the Hall voltage and of the $h/2e^2$ quantum Hall (QH) plateau, which is observed over a wide range of applied magnetic fields and temperatures. The results presented in this chapter has been published in *Advanced Functional Materials,* **29**, 1805491 (2019).

6.1 Gate-tunable graphene transistors photosensitized with InSe

Figure 6.1a shows an optical image of one of our InSe/graphene heterostructure devices. The InSe layer forms a cap over one half of the graphene Hall bar. The two sections of the device comprising uncapped and InSe-capped graphene are in a "series" resistance configuration with the same electrical current, *I*, flowing through both of them (Figure 6.1b). Magneto-transport experiments were performed in two modes: (i) in darkness and (ii) with the device uniformly illuminated by an unfocused He-Ne laser beam with a photon energy, $h\nu$ = 1.96 eV, in excess of the band gap energy of bulk InSe, E_g = 1.26 eV at 300K. Figure 6.1c and 6.1d show the V_g-dependence of the low (T = 2K) and room temperature (T = 300K) resistance, R_{xx}, of the uncapped and

InSe-capped graphene measured at zero magnetic field in darkness (black dashed curves) and under light illumination (red curves).

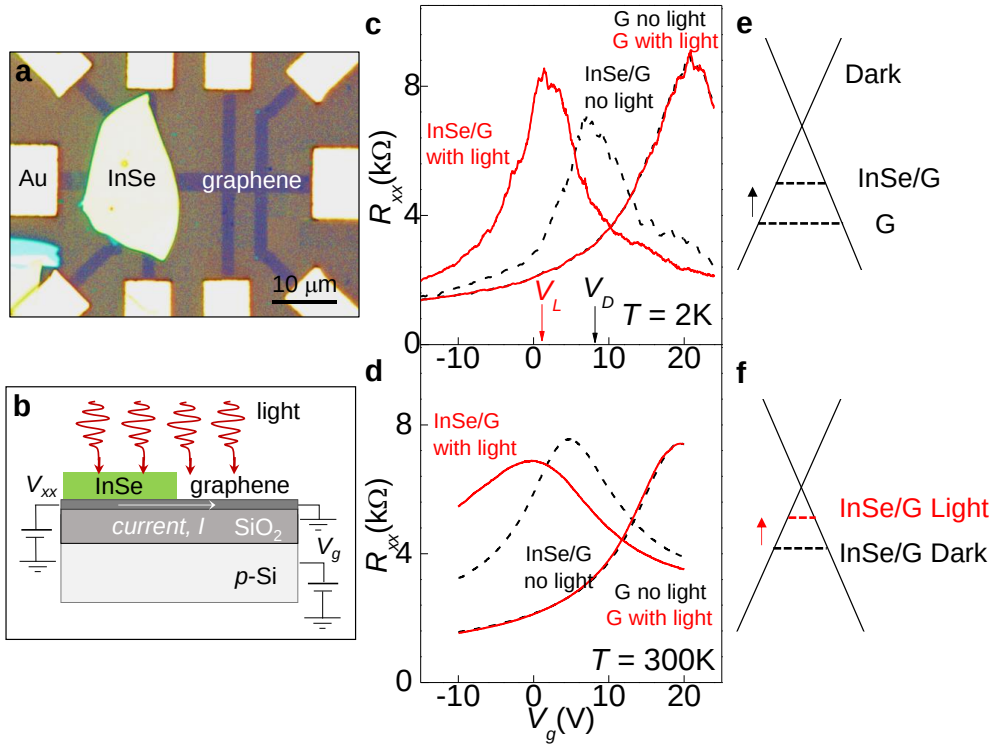

Figure 6.1 (a) Optical image and (b) sketch of a Hall bar containing uncapped and InSe-capped graphene. The thickness of the InSe layer is 50 nm, as measured by Atomic Force Microscopy. Devices with different layer thickness down to ~ 10 nm show a similar behaviour. (c-d) Resistance R_{xx} versus gate bias V_g (B = 0T and I = 0.5 μA) without (black dashed curves) and with illumination (red curves; λ = 633 nm and P = 9 mW/mm^2) for uncapped graphene (G) and InSe-capped graphene (InSe/G) at (c) T = 2K and (d) T = 300K. V_L and V_D denote the peak position of the $R_{xx}(V_g)$ curves under illumination and in darkness, respectively. (e) Band diagram of graphene showing the upward shift of the Fermi level, E_F, following the capping of graphene by an InSe layer in the dark (e) and under illumination (f).

For uncapped graphene, R_{xx} reaches a maximum at a positive gate voltage, V_g = +21 V at T = 2K. Using the capacitance equation $n = -CV_g/q$ introduced in section 2.1.1, we deduce that the graphene is p-doped at V_g = 0 V with a hole density, $n = 1.6\times10^{12}$ cm^{-2}. In the capacitance equation q = - e is the electron charge, $C = \varepsilon\varepsilon_0/t = 121$ μF/m^2 is the "classical" capacitance per unit area of the graphene/SiO_2/Si heterostructure, t = 285 nm is the SiO_2 layer

thickness, $\varepsilon = 3.9$ is the relative dielectric constant of SiO_2, ε_0 is the permittivity of free space, and V_g is the voltage position of the peak in $R_{xx}(V_g)$. For InSe-capped graphene, the maximum of $R_{xx}(V_g)$ occurs at V_g = +7 V, shifted by ΔV_g ≈ -14 V relative to the peak for uncapped graphene, corresponding to a reduced hole density and shifts in Fermi level $\Delta E_F \approx +0.12$ eV (Figure 6.1e). The $R_{xx}(V_g)$ curve for the graphene-only section of the Hall bar does not change when its surface is illuminated with laser light. In contrast, for InSe-capped graphene, the maximum of $R_{xx}(V_g)$ shifts towards lower gate voltages at both T = 2K and 300K (red curves in Figures 6.1c and d). The corresponding shift in the Fermi level is $\Delta E_F \approx +0.078$ eV at T = 2K (Figure 6.1f).

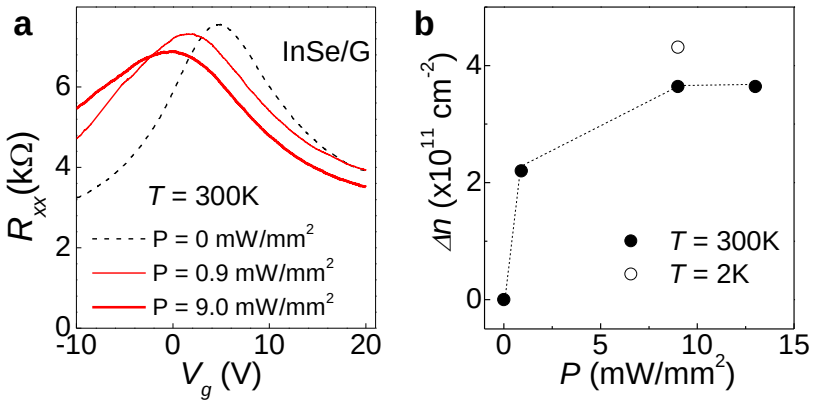

Figure 6.2 (a) Resistance R_{xx} of InSe-capped graphene versus V_g (I = 0.5μA) under illumination (P = 0, 0.9, 9.0 mW/mm^2; λ = 633 nm) at B = 0T and T = 300K. (b) Change in the electron density after light illumination as derived from the voltage shift of the $R_{xx}(V_g)$ curve and the capacitance equation described in the text.

The maximum of $R_{xx}(V_g)$ shifts steadily towards lower bias with increasing light intensity (Fig 6.2a). The shift to lower bias, ΔV_g, is proportional to the light intensity at low levels, but tends to saturate at $\Delta V_g \approx$ - 6 V for a light intensity $P >$ 10 mW/mm^2. The shift in V_g, ΔV_g, corresponds to an increase in the electron density by up to $\Delta n = 4.5\text{x}10^{11}$ cm^{-2} at $V_g = 0$ V, as derived from

the capacitance equation $\Delta n = C\Delta V_g/q$. Figure 6.2b shows these estimated values of Δn at different laser powers.

The photosensitivity of the InSe-capped graphene section of the device is illustrated in more detail in Figure 6.3a and 6.3b, which show the V_g-dependence of the light-induced change of R_{xx}, *i.e.* $\Delta R_{xx} = R_{xx}$(light) - R_{xx}(dark), at T = 2K and T = 300K, respectively. ΔR_{xx} has a maximum at a gate voltage $V_L \sim 0$ V, passes through zero at a gate voltage $V_F \sim +6$ V and changes sign with a minimum at $V_D \sim +10$ V. The values of V_D and V_L in Figure 6.3a correspond approximately to the peak positions of the $R_{xx}(V_g)$ curves in darkness and under illumination, respectively (Figure 6.1c). At the peak of $R_{xx}(V_g)$ the Fermi energy, E_F, aligns with the neutrality point of the graphene's band structure in darkness ($V_D \sim +10$ V) and under illumination ($V_L \sim 0$ V). Thus R_{xx} is either increased or decreased by light depending on the applied gate voltage and/or light intensity. The dependence of ΔR_{xx} on V_g is weakly affected by temperature, revealing similar features at both T = 2K and 300K (Figure 6.3a and b).

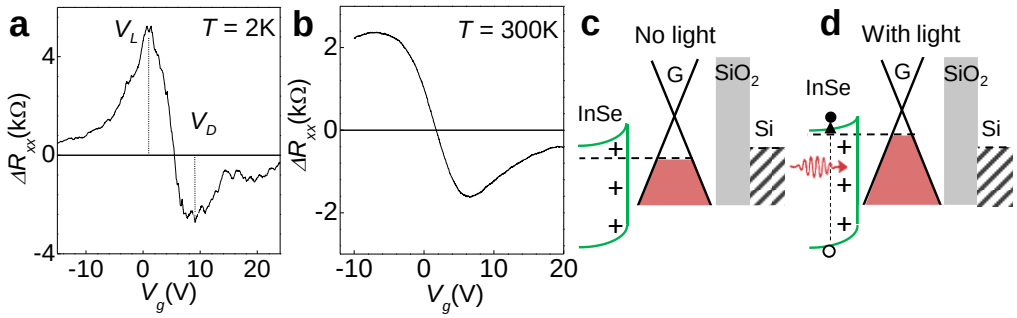

Figure 6.3 Dependence on the gate voltage V_g of the change in the resistance, ΔR_{xx}, of the InSe-capped section of the graphene Hall bar after illumination at (a) T = 2K and (b) T = 300K. Band diagram for the InSe/graphene/SiO_2/Si heterostructure in (c) darkness and (d) under illumination at V_g = 0.

The data in Figure 6.1 show that in darkness the capping of graphene with InSe increases significantly the electron density in the graphene layer. The

dopants responsible for the donor states in our nominally undoped InSe originate from In-interstitials in the crystal.[186] Under illumination, electrons photogenerated in InSe neutralize the positively charged donors in the InSe depletion layer and reduce the upward bending of the InSe conduction band edge near its interface with graphene (see Figure 6.3c and d). Thus the density of electrons in InSe-capped graphene increases under illumination.

6.2 Landau level quantization and quantum Hall plateau

The effects of light on the Hall resistance, R_{xy}, and its dependence on V_g are shown in Figure 6.4a for various magnetic fields, B, and T = 2K. For gate voltages in the range $V_L < V_g < V_D$ (see shaded areas), the optical excitation induces a sign reversal of the Hall voltage and of the QH plateau, $R_{xy} = h/\nu e^2$, where $\nu = 2$ is the graphene Landau level (LL) filling factor. Thus illumination induces a transition from a hole- to an electron-carrier current in the graphene layer over an extended range of gate voltages (Figure 6.4b).

We probe the distribution of charge in the graphene and InSe layers in the dark and under illumination by analysis of the magnetoresistance $R_{xx}(V_g)$ (Figure 6.5a-b). At low temperature (T = 2K) and in the presence of a quantizing magnetic field, both in darkness (left panel, Figure 6.5a) and under illumination (right panel, Figure 6.5a), the plots of $R_{xx}(V_g)$ display a pair of minima over a range of gate voltages corresponding to a quantized value $R_{xy} = h/2e^2$. Furthermore, under illumination, the minima in R_{xx} and the corresponding width of the QH plateaux in R_{xy} become asymmetric, and the QH plateau at $V_g > 0$ V becomes almost twice as wide as in darkness (Figure 6.5b).

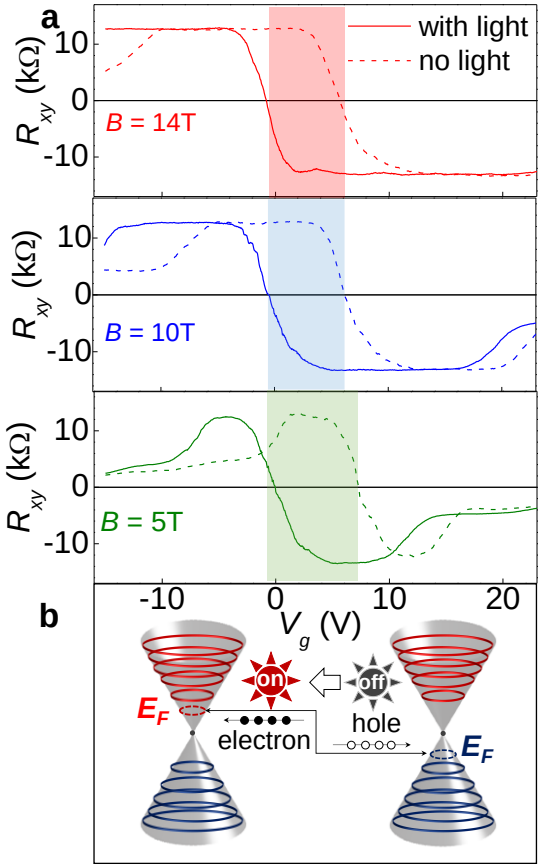

Figure 6.4 (a) Hall resistance, R_{xy}, of InSe-capped graphene versus gate voltage, V_g, in darkness (dashed line) and under illumination (continuous line) at T = 2K and B = 5, 10 and 14T (I = 0.5 μA, λ = 633 nm and P = 9 mW/mm^2). The shaded areas identify a range of gate voltages for which light reverses the sign of R_{xy}. (b) Landau level quantization in graphene and sketch of the movement of the Fermi level from the lower to the upper part of the Dirac cone under illumination, leading to the sign reversal of R_{xy} shown in part (a).

For single layer graphene, the energy-level spectrum of Dirac fermions in a magnetic field is described by the relation $E_N = sgn(N)\sqrt{e\hbar v_F^2 B|N|/\pi}$, where $v_F \sim 10^6$ m/s is the Fermi velocity in graphene and $N = 0, \pm1, \pm2 \ldots$ The spectrum comprises electron ($N \geq 1$) and hole ($N \leq -1$) LLs, as well as a LL ($N = 0$) at the neutrality point (inset of Figure 6.5).[140-143] Since the LLs for electrons and holes are symmetrically arranged around the $N = 0$ state, one might expect an approximately symmetric V_g-dependence of R_{xx} and R_{xy} relative to the voltage position of the peak in $R_{xx}(V_g)$. For graphene or InSe-capped graphene

in darkness, the minima in R_{xx} and the corresponding width of the QH plateaux in R_{xy} at the LL filling factor $\nu = 2$ are indeed symmetric. However, for InSe-capped graphene under illumination, both peaks and plateaux become asymmetric (Figure 6.5b).

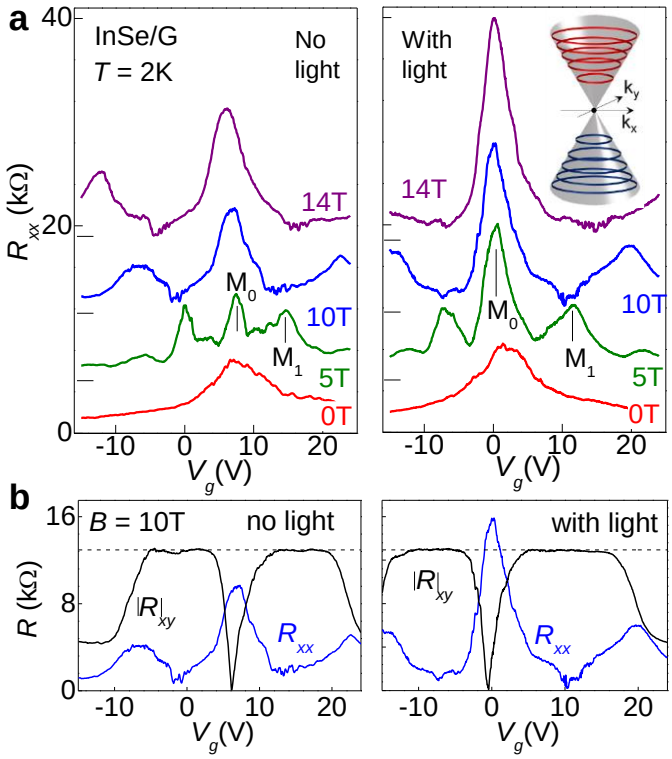

Figure 6.5 (a) Resistance, R_{xx}, of InSe-capped graphene versus gate voltage, V_g, at various magnetic fields B in darkness (left) and under illumination (right) (T = 2K, λ = 633 nm, P = 9 mW/mm^2). For clarity, curves at different B are displaced along the vertical axis. M_0 and M_1 label two maxima in $R_{xx}(V_g)$ corresponding to the alignment of the Fermi level with the N = 0 and N = +1 Landau levels (LLs). Inset: LL quantization in graphene. (b) R_{xx} and modulus of the Hall resistance, $|R_{xy}|$ versus V_g in darkness (left) and under illumination (right) at B = 10T. Dashed lines show $R_{xy} = h/2e^2$.

For the case of uncapped graphene and InSe-capped graphene in darkness, we use a simple capacitance equation, *i.e.* $C = e[dn_G/dV_g]$, to calculate the voltage separation ΔV_g of the maxima in the $R_{xx}(V_g)$ curve at different B. Here $C = \varepsilon\varepsilon_0/t$ is the "classical" capacitance per unit area of the graphene/SiO_2/Si heterostructure, e is the elementary charge, t = 285 nm is the

SiO_2 layer thickness, ε =3.9 is the relative dielectric constant of SiO_2, ε_0 is the permittivity of free space, and n_G is the carrier density in graphene. Over the range of V_g between the maxima M_0 and M_1 in $R_{xx}(V_g)$ (Figure 6.5a), corresponding respectively to the alignment of the Fermi level with the $N = 0$ and $N = +1$ LLs, $\Delta V_g = eg/C$, where $g = 4eB/h$ is the LL degeneracy.[143] This simple model reproduces quite accurately the data for the uncapped graphene in darkness and under illumination at different values of B and also for InSe-capped graphene in darkness (Figure 6.6a, black dots and star). However, it does not reproduce the values of ΔV_g in InSe-capped graphene under illumination (Figure 6.6a, open circles). To explain this behaviour, we note that when the positive gate voltage or the intensity of light are sufficiently large so that the Fermi level approaches the InSe CB edge, electrons start to fill donor states below the CB edge. In this case the carrier density induced by V_g has two contributions, one from the InSe layer (n_{InSe}) and one from graphene (n_{G}).

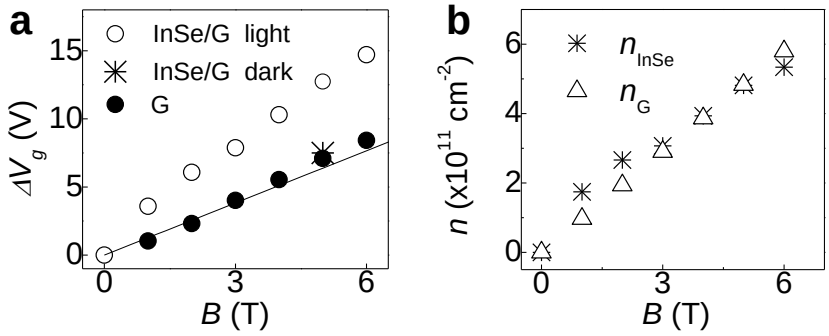

Figure 6.6 (a) B-dependence of the separation, ΔV_g, between peaks in $R_{xx}(V_g)$, M_0 and M_1, for graphene (G) and InSe-capped graphene (InSe/G) in darkness and under illumination (T = 2K). The line is the calculated dependence for graphene according to the model described in the text. (b) Density of carriers in graphene (n_G) and in InSe (n_{InSe}) versus B for InSe-capped graphene.

From the measured value of ΔV_g, corresponding to the separation of the peaks M_0 and M_1 peaks in R_{xx}, we estimate n_{InSe}, *i.e.* $en_{\mathrm{InSe}} = C\Delta V_g - en_{\mathrm{G}}$,

where $n_G = 4eB/h$ and $C = \varepsilon\varepsilon_0/t$. The values of n_{InSe} are plotted in Figure 6.6b for different B: n_{InSe} increases with B from zero at B = 0T and $V_g \approx 0$ V to 6x10^{11} cm^{-2} at B = 6T and $V_g \approx 15$ V. These values are comparable to the electron density in the $N = +1$ LL of the graphene layer, $n_G = 4eB/h$, also shown in Figure 6.6b. The increase of n_{InSe} with B corresponds to an increase of n_{InSe} with the Fermi energy, *i.e.* from the Dirac point at $N = 0$ at $E_0 = 0$ to the $N = +1$ LL at $E_1 = \sqrt{e\hbar v_F^2 B/\pi}$. Thus, at low temperatures, a significant fraction of electrons become bound on the relatively large density of donors (~10^{11} cm^{-2}) in the InSe capping layer. These donor states are likely to extend over a broad energy range: we estimate that $E_1 - E_0$ ~ 60 meV at B = 10T. The binding energy of isolated donors in bulk InSe is E_d ~ 30 meV.[97] However, for thin InSe, E_d depends on the position of the donors relative to the surface; furthermore, closely spaced donors can have larger binding energies. At low temperatures (T < 100K) the electrons in InSe remain bound to donors so that the QH voltage of the graphene layer is not "short-circuited" by the parallel conduction in the InSe layer.

The larger negative charge in the InSe-capped graphene with increasing positive gate voltage and/or increasing light intensity causes an asymmetric distribution of LL-features and QH plateaus relative to the peak in $R_{xx}(V_g)$ (Figure 6.5b). In particular, over a range of gate biases the QH plateau extend to high B. For example, at V_g = 7.5 V and V_g = - 6.0 V, the QH plateau is observed from B ~ 5T to 14T at T = 2K, corresponding to an increase in sheet density of ~ 5x10^{11} cm^{-2} (Figure 6.7a), and persists over a wide range of temperatures (Figure 6.7b).

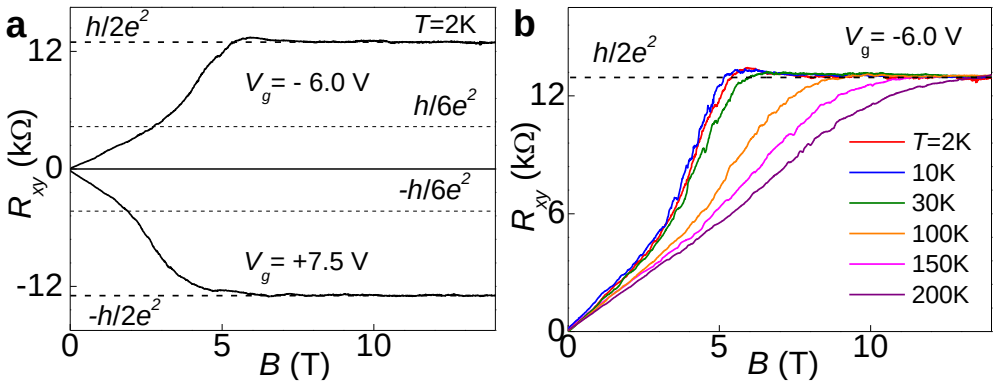

Figure 6.7 (a) Hall resistance, R_{xy}, of InSe-capped graphene versus magnetic field B at T = 2K and different gate voltages V_g under illumination (I = 0.5 μA, λ = 633 nm and P = 9 mW/mm^2). (b) Hall resistance R_{xy} of InSe-capped graphene versus B under illumination at different temperatures, T, and V_g = -6.0 V (I = 0.5 μA, λ = 633 nm and P = 9 mW/mm^2).

We have observed this behaviour for several devices although the QH resistance plateau occurs for a range of gate voltages that vary slightly from sample to sample. For example, the QH plateau at a filling factor ν = 2 in the magnetic field-dependent Hall resistance, R_{xy}, of InSe-capped CVD graphene extends up to the highest available magnetic field, *i.e.* B = 25T, at T = 2K for V_g = +22 V (Figure 6.8a). A similar extended QH plateau at a filling factor ν =2 is also observed in InSe-capped exfoliated graphene on an hBN/SiO_2/Si substrate (Figure 6.8b).

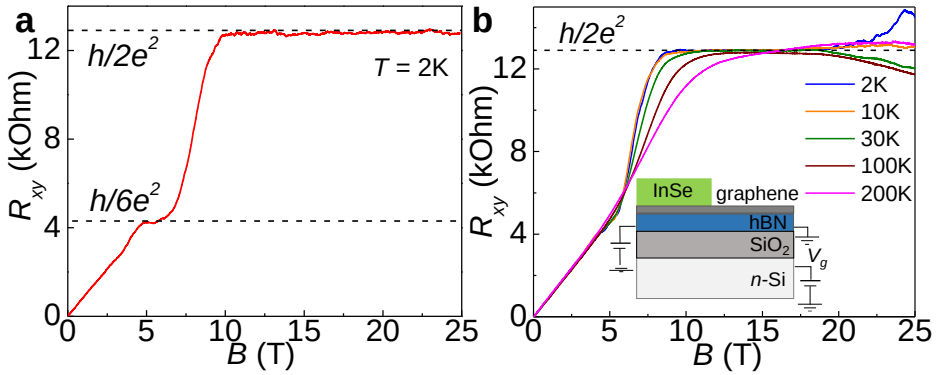

Figure 6.8 Hall resistance R_{xy} versus magnetic field B of InSe-capped (a) CVD graphene in the dark at V_g = +22 V (I = 0.5 μA) and T = 2K and (b) exfoliated graphene in the dark at different temperatures and V_g = +8.0 V (I = 0.5 μA). Inset in (b) shows the schematic representation of the InSe/exfoliated graphene on an hBN/SiO_2/Si substrate.

The appearance of the extended $\nu = 2$ QH plateau relies on the "pinning" of the chemical potential in the energy gap between Landau levels when their degeneracy increases with increasing *B*. The extended QH plateau reported here is similar in form to that for graphene grown epitaxially by the thermal decomposition of the surface layer of SiC.[134,160,162-164] This phenomenon can be explained in terms of the transfer of charge carriers, between the graphene layer and defects in the adjacent SiC substrate[164] or between graphene and its InSe capping layer, as discussed in chapter 5. Thus the $N = 0$ Landau level at the Dirac point of the graphene layer remains completely filled when its degeneracy increases with increasing *B* (Figure 6.9). Our data illustrate that this effect can be controlled by both the gate voltage and optical illumination.

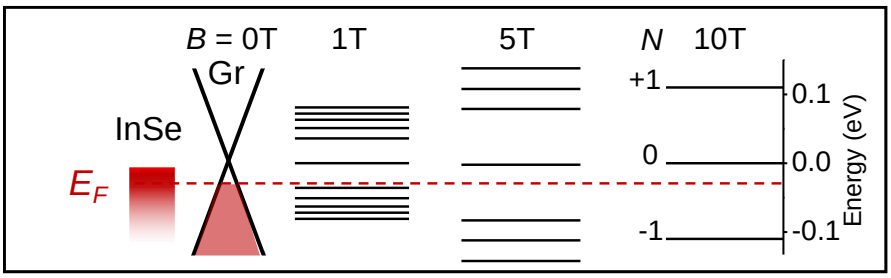

Figure 6.9 Landau levels (LLs) of graphene at *B* = 0, 1, 5 and 10T. For InSe-capped graphene, the Fermi level is pinned between the *N* = 0 and *N* = -1 LLs over a wide range of *B*.

We note that quantum Hall plateaux have been reported in exfoliated graphene at high magnetic fields $B \sim 20$T.[187] Also, a robust QH plateau has been reported in CVD graphene on SiC at lower $B = 2.5$T and $T = 1.3$K.[163] This plateau persists up to $T = 100$K and $B = 14$T. In our InSe capped graphene device, the $\nu = 2$ plateau can be seen up to $T \sim 200$K at $B = 14$T, although it becomes weaker with increasing temperature (Figure 6.7b). We assign the quenching of the QH plateau at higher *T* in an InSe-capped graphene to the thermal ionization of electrons out of the donor states into the conduction band

of the InSe capping layer, leading to current leaking onto the InSe layer. Using the measured values of R_{xy} at various T and the parallel conduction model for the Hall resistance R_{xy} in the high field and quantum limit[185]:

$$R_{xy} = \frac{B}{en_{th}+2Be^2/h}, \tag{6.1}$$

we find that the electron density in the conduction band of InSe, n_{th}, increases with increasing T. In particular, at B = 12T it increases from zero at 2K to ~ 10^{10} cm^{-2} at T ~ 200K (Figure 6.10).

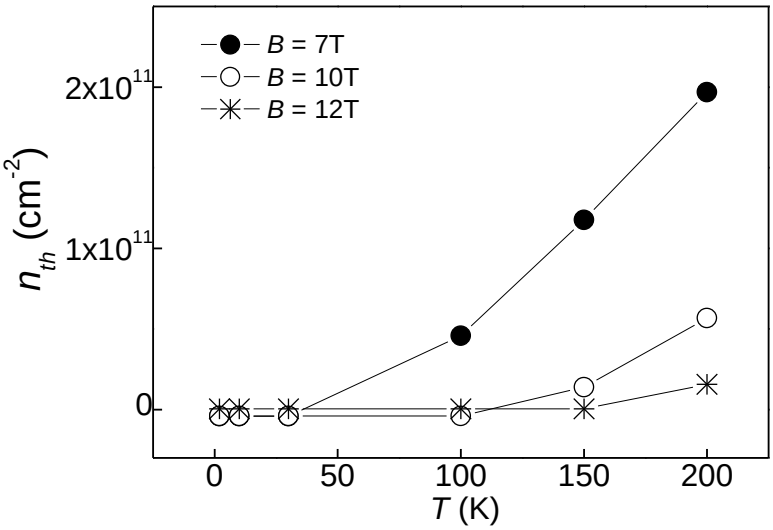

Figure 6.10 Thermally activated carrier density in the conduction band of InSe versus T, as derived from a fit to the measured values of R_{xy} to equation (6.1) at different applied magnetic fields B.

6.3 Summary

We demonstrated novel hybrid InSe/graphene phototransistors where the electronic properties of the graphene layer can be controlled by a combination of optical excitation and electrostatic gating. The optical illumination of the device create carriers in the high photosensitive InSe layer. The photo generated carriers are transferred across the InSe/graphene interface onto the graphene. This light induced charge transfer offers an effective method

to increase or decrease selectively the carrier density in the InSe-capped graphene, causing a change in the resistance that is gate-controllable and weakly dependent on temperature. A light-induced transition from a hole- to an electron-carrier current is also achieved over an extended range of gate voltages. In particular, the $\nu = 2$ quantum Hall plateau extends over a wide range of applied magnetic fields and temperatures. We estimate the carrier density of InSe-capped graphene under illumination and reveal the presence of a high density of donor states (~10^{11} cm^{-2}) in InSe. The combination of the high photosensitivity of InSe and unique electrical conductivity of graphene offer prospects for potential applications in quantum metrology and high-photosensitive optoelectronic devices.

Chapter 7

Transition metals in InSe

This chapter describes a new hybrid material system, which comprises the InSe semiconductor van der Waals crystal and ferromagnetic Fe-islands. This system exhibits ferromagnetic resonances and a large uniaxial magnetic anisotropy at room temperature, and simultaneously possesses semiconducting properties, thus offering opportunities for the development of functional devices that integrate magnetic and semiconducting properties within the same material system. Different transition metals in InSe are also discussed briefly at the end of the chapter. The results presented in this chapter were published in *Advanced Science*, **5**, 1800257 (2018).

7.1 Introduction

Magnetic anisotropy is at the heart of spintronics: it gives rise to a magnetic anisotropy energy (MAE) barrier between two opposite spin directions and hence to the possibility to store and process information.[188] Magnetic anisotropy has been demonstrated in several material systems, ranging from magnetic ion nano-clusters[189] and single-molecule magnets[190] to single atoms.[191] However, the integration of magnetic properties within a semiconductor crystal is generally challenging to achieve. This integration is important for several applications and new device concepts in spintronics, including electrical control of the magnetization and generation of spin-currents,[192] spin-filtering[193] and spin-amplification[194] in logic devices. To date,

the realization of magnetic semiconductors has proven to be challenging and it has led to material systems with interesting magnetic and electronic properties.[30-32] Here, we focus on the magnetic anisotropy in InSe containing Fe. We show that the semiconductor vdW crystal InSe, which is non-magnetic in its pristine form, becomes magnetic following the incorporation of Fe-atoms during the growth of InSe by the Bridgman method. The Fe-atoms self-assemble into islands embedded within the InSe host-crystal. The islands are crystalline and have a triangular shape in the plane of the vdW layers. The new materials tend to retain the electronic, optical and vibrational properties of pristine InSe. However, the Fe-islands imprint the InSe crystal with a large uniaxial magnetic anisotropy at room temperature with the magnetization preferentially oriented in the direction perpendicular to the plane of the vdW layers. This combination of magnetic and semiconducting properties within a vdW crystal has the potential for exploitation beyond traditional electronic[17,36] and photonic[29,35,195] applications.

7.2 Fe-islands in InSe van der Waals crystals

The pristine γ-polytype InSe and the Fe-doped γ-InSe crystals were grown using the Bridgman method from a polycrystalline melt of $In_{1.03}Se_{0.97}$, where Fe-dopants were incorporated during the growth at a nominal concentration of 1% and 10%. The growth method is described in section 4.1. Figure 7.1 shows the schematic crystal structure of a hybrid material system where the body centred cubic (bcc) Fe lattice (left) coexists with the rhombohedral γ-polytype InSe. The primitive unit cell of γ-InSe contains three layers each of which has a thickness of $L = 0.8320$ nm ($N = 1$ layer) and consists

of four covalently bonded monoatomic sheets in the sequence Se-In-In-Se; along the *c*-axis, the primitive unit cell has a lattice constant c = 2.4961 nm; within each *a*-*b* plane atoms form hexagons with lattice parameter a = 0.4002 nm (see Figure 2.4a).

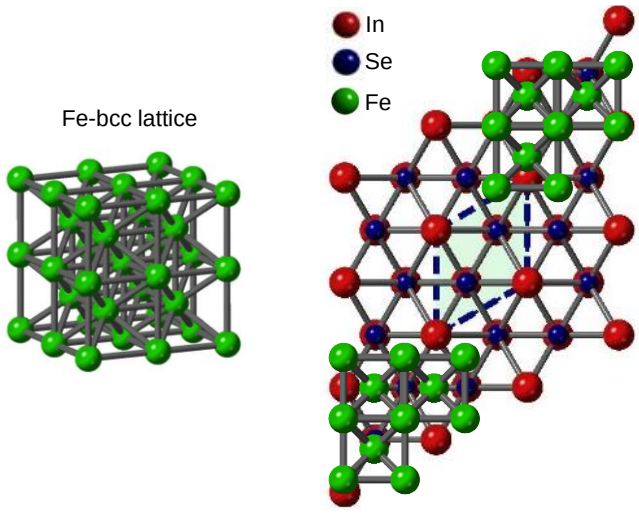

Figure 7.1 Schematic of the crystal structure of a hybrid material system where the body centred cubic (bcc) Fe lattice (left) coexists with the rhombohedral γ-InSe (right).

X-ray diffraction (XRD) patterns for InSe with nominal Fe-content of 0%, 1% and 10% are shown in Figure 7.2 and corresponding lattice parameters are in Table 7.1. The XRD studies of bulk crystals indicate that the lattice parameters are very weakly modified following the incorporation of nominal Fe-content up to 10%.

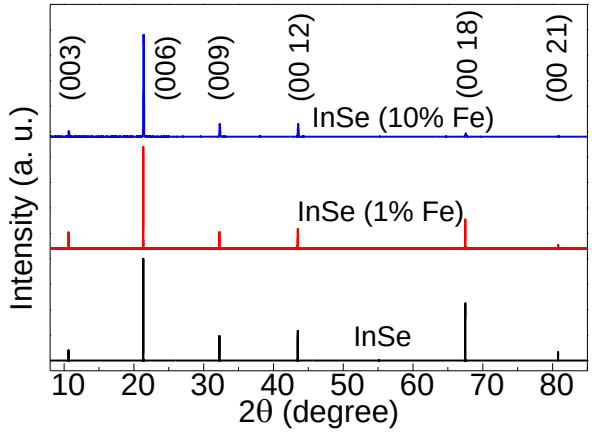

Figure 7.2 X-ray diffraction patterns for InSe with nominal Fe-content of 0%, 1% and 10%.

Table 7.1. Lattice parameters (a, b and c) from XRD studies of InSe:Fe crystals.

Fe (%)	$a = b$ (Å)	c (Å)
0	4.002 ± 0.003	24.950 ± 0.014
1	4.012 ± 0.008	24.953 ± 0.002
10	4.011 ± 0.017	24.905 ± 0.032

However, studies of the crystals by spatially resolved energy-dispersive X-ray (EDX) spectroscopy and transmission electron microscopy (TEM) reveal that the Fe-atoms self-assemble into islands that are randomly oriented in the *ab*-plane (Figure 7.3a). For thick films (thickness $t > 1$ μm), these islands are elongated along the c–axis of the crystal (Figure 7.3b-c). High resolution EDX images show that these Fe-islands have a well defined triangular shape in the *ab*-plane and average area $A \sim 1$ μm^2. The two equal sides of the triangular Fe-islands have length of 0.8 μm (Figure 7.3d). All islands contain a high content of Fe (> 95 %).

Furthermore, the electron diffraction studies reveals that the Fe-atoms are arranged into a body centred cubic (bcc) lattice with lattice constant $a = 2.87$ Å (Figure 7.3e), as for bulk δ-Fe, and are embedded within rhombohedral γ-InSe (Figure 7.3f). Thus our crystals can be described as a hybrid metal-semiconductor system in which the Fe-islands with a bcc lattice (Figure 7.3e) coexist with the rhombohedral γ-InSe (Figure 7.3f). The low solubility of Fe in InSe and the large Fe-content create supersaturation conditions during the Bridgman growth of γ-InSe, thus leading to the formation of two distinct crystals within the same material system.

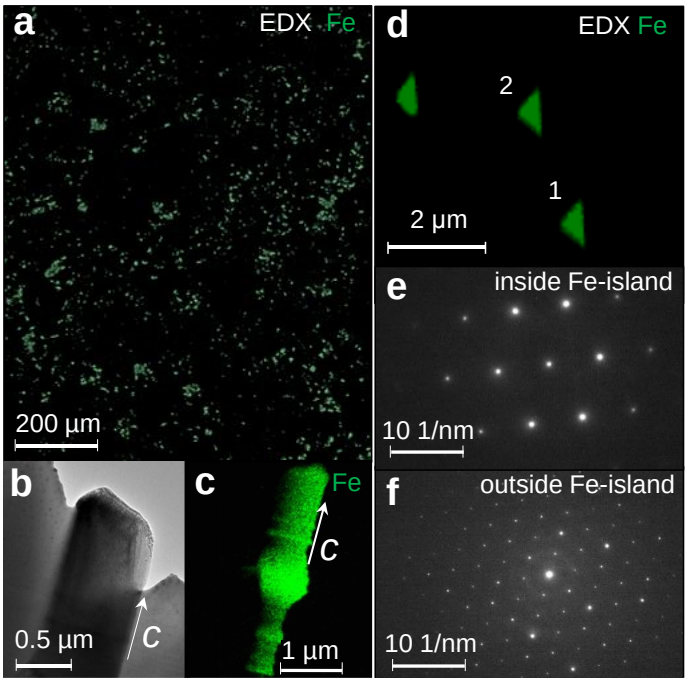

Figure 7.3 a) SEM-EDX maps of the surface of an InSe crystal grown by the Bridgman method with a nominal Fe-content of 10%. Cross-sectional b) TEM image and c) EDX map of an Fe-island in InSe. The island is elongated along the *c*-axis. d) TEM-EDX in-plane map of an InSe thin film (thickness of 100 nm) with nominal Fe content of 10%. Two specific Fe-islands are labelled as 1 and 2. e-f) Electron diffraction patterns within (e) and outside (f) one of the Fe-islands shown in part (d). The two electron diffraction patterns correspond to a bcc Fe-lattice and a rhombohedral InSe crystal, respectively.

Magnetic force microscopy (MFM) measurements were conducted on a thin InSe film (t ~ 100 nm) at the locations of the Fe-islands #1 and #2 highlighted in the EDX image of Figure 7.3d. Figures 7.4a and 7.4b show the acquired AFM and MFM images. Dark and bright contrasts in the MFM images (Figure 7.4b) correspond to magnetic repulsion and attraction, respectively, indicating the presence of perpendicular stray fields emanating from magnetic domains. Both Fe-islands have a similar domain structure suggesting a close similarity in their magnetic properties (Figure 7.4b, top). The enlarged AFM and MFM images in the bottom of Figures 7.4a and 7.4b show with greater detail the shape, orientation and height of an individual Fe-island and its 3-fold multi-domain state. By comparing the morphology and the domain structure of

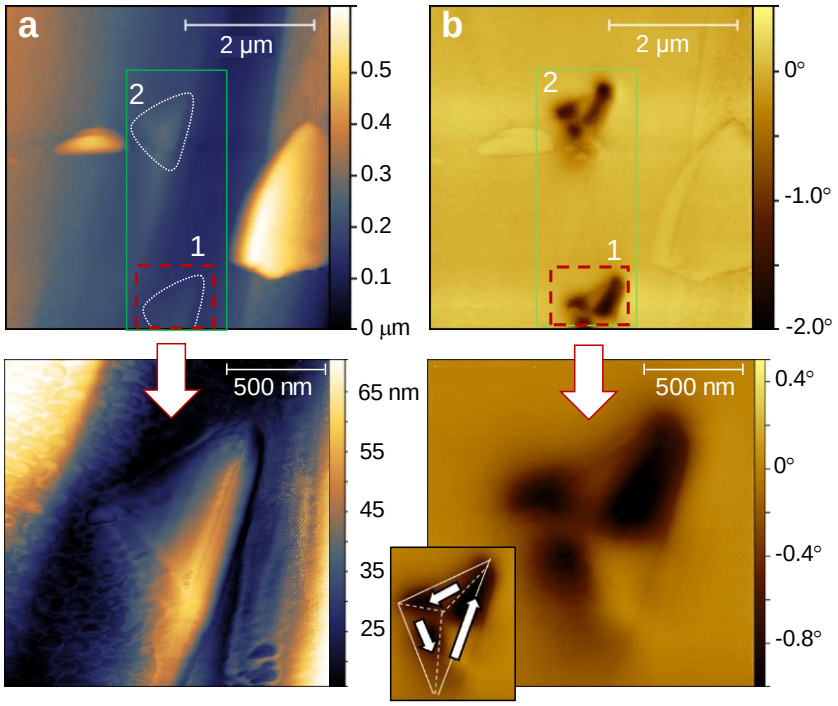

Figure 7.4 a) Top: AFM image of the InSe film shown in Fig.7.3d, with Fe-islands outlined in white. The region corresponding to the Fe-islands #1 and #2 is marked by a green rectangle. Bottom: enlarged AFM image of Fe-island #1. b) Top: MFM image showing the multi-domain domain structure of Fe-islands #1 and #2 (h = 25 nm). Bottom: enlarged MFM image for Fe-island #1 (h = 50 nm). Inset: sketch of the multi-domain structure.

this island, we conclude that the domain structure is three-dimensional. The largest domain on the right-hand side morphs around the upper-right-hand edge. The two other domains are similar in size, completing the domain closure in an anticlockwise fashion to minimize the energy, as shown in schematic in the left bottom corner of Fig. 7.4b. These findings demonstrate that ferromagnetic Fe-islands with a bcc lattice are embedded with the rhombohedral γ-InSe crystal. The MFM results on thin films (t ~ 100 nm) of InSe containing Fe-islands reveal that the magnetic domains point in the layer plane, perpendicular to the c-axis of the sample. However, from the electron spin resonance measurements on a thicker InSe sample containing Fe-islands, we deduce that the easy axis of magnetisation is along the c-axis (section 7.4). We attribute this inconsistency

in the direction of the magnetisation to the shape anisotropy of the sample, *i.e.* in the case of our thin sample, the magnetisation prefers to align in the plane (perpendicular to the *c*-axis) to avoid the energy cost associated with the demagnetising field, as discussed in section 3.3.2.

7.3 Semiconducting properties of Fe-containing InSe

Figure 7.5a shows the room temperature photoluminescence (PL) spectra for bulk InSe:Fe with different nominal Fe-content. Irrespectively of the Fe-content, we find that for all our InSe bulk crystals the energy peak position of the room temperature (T = 292K) photoluminescence (PL) emission is centred at an energy hv = 1.25 eV (Figure 7.5a) and the Raman peaks are at 115.7, 179.2, 201.2, 212.4, 228.0 cm^{-1}, as observed for pristine bulk InSe (Figure 7.5b). With increasing Fe-content, the intensity of the optical signals

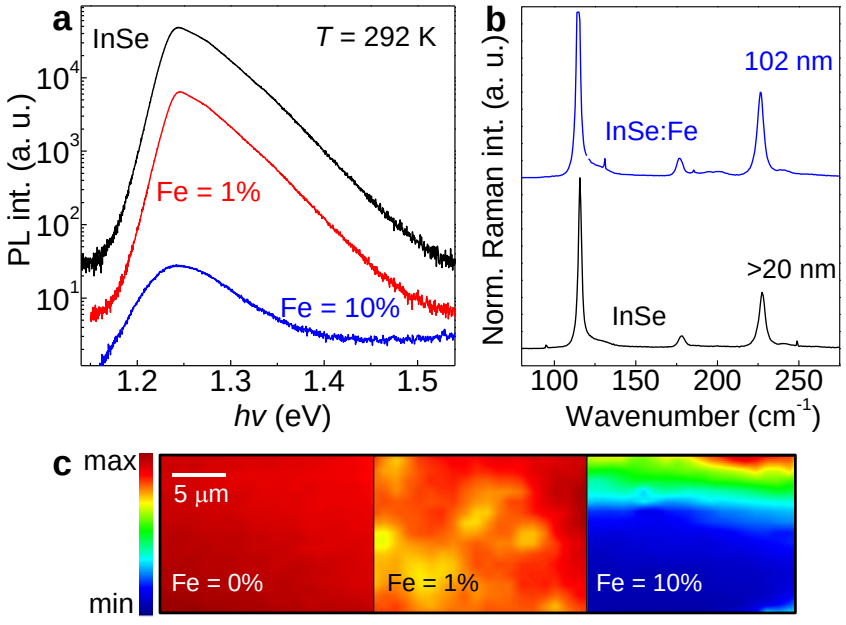

Figure 7.5 a) Room temperature photoluminescence (PL) spectra for bulk InSe:Fe with nominal Fe-content of 0 (black), 1% (red) and 10% (blue). b) Normalised Raman spectra for exfoliated bulk flakes of InSe and InSe with nominal Fe-content of 10%. c) Maps of the PL intensity for bulk InSe with nominal Fe-content of 0, 1% and 10% (λ = 633 nm; P = 0.1 mW).

tends to decrease and spatial maps of the PL intensity reveal an increasing non-homogeneity over length scales of a few microns (Figure 7.5c). Correspondingly, the room temperature conductivity in the layer plane decreases due to a reduction of the electron mobility from $\mu \sim 10^3$ cm^{2}V^{-1}s^{-1} in pristine InSe to $\mu \leq 10^2$ cm^{2}V^{-1}s^{-1} in the InSe crystals containing Fe. Thus, despite the incorporation of Fe-islands in InSe, the crystal preserves many of the functional properties of pristine InSe.

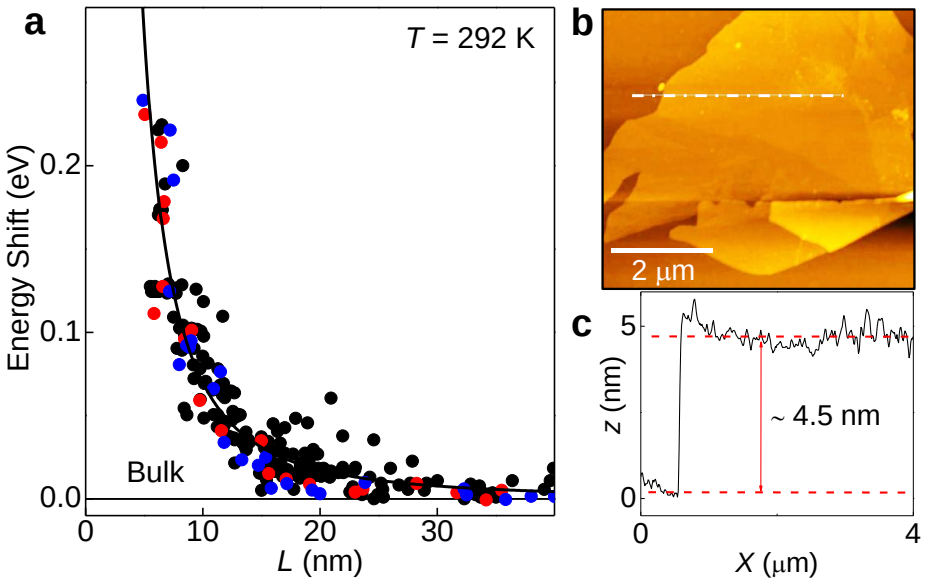

Figure 7.6 a) Energy shift of the room temperature photoluminescence (PL) peak versus the layer thickness L for InSe layers with nominal Fe-content of 0 (black), 1% (red) and 10% (blue). The solid line is the energy shift calculated using an effective mass quantum well model. b) AFM image and c) corresponding z-profile for an InSe flake exfoliated from a 10% Fe-containing InSe crystal.

Furthermore, despite the high Fe-content, all of the Fe incorporated crystals can be exfoliated into thin layers and the PL emission peak undergoes a strong blue-shift ΔE with decreasing layer thickness L (Figure 7.6a-c). The measured energy shift is in agreement with that observed and calculated for pristine InSe (Figure 7.6a).[34] In our quantum well model, the energy shift is described as $\Delta E = h^2/8L^2\mu$ (continuous line in Figure 7.6a), where μ = 0.054

m_e, is the exciton mass and m_e is the electron mass in vacuum, as calculated from the measured values of the electron and hole masses for motion along the *c*-axis in bulk InSe.[196,197] A similar energy shift is calculated from density functional theory (DFT).[37]

7.4 Uniaxial magnetic anisotropy at room temperature

Although the semiconducting behaviour of our samples is preserved, the magnetic properties of InSe are modified after the incorporation of Fe. As shown by MFM (Figure 7.4b), magnetic domains are observed at room temperature and are localized within the Fe-islands. Also, room temperature superconducting quantum interference device (SQUID) studies show a ferromagnetic behaviour (Figure 7.7) for InSe with 10% Fe. In particular, the magnetisation saturates at lower magnetic fields for **B** parallel to the *c*-axis than for **B** in the *ab*-plane. This indicates that the *c*-axis is the easier axis of magnetisation of the crystal.

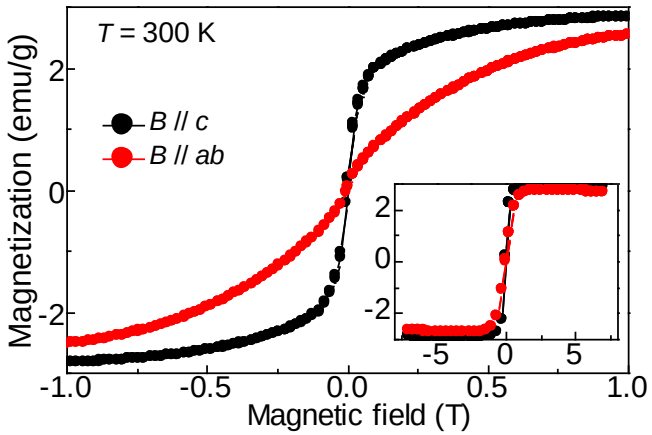

Figure 7.7 Magnetic field dependent magnetization at T = 300K for an InSe crystal with nominal Fe = 10% and **B** oriented parallel to the *c*-axis and to the *ab*-plane. Inset: Magnetisation vs magnetic field at T = 300K.

To obtain a better understanding of the magnetic properties of the crystal, we conducted electron spin resonance (ESR) studies. Figure 7.8a shows

typical room temperature (T = 292K) ESR spectra measured at Q-band (frequency ν = 34.229 GHz) for bulk InSe containing Fe-islands. The experiment is conducted in perpendicular mode, *i.e.* the external magnetic field **B** is perpendicular to the microwave field; also, **B** is at angle ϑ_B relative to the c-axis (out-of-plane geometry, inset of Figure 7.8a). For **B** parallel to the c-axis (*i.e.* $\vartheta_B = 0°$), the ESR spectrum reveals two strong ferromagnetic resonances at B = 0.199T and 0.326T, corresponding to effective g-values of g_1 = 12.3 and g_2 = 7.5, respectively. These two ferromagnetic resonance lines are due to the zero-field splitting of the energy levels, as discussed in section 3.5. The large effective g-value (*e.g.* g_1 = 12.3, g_2 = 7.5 for $\vartheta_B = 0°$) differs significantly from that expected for isolated Fe ions, *i.e.* g ~ 4.3 and 2.[198] The large g-factors demonstrate strong ferromagnetic spin-spin interactions in the crystalline Fe-islands, leading to an internal magnetic field. We note that ESR signals were not detected in pristine InSe.

The position, linewidth and intensity of the resonances are strongly sensitive to the orientation of **B** with a periodic modulation and turning points that occur when **B** is aligned close to main crystallographic directions, *i.e.* parallel to the c-axis ($\vartheta_B = 0°$, 180° and 360°) or to the ab-plane ($\vartheta_B = 90°$ and 270°). For example, the intensity of the main ESR line (g_2) has minima at angles close to $\vartheta_B = 90°$ and 270° (Figure 7.8b); correspondingly, the resonance field B_{res} reaches maxima at B ~ 1.5T (Figure 7.8c) and the resonance linewidth ΔB increases by more than a factor of 5 (Figure 7.8d). When the crystal is rotated in the out-of-plane geometry, the resonance field B_{res} increases for ϑ_B going from $\vartheta_B = 0°$ to ~ 90°. This suggests that by rotating the crystal off the c-axis, the applied magnetic field required to meet the magnetic resonance condition

increases. The opposite behaviour is observed when the crystal is rotated from $\vartheta_B \sim 90°$ to $\sim 180°$. This orientation dependence of the ESR lines demonstrates that this internal magnetic field has uniaxial magnetic anisotropy with easy axis parallel to the *c*-axis and perpendicular to the plane of the triangular Fe-islands.

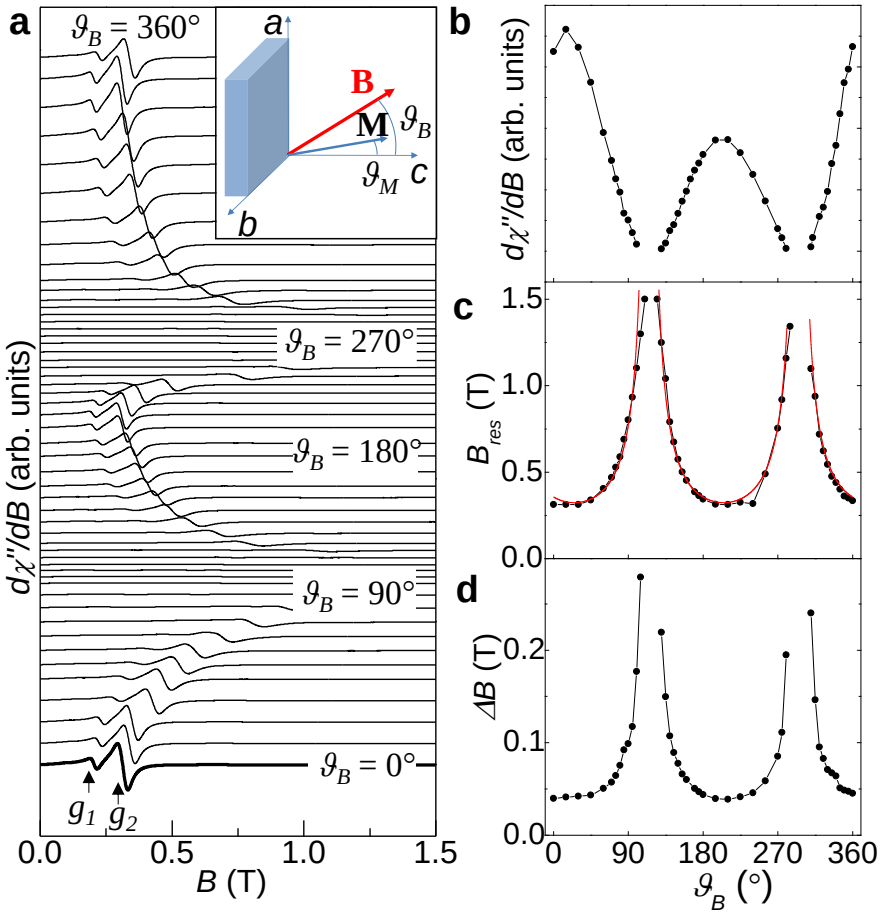

Figure 7.8 a) Angle-dependent ESR spectra of an InSe crystal with nominal Fe content of 10% (*Q*-band and T = 292K). The ESR spectra are shifted vertically for clarity. The step in the increment of the angle ϑ_B is 5°. Inset: Orientation of the magnetic field **B** and magnetization **M** relative to the crystallographic *c*-axis of InSe. b-c-d) ESR intensity, resonance field B_{res} and linewidth ΔB of the resonance g_2 versus ϑ_B. The red curve in part c) is the simulation of the data by equation (7.1) in the text. Black lines in parts b-c-d are guides to the eye.

We model the measured angular dependence of the resonance field B_{res} by equation (7.1), which is commonly used for systems with uniaxial magnetic anisotropy in an out-of-plane configuration[199]:

$$\left(\frac{\omega}{\gamma}\right)^2 = \left[B_{res}\cos(\vartheta_M - \vartheta_B) - 4\pi M_{eff} cos2\vartheta_M\right] \times$$

$$\left[B_{res}\cos(\vartheta_M - \vartheta_B) - 4\pi M_{eff}\, cos^2\vartheta_M\right]. \quad (7.1)$$

Here, γ is the gyromagnetic factor, and ϑ_M and ϑ_B are the angles between the *c*-axis and the magnetization, **M**, and external magnetic field, **B**, respectively (inset of Figure 7.8a). The term $4\pi M_{eff}$ represents an effective demagnetizing field defined as $4\pi M_{eff} = 4\pi M_s - 2K/M_s$, where M_s is the saturation magnetization, $B_d = 4\pi M_s$ is the demagnetizing field, $B_a = 2K/M_s$ is the anisotropy magnetic field, and K is an anisotropy constant. The simulation of the angular dependence of B_{res} in Figure 7.8c gives K = -9 x 10^3 J/m^3 and an anisotropy field $\mathbf{B_a}$ oriented close to the *c*-axis with amplitude $B_a \approx 1$T. We have assumed M_s = 3 emu/g (B_d = 2.7 x 10^{-1}T), as obtained from our SQUID studies (Figure 7.7), and $\gamma = 2\pi g\mu_B/h$ with g = 2.09.[167,200] We describe the angular anisotropy of the resonance linewidth ΔB (Figure 7.8d) as:

$$\Delta B = \Delta B_0 + \Delta B_G, \quad (7.2)$$

where ΔB_0 is the inhomogeneous linewidth broadening. This is attributed to the non-homogeneous internal magnetic field arising from the random distribution of the Fe-islands (Figure 7.3a) and is independent of the angle ϑ_B. The second term describes the damping, which is expressed as $\Delta B_G \approx \frac{2}{\sqrt{3}}\frac{\alpha\omega}{\gamma cos\beta}$, where α is the dimensionless Gilbert damping parameter, and β is the angle between the magnetisation (M) and the applied field (B).[201] The term $cos\beta$ is the field dragging term and plays an important role in the resonance linewidth broadening since the magnetisation is dragged behind the applied field when they are nonparallel. When $\mathbf{B_{eff}}$ is parallel to the *c*-axis, the external magnetic field and the magnetization direction are parallel and ΔB has a minimum; in

contrast, in the out-of-plane rotation of $\mathbf{B_{eff}}$, ΔB first increases by about 10 % for $\vartheta_B \sim 45°$ and then increases steeply for ϑ_B approaching a value of $\vartheta_B \sim 90°$ (Figure 7.8d). Thus the angular dependence of ΔB suggests a magnetic dragging effect due to the non-collinearity of the external magnetic field and the magnetization direction.[201] The contribution to the linewidth broadening ΔB of the Gilbert parameter (Equation 7.2) implies angular momentum losses of the magnetization precession in the magnetic Fe-islands into the non-magnetic InSe matrix. This spin-pump mechanism[192] occurs at room temperature, offering prospects for the generation of a charge current in InSe via the inverse spin Hall effect (ISH).[202]

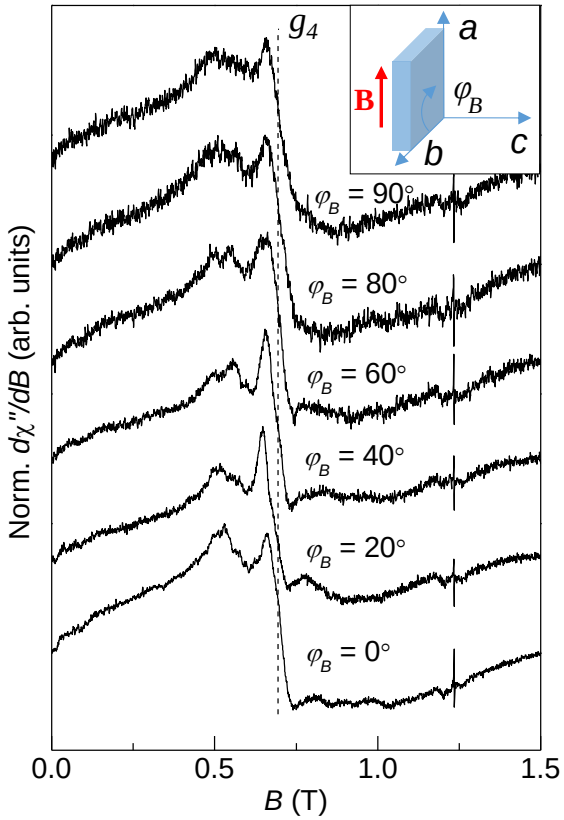

Figure 7.9 Angular rotation (**B** in the *ab*-plane, see inset) dependent ESR spectra of InSe with nominal Fe = 10% (*Q*-band and *T* = 292K). The ESR spectra are shifted along the vertical axis for clarity.

Angular rotation dependence ESR spectra were also acquired for **B** in the *ab*-plane (Figure 7.9). The inset of Figure 7.9 shows the orientation of **B** in

the *ab*-plane. For this orientation dependent ESR studies, g_1 and g_2 cannot be clearly resolved; however, a narrow ESR line is observed at $g_4 = 3.6$, which has weak dependence on the orientation of **B** in the *ab*-plane.

7.5 Magnetic phases induced by Fe-islands in InSe

The uniaxial magnetic anisotropy is observed at room temperature and it depends only weakly on temperature, as assessed by SQUID (Figure 7.10). This dependence is different from that expected for ferromagnetic bulk δ-Fe due to the coexistence of mixed phase states within a system that consists of a diamagnetic InSe crystal and ferromagnetic Fe-islands (Figure 7.4).

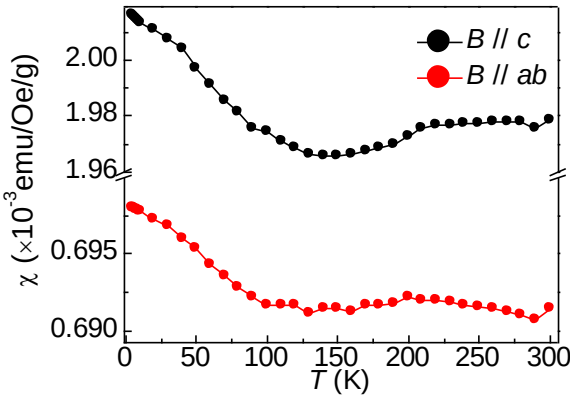

Figure 7.10 Temperature dependence of the magnetic susceptibility for an InSe crystal with nominal Fe = 10%. The magnetic field **B** is oriented parallel to the *c*-axis and to the *ab*-plane.

We examine further this *T*-dependence by ESR: the intensity of an ESR line is proportional to the first derivative of the imaginary component of the magnetic susceptibility, $d\chi''/dB$. Thus the temperature dependence of an ESR line is used to probe the existence of different magnetic phases. Figure 7.11a shows the *T*-dependence of the ESR spectra for **B** parallel to the *c*-axis. It can be seen that resonances g_1 and g_2 are observed over a wide range of temperatures from 5K to 300K. From these ESR measurements (*B*//*c*), it is possible to derive

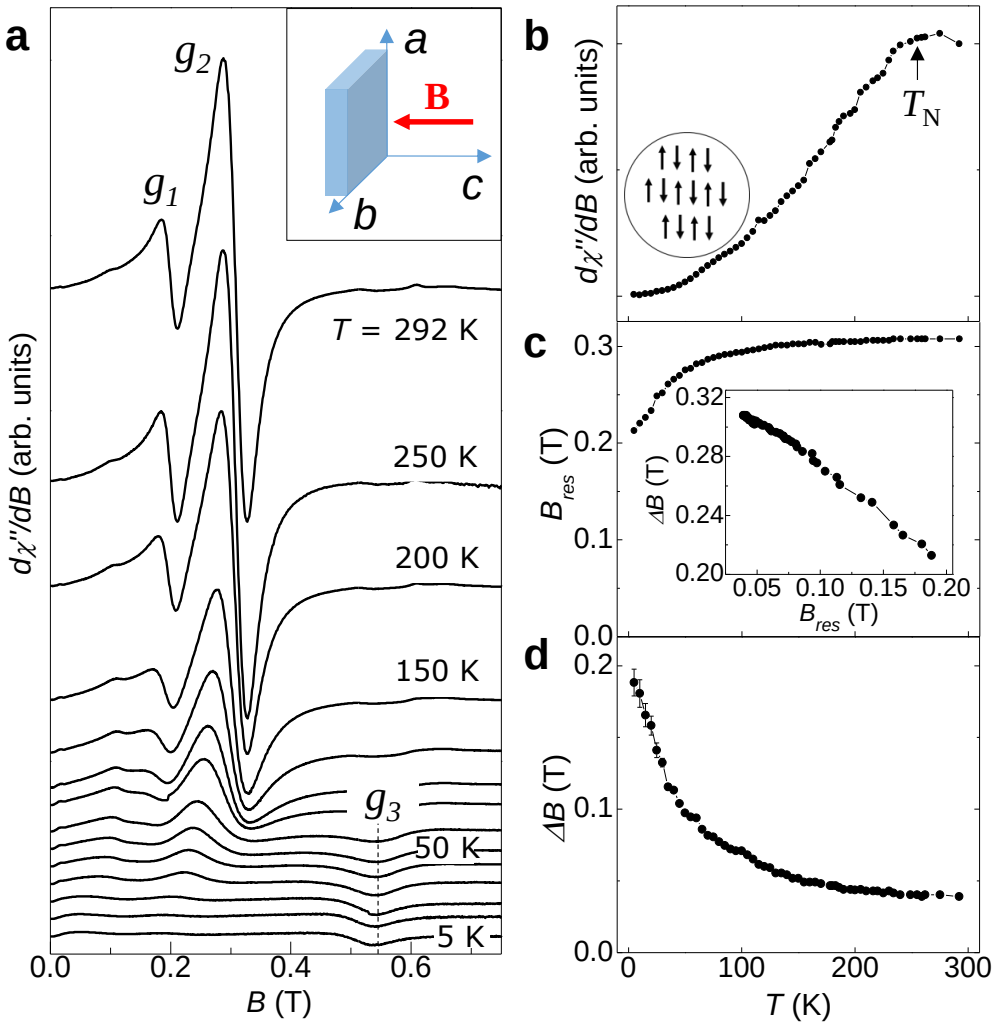

Figure 7.11 a) Temperature-dependent ESR spectra for an InSe crystal with nominal Fe = 10% (*Q*-band and **B** parallel to the *c*-axis). Inset: Orientation of **B** relative to the crystallographic *c*-axis of InSe. The ESR spectra are shifted along the vertical axis for clarity. Temperature values from top to bottom are *T* = 292, 250, 200, 150, 120, 100, 80, 60, 50, 40, 30, 20, 10 and 5K. b-c-d) ESR intensity, resonance field B_{res} and linewidth ΔB of resonance g_2 versus *T*. The inset in b) sketches the low *T* antiferromagnetic order. The inset in c) shows the correlation between the resonance linewidth and resonance field.

the *T*-dependent peak-to-peak intensity, resonance field and linewidth for resonance g_2, see Figure 7.11b-d. The ESR intensity decreases steeply from a broad maximum centred at $T \approx 260$K to approximatively zero for $T < 50$K (Figure 7.11b). The weakening of the main ESR lines, g_1 and g_2, with decreasing temperature differs from the dependence expected for a ferromagnet. It suggests the emergence of an anisotropic antiferromagnetic (AF) order at a Néel

temperature $T_N \approx 260$K (Figure 7.11b) and a magnetisation oriented along the *c*-axis. In the same range of temperatures, the resonance magnetic field B_{res} shifts to lower values (Figure 7.11c) and the ESR linewidth broadens (Figure 7.11d), with a linear correlation between the resonance field and the linewidth (inset of Figure 7.11c).

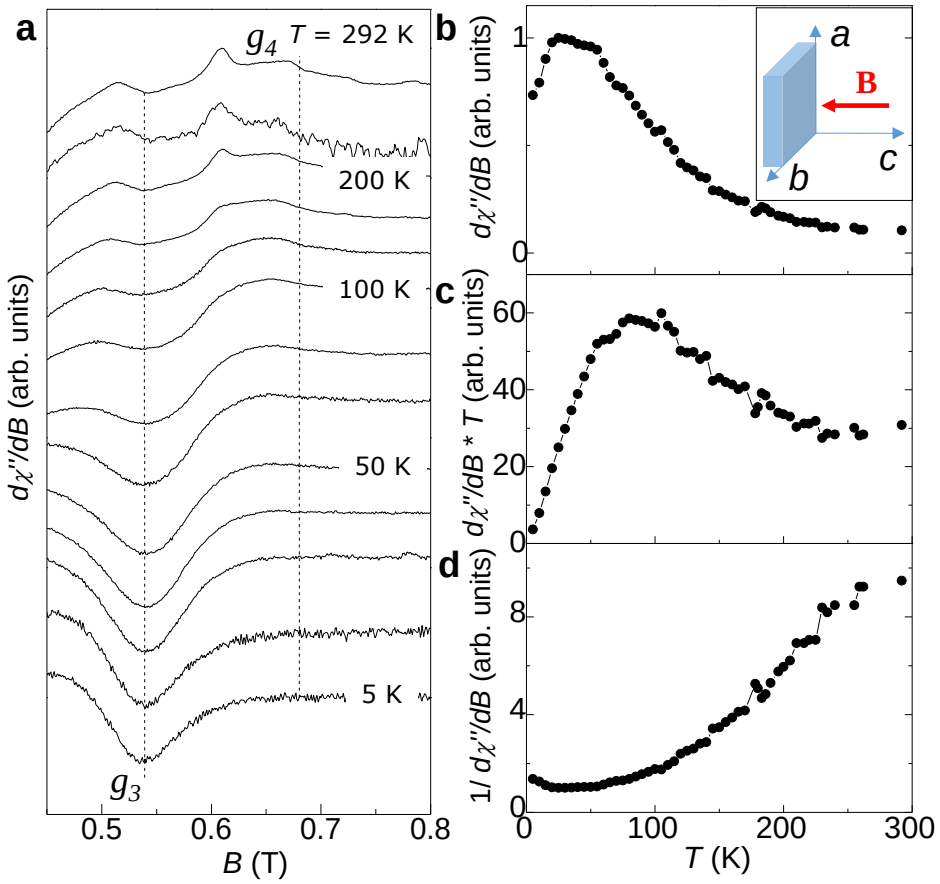

Figure 7.12 a) Temperature-dependent ESR spectra for an InSe crystal with nominal Fe = 10% (*Q*-band and *B* parallel to the *c*-axis, see inset). The ESR spectra are shifted along the vertical axis for clarity. Temperature values from top to bottom are *T* = 292, 250, 200, 150, 120, 100, 80, 60, 50, 40, 30, 10 and 5K. b-c-d) ESR intensity, ESR intensity times temperature and reciprocal ESR intensity of resonance g_3 versus *T*.

Also, for $T < 100$K, a weak resonant feature emerges at $B = 0.537$T ($g_3 \sim 4.6$) accompanied by a small magnetic field shift of about 24 mT (Figure 7.11a) suggesting a possible rotation of the easy axis of magnetisation with temperature. This weak ESR line g_3 has a *T*-dependence that differs from that

of the dominant narrow ESR signals g_1 and g_2 (Figure 7.11a). Temperature dependent ESR spectra and the *T*-dependence of $d\chi''/dB$, $d\chi''/dB*T$ and $1/d\chi''/dB$ for resonance g_3 are plotted in Figure 7.12a-d. For the g_3 line the temperature dependence $d\chi''/dB$ plot (Figure 7.12b) reveals that the ESR intensity increases with decreasing temperature and reaches a maxima at $T \sim$ 25K after which it starts to decrease steeply. In summary, the *T*-dependence of the ESR lines differs from that expected for a ferromagnetic system.

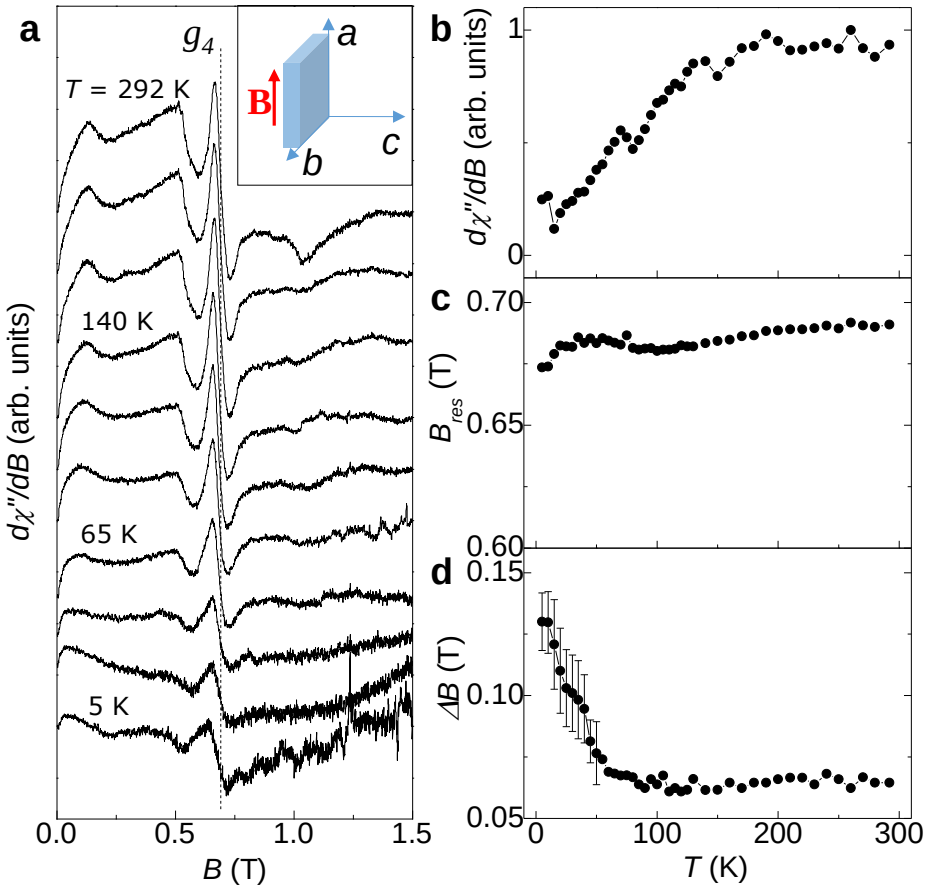

Figure 7.13 a) Temperature-dependent ESR spectra for InSe with nominal Fe = 10% (*Q*-band and **B** in the *ab*-plane, see inset). The ESR spectra are shifted along the vertical axis for clarity. Temperature values from top to bottom are *T* = 292, 220, 200, 140, 115, 95, 65, 45, 35 and 5K. b-c-d) ESR intensity, resonance field and linewidth of resonance g_4 versus *T*.

Temperature dependent ESR spectra were also acquired for **B** in the *ab*-plane for a wide range of temperature (5K – 292K). Figure 7.13a shows the *T*-dependence of the ESR spectra for **B** in the *ab*-plane. For this orientation of **B**,

g_1 and g_2 cannot be clearly resolved; however, a narrow ESR line is observed at g_4 = 3.6 (B = 0.680T). The T-dependent peak-to-peak intensity, resonance field and linewidth for resonance g_4 are plotted in Figure 7.13b-d. This temperature dependence behaviour is similar to that observed for g_1 and g_2 for $\boldsymbol{B}$ applied parallel to c-axis.

To account for these complex behaviours, we note that Fe-containing nanomaterials have magnetic properties that are distinct from those of bulk δ-Fe, which is FM. An AF order with a Néel temperature T_N up to 100K was reported for γ-Fe thin films with face-centered cubic (fcc) crystal symmetry obtained by epitaxial growth[203,204] or precipitation[205]; an AF order can emerge when bcc δ -Fe undergoes a crystal phase transition to fcc below a critical layer thickness[206,207] due to stronger magnetic interactions arising from a smaller lattice constant[208] and/or surface/interface effects[209]; AF and FM orders can also coexist within Fe-clusters due a composite crystal structure.[210] The coexistence of different magnetic phases in our system may arise from non-equivalent Fe-atoms in the islands and strain effects at the interface with the diamagnetic InSe, which requires further investigation.

Theories and earlier studies of magnetic resonances showed that these resonances can quench as the temperature is lowered below the Néel temperature. Also, for an ideal antiferromagnet $\chi_{//}$ approaches zero as the temperature goes to zero.[211,212] Measurements in real uniaxial antiferromagnets often show a finite $\chi_{//}$ at low temperature.[211] A phenomenological theory suggests that the low microwave frequency is the reason for the disappearance of the ESR lines on cooling the antiferromagnetic crystal below its Néel temperature.[213] In general, identifying directly magnetic phases in our complex

hybrid material system is difficult. Further studies require investigations at different magnetic fields and/or microwave frequencies with nanoscale spatial resolution.

7.6 Doping and intercalation of InSe with transition metals

To create an homogeneous ferromagnetic semiconductor,[121] we have explored different methods for incorporating transition metals (TMs: Fe, Mn, Ni) in InSe. These methods involve the incorporation of the TMs during the Bridgman growth or the intercalation of the TMs after the growth of InSe. These methods are described in section 4.1. The results of these studies are described below.

7.6.1 Doping of InSe with TMs

The EDX analysis of the InSe crystals doped with TMs reveals that at high concentration (> 0.5%) the TMs tend to form clusters that are randomly distributed throughout the InSe crystal (Figure 7.3a and 7.14a). Using EDX, we were not able to assess whether the TMs are incorporated on the In and/or Se sites, or as interstitials (Figure 7.14c). In contrast, at low concentration the EDX analysis indicates an homogeneous distribution of TMs (Figure 7.14b). However, in this case the detection of small concentrations of TMs (< 0.5%) is difficult due to the sensitivity of the EDX detector (Figure 7.14d).

To study the magnetic properties of these crystals, we conducted SQUID measurements. The room temperature magnetic field dependence magnetisation (M) studies of 0.5% Mn doped InSe show a paramagnetic behaviour for $B//c$ and $B//ab$ (Figure 7.15a). This paramagnetic behaviour is observed at temperature down to $T \sim 188$K. For $T < 188$K, the magnetisation decreases with

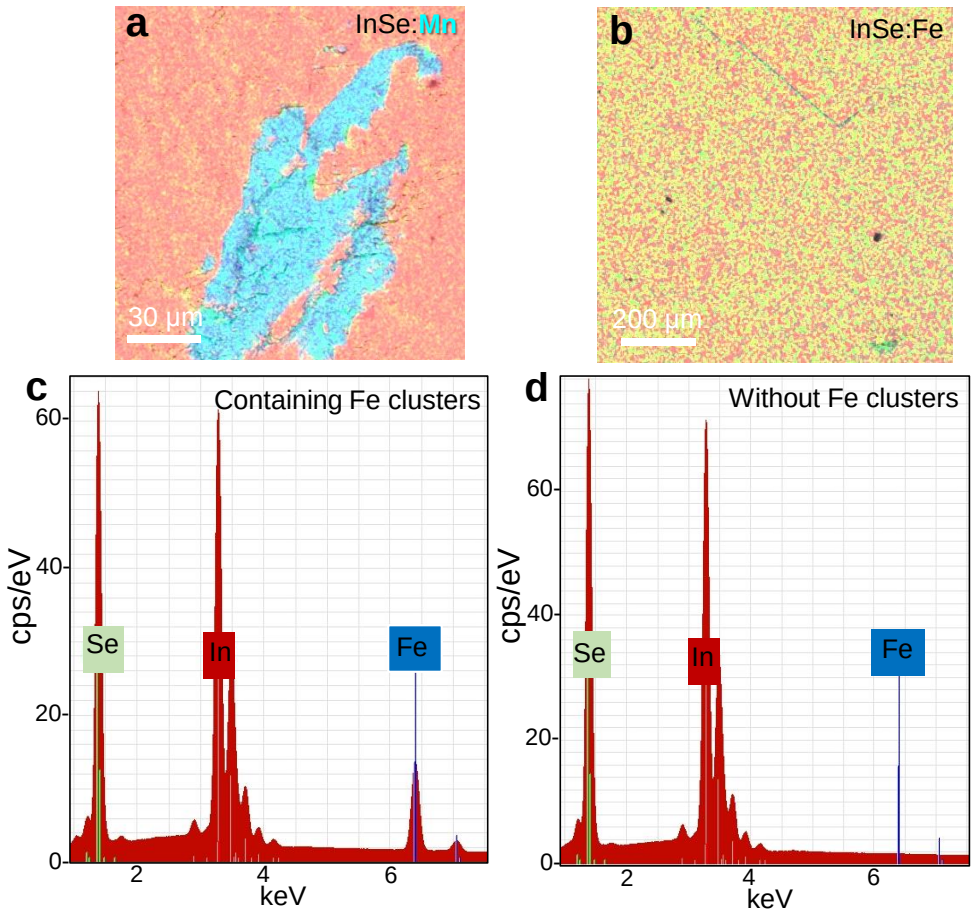

Figure 7.14 In-plane EDX maps of (a) 0.5% Mn doped, (b) 1% Fe doped InSe crystals. EDX spectra of InSe:Fe crystals containing Fe clusters (Fe = 10%) (c) and without any cluster (Fe = 1%) (d).

decreasing temperature (Figure 7.15b). The temperature at which the magnetisation starts to decrease is the Néel temperature (T_N). For $T < T_N$, adjacent magnetic moments tend to align in opposite directions and the system becomes antiferromagnetic. The low temperature field dependent magnetisation measurements also show an anomalous behaviour close to $B \approx 0$ for both $B//c$ and $B//ab$ (Figure 7.15c). For instance, in the low field regime, the magnetisation curve for $B//ab$ reveals a narrow hysteresis for ascending and descending sweeps of the field and a strong enhancement of M at $B < 0.05$T (Figure 7.15d). This unusual behaviour may arise from a superconducting phase at low temperature (T = 2K). We propose that this may originate from In-

clusters in InSe (In is superconducting at T ~ 3.4K).[214-216] External contamination could also be an alternative possibility.

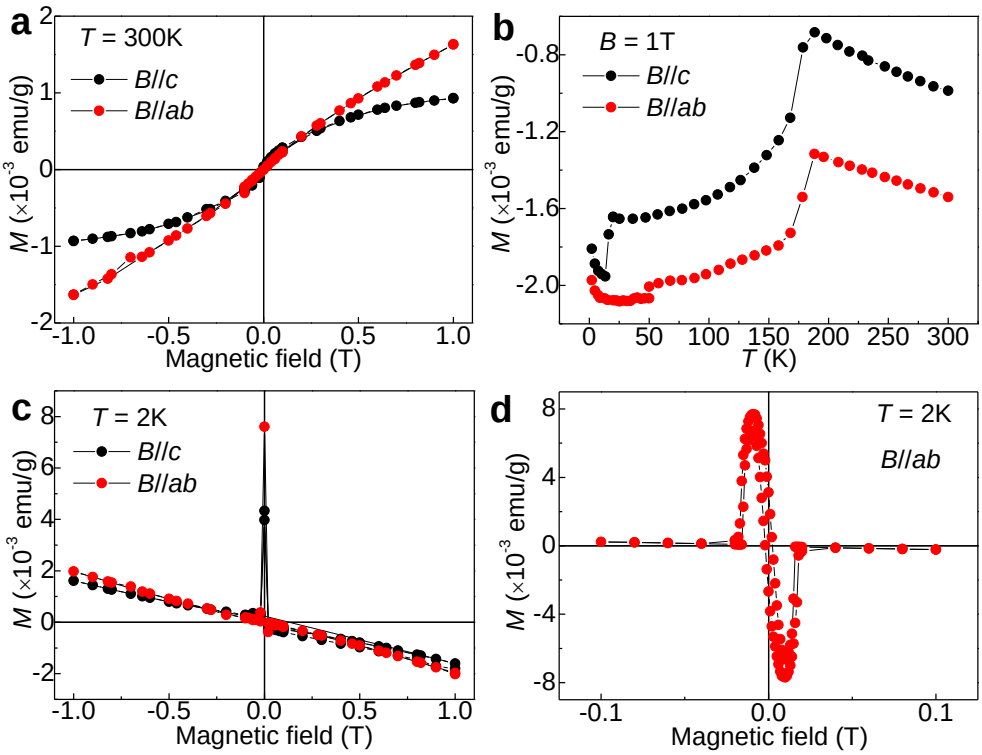

Figure 7.15 (a) *B*-dependence of the magnetisation at T = 300K; (b) *T*-dependence of the magnetisation at B = 1T; (c) *B*-dependence of the magnetisation at T = 2K for $B//c$ and $B//ab$. (d) *B*-dependence of the magnetisation at T = 2K for $B//ab$. All measurements are for an InSe crystal doped with 0.5% Mn.

7.6.2 Intercalation of InSe with TMs

We have studied InSe crystals intercalated with TMs. In this case the TMs are incorporated by electrochemical intercalation and one could expect that they tend to be incorporated in the vdW gaps between the Se planes of adjacent layers. The EDX studies of the InSe crystal intercalated with 15% Ni reveals that the intercalant Ni atoms form clusters instead of being homogeneously distributed and that these clusters are randomly distributed throughout the InSe crystal (Figure 7.16a). We have studied the magnetic properties of this crystal by SQUID. The room temperature magnetic field dependent magnetisation

studies for *B*//*c* and *B*//*ab* do not show any hysteresis and the magnetisation goes to zero at zero field, which implies a paramagnetic behaviour (Figure 7.16b). From the magnetisation curves at T = 300K, one might think that the saturation of the magnetisation occurs at lower field for *B*//*c* than for *B*//*ab*. However, we note that the saturation in magnetisation curves may be an artifact: It could arise from the subtraction of the diamagnetic background (see the field dependence magnetisation curve without background subtraction in the inset of Figure 7.16b).

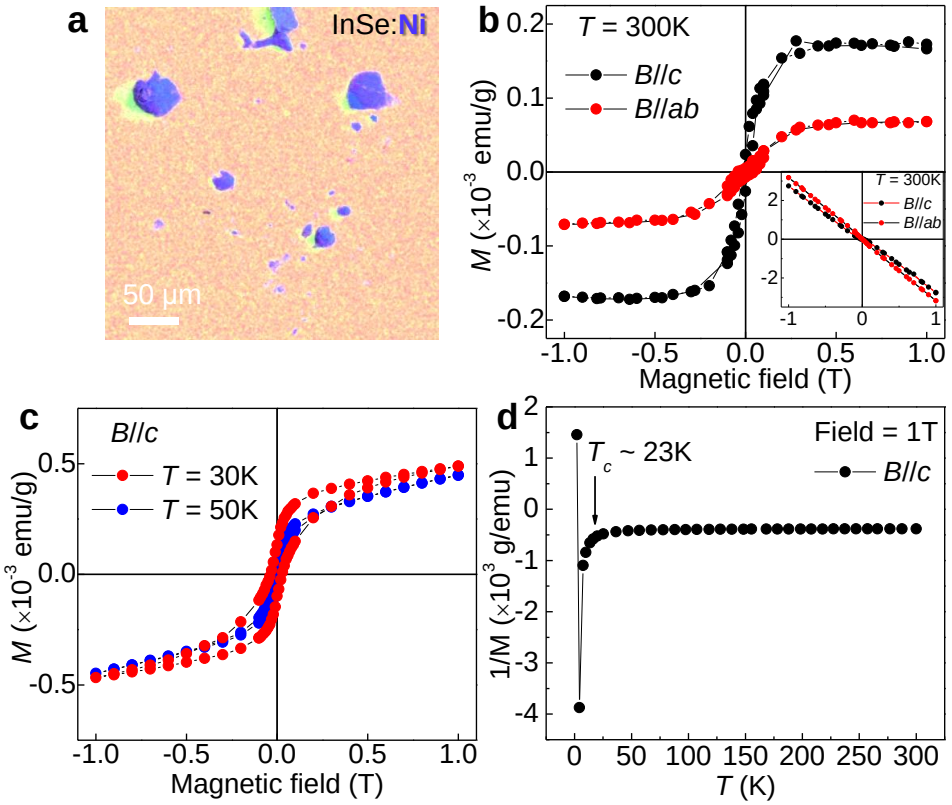

Figure 7.16 (a) In-plane EDX map of an InSe crystal intercalated with 15% Ni. (b) Field dependence magnetisation curve at T = 300K for the field oriented parallel to the *c*-axis and to the *ab*-plane of the crystal. Inset: Magnetisation vs magnetic field at T = 300K for *B*//*c* and *B*//*ab* without diamagnetic background subtraction. (c) Magnetisation curve at two different temperatures for *B*//*c*. (d) 1/*M* vs T for the applied field parallel to the *c*-axis of the crystal. The arrow indicates the Curie temperature (T_c).

We conducted SQUID measurements at different temperatures (*e.g.* T = 30, 50K) for *B*//*c*, as shown in Figure 7.16c. At low T, the magnetisation shows

an hysteresis behaviour, suggesting a transition from a paramagnetic to a ferromagnetic phase at around $T \sim 30$K. In the temperature dependence of the magnetisation one might expect a standard ferromagnetic behaviour, but this is not the case (see Figure 7.16d). From the temperature dependence of $1/M$ (Figure 7.16d), we observed that the magnetisation starts to diverge at $T \sim 23$K. The deviation of the T-dependent magnetisation from the usual ferromagnetic characteristic curve may be due to the coexistence of mixed phase states within an hybrid system, which consists of a diamagnetic InSe crystal and ferromagnetic clusters.

In summary, our studies show that the incorporation of TMs either by doping during the Bridgman growth or by electrochemical intercalation after the Bridgman growth of InSe can induce magnetism. But in both cases, the TMs tend to form clusters. The formation of TM-clusters was previously reported by other groups for Bridgman grown InSe crystals doped with Co.[217] The low solubility of TMs in InSe might be responsible for the cluster formation. Further developments of the growth technique are required to incorporate substitutional TMs in InSe and create an homogeneous magnetic crystal.

7.7 Summary

Recent advances in the science and technology of 2D vdW crystals, which includes graphene, hBN, transition metal dichalcogenides and many others, have demonstrated the potential of this class of materials for novel functional devices. Among these 2D crystals, InSe has emerged as a semiconducting system with unprecedented properties, *e.g.* high electron mobility[17] and strong photosensitivity[29,35]. This semiconductor vdW crystal,

which is non-magnetic in its pristine form becomes magnetic following the incorporation of Fe-atoms. The Fe-atoms self-assemble into triangular shaped Fe-clusters and imprint the semiconductor with a large uniaxial magnetic anisotropy at room temperature. The magnetization is preferentially oriented in the direction perpendicular to the plane of vdW layers and arises from magnetic cooperative interactions between neighbouring Fe-spins within each cluster. In stark contrast to other magnetic semiconductors, the incorporation of a large content of Fe in the InSe crystal does not modify the fundamental electronic properties of the semiconductor. Thus, this hybrid system, which consists of ferromagnetic Fe-inclusions and a semiconducting van der Waals InSe crystal, enables the coexistence of magnetic and semiconducting properties within the same structure. This new hybrid material system offers prospects for new functional devices based on spin-injection into nonmagnetic InSe from magnetic Fe-island and its control by the magnetic anisotropy of the crystal. However, further development on the homogeneous incorporation of transition metals in InSe is required to synthesize an homogeneous magnetic semiconductor, which is expected to be ferromagnetic.[121]

Chapter 8

Conclusions and outlook

The aim of my PhD was to explore the integration of InSe two-dimensional (2D) semiconducting layers in graphene-based field effect transistors (FETs) and to investigate the charge transfer at the interface between InSe and graphene. Also, my research focussed on the magnetic properties of a new hybrid material system, which comprises InSe and ferromagnetic Fe-islands. The key findings of this work can be summarised as follows.

(i) InSe can be employed in graphene-based FETs as an electrically active capping layer to "modulation-doped" graphene, thus leading to a "giant" quantum Hall (QH) effect plateau in its magnetoresistance, which extends over a wide range of applied magnetic fields and temperatures.

(ii) The electronic properties of InSe/graphene phototransistors can be controlled by a combination of optical illumination and field effect gating. In particular, the photoresponse of graphene is greatly enhanced and is weakly dependent on temperature.

(iii) We have investigated the magnetic behaviour of a new hybrid material system consisting of a semiconductor InSe matrix and ferromagnetic Fe-inclusions. This system exhibits room temperature ferromagnetism; it has a large uniaxial magnetic anisotropy perpendicular to the plane of the vdW layers; and preserves the semiconducting properties of pristine InSe.

The main findings and prospects for further studies are discussed below.

8.1 Electron transport in InSe/graphene heterostructures

The electronic properties of atomically thin layers of vdW crystals can be modified by their combination with different 2D crystals.[28] This offers opportunities to explore different band structures and corresponding new physical phenomena. In this work, we have demonstrated how a capping layer of *n*-type InSe can enhance the electronic properties of CVD–grown graphene in an InSe/graphene field effect transistor. The favourable alignment of the band structure of the two crystals enables a transfer of electrons across the van der Waals interface between the InSe and graphene layers. This modulation doping of graphene is controlled by applying a gate voltage to the doped silicon substrate and leads to a 3-fold enhancement of the Hall mobility together with a giant $\nu = 2$ quantum Hall plateau, similar to that observed in graphene grown on SiC.[134,160-164] InSe/graphene therefore represents a novel heterostructure for exploring further the giant quantum Hall plateau phenomenon, with potential for metrological applications, and for future 2D technologies that exploit modulation doping and controlled charge transfer between the component layers of this type of vdW heterostructures. These results were published in *Physical Review Letters,* **119**, 157701 (2017).

8.2 Photosensing with InSe/graphene heterostructures

We have demonstrated that by mounting the InSe/graphene heterostructure on an oxidized silicon substrate, the electronic properties of the graphene layer can be controlled by a combination of optical excitation and field effect gating. In this way, the Fermi energy of the graphene layer can be fine-tuned across the Dirac point, thus achieving either *n*- or *p*-type conduction. The

light-induced charge transfer also induces a reversal of the sign of the Hall voltage and of the $\nu = 2$ quantum Hall plateau, which extends over a wide range of applied magnetic fields and temperatures. We have measured the carrier density in the InSe and graphene layers under optical excitation, suggesting the presence of a high density of donor states ($\sim 10^{11}$ cm^{-2}) in InSe. This new type of hybrid phototransistor combines the high photosensitivity of InSe with the unique electrical properties of graphene. These devices are made by a relatively simple fabrication process and offer a flexible route to integration with existing Si-manufacturing technologies. In particular, the broad-band absorption of InSe including a range of intraband and interband optical transitions in the visible, near-infrared and infrared range[17,37] provide an opportunity to tune the photoresponsivity of graphene and unlock its potential for optoelectronic applications, beyond the capability of traditional semiconductor devices and other 2D photodetectors in the current literature.[11,218-220] This work has been published in *Advanced Functional Materials*, **29**, 1805491 (2019).

8.3 Transition metals in InSe

Among the family of 2D materials, InSe has become a promising semiconductor due to its unique electronic and optical properties, including a high electron mobility[17,36] and strong photosensitivity.[29,35,195] Here we have shown that the incorporation of Fe-atoms during the Bridgman growth of InSe leads to the formation of crystalline triangular ferromagnetic Fe-islands. These induce a uniaxial internal magnetic field (~ 1 T) parallel to the *c*-axis of the InSe crystal. Also, the crystal preserves the semiconducting properties of pristine InSe. Thus, this hybrid system possesses both magnetic and semiconducting

properties. Our findings will stimulate further research on magnetism in novel semiconductor materials beyond conventional Si[221] and GaAs.[222] Since vdW crystals are compatible with other vdW crystals, magnetic metals, and dielectrics, we envisage further developments and a new class of devices that exploit the magnetic properties of hybrid magnetic-semiconducting materials. These results were published is *Advanced Science,* **5**, 1800257 (2018).

8.4 Outlook

In pursuing the project, new findings have emerged. Also, new questions have arisen. These have generated new ideas and opportunities for further developments, which are outlined in this section.

In our InSe/graphene FETs, the $\nu = 2$ extended Hall plateau in the Hall resistance R_{xy} was observed at relatively high temperatures, up to $T \sim 200$K. However, the measured value of R_{xy} departs from the quantised value $h/2e^2$ at high temperatures. This was assigned to the thermally activated parallel conduction in the InSe layer. To optimize the quantum Hall plateau and reduce the contribution of parallel conduction, one could explore new vdW heterostructures with a thin hBN tunnel barrier between InSe and graphene, *i.e.* an InSe/hBN/graphene heterostructure. In developing these new structures, one should consider that a hBN tunnel barrier between two graphene layers can increase the resistance of the graphene/hBN/graphene heterostructure by a factor of ~ 30 for each added layer of hBN.[65] Thus the addition of hBN could influence the charge transfer between InSe and graphene. This further development requires the fabrication of samples with different thicknesses of hBN and a study of effect of the hBN tunnel barrier on the charge transfer

mechanism. In addition to the magneto-transport measurements, the charge transfer could be examined by photoconductivity experiments.

The experimental transport studies of FETs in this thesis were mainly focussed on CVD grown graphene capped by InSe layers. However, capping of other types of graphene by InSe, *e.g.* epitaxial graphene on SiC or on hBN, could also enable the fabrication of devices with improved properties.

Owing to the unique optical properties of InSe[29,34] and compatibility with other vdW materials, it should also be possible to fabricate other complex structures and realise high-performance devices for practical applications.[223] For example, multi-layer light emitting diodes (LEDs) have been demonstrated by creating quantum well heterostructures where a TMDC layer is sandwiched between two insulating hBN layers.[224] In these structures, electrons and holes are electrically injected from two graphene layers into the TMDC and recombine radiatively, resulting in emission of photons. In a similar way, InSe layers could be employed to fabricate graphene/hBN/InSe/hBN/graphene LEDs. These might offer enhanced efficiency and broad tunable spectral selectivity due to the direct and widely tunable band gap of InSe.

Our findings on 2D magnetic layers could stimulate an interesting research path. The presence of a large uniaxial magnetic anisotropy and losses of spin angular momentum during the precession of the magnetization in the ferromagnetic Fe-islands into the non-magnetic InSe offer prospects for the generation of a charge current in InSe via the inverse spin Hall effect[202] and its control by the magnetic anisotropy of the crystal. This development requires the fabrication of devices with good electrical ohmic contacts to the InSe:Fe, which represents a challenge.

In the investigation of transition metal (TM) doped and intercalated InSe crystals, TM clusters were detected throughout the crystal. Thus the homogeneous incorporation of substitutional TM atoms in InSe remains to be addressed. Also, to construct nano-spintronic devices, it is necessary to examine the magnetic and semiconducting behaviour of atomically thin layers. This requires the development of sensitive probing techniques. Finally, it would be interesting to combine new magnetic 2D layers with graphene to induce magnetism in high mobility graphene. These structures have potential for future graphene-based spintronic applications.

In summary, InSe offers a new playground to explore low dimensional physical phenomena and could play an important role in future technological developments.

Bibliography

1 Moore, G. E. Cramming more components onto integrated circuits, Reprinted from Electronics, Vol. 38, April 19, 1965, pp. 114 ff. *IEEE Solid-State Circuits Society Newsletter* **11**, 33 (2006).

2 Iannaccone, G., Bonaccorso, F., Colombo, L. & Fiori, G. Quantum engineering of transistors based on 2D materials heterostructures. *Nat. Nanotechnol.* **13**, 183 (2018).

3 Novoselov, K. S. *et al.* Electric field effect in atomically thin carbon films. *Science* **306**, 666 (2004).

4 Neto, A. C., Guinea, F., Peres, N. M., Novoselov, K. S. & Geim, A. K. The electronic properties of graphene. *Rev. Mod. Phys.* **81**, 109 (2009).

5 Xia, F., Mueller, T., Lin, Y., Valdes-Garcia, A. & Avouris, P. Ultrafast graphene photodetector. *Nat. Nanotechnol.* **4**, 839 (2009).

6 Jariwala, D., Sangwan, V. K., Lauhon, L. J., Marks, T. J. & Hersam, M. C. Carbon nanomaterials for electronics, optoelectronics, photovoltaics, and sensing. *Chem. Soc. Rev.* **42**, 2824 (2013).

7 Lin, M. W. *et al.* Room-temperature high on/off ratio in suspended graphene nanoribbon field-effect transistors. *Nanotechnol.* **22**, 265201 (2011).

8 Li, X., Wang, X., Zhang, L., Lee, S. & Dai, H. Chemically derived, ultrasmooth graphene nanoribbon semiconductors. *Science* **319**, 1229 (2008).

9 Han, M. Y., Özyilmaz, B., Zhang, Y. & Kim, P. Energy band-gap engineering of graphene nanoribbons. *Phys. Rev. Lett.* **98**, 206805 (2007).

10 Geim, A. K. & Grigorieva, I. V. Van der Waals heterostructures. *Nature* **499**, 419 (2013).

11 Ferrari, A. C. *et al.* Science and technology roadmap for graphene, related two-dimensional crystals, and hybrid systems. *Nanoscale* **7**, 4598 (2015).

12 Ci, L. *et al.* Atomic layers of hybridized boron nitride and graphene domains. *Nat. Mater.* **9**, 430 (2010).

13 Yang, J. *et al.* Integer and Fractional Quantum Hall effect in Ultrahigh Quality Few-layer Black Phosphorus Transistors. *Nano Lett.* **18**, 229 (2018).

14 Wang, Q. H., Kalantar-Zadeh, K., Kis, A., Coleman, J. N. & Strano, M. S. Electronics and optoelectronics of two-dimensional transition metal dichalcogenides. *Nat. Nanotechnol.* **7**, 699 (2012).

15 Wang, K. *et al.* Electrical control of charged carriers and excitons in atomically thin materials. *Nat. Nanotechnol.* **13**, 128 (2018).

16 Brotons-Gisbert, M. *et al.* Nanotexturing to enhance photoluminescent response of atomically thin indium selenide with highly tunable band gap. *Nano Lett.* **16**, 3221 (2016).

17 Bandurin, D. A. *et al.* High electron mobility, quantum Hall effect and anomalous optical response in atomically thin InSe. *Nat. Nanotechnol.* **12**, 223 (2017).

18 Hamer, M. J. *et al.* Gate-defined quantum confinement in InSe-based van der Waals heterostructures. *Nano Lett.* **18**, 3950 (2018).

19 Jacobs-Gedrim, R. B. *et al.* Extraordinary photoresponse in two-dimensional In_2Se_3 nanosheets. *ACS Nano* **8**, 514 (2013).

20 Hu, P. A., Wen, Z., Wang, L., Tan, P. & Xiao, K. Synthesis of few-layer GaSe nanosheets for high performance photodetectors. *ACS Nano* **6**, 5988 (2012).

21 Mounet, N. *et al.* Two-dimensional materials from high-throughput computational exfoliation of experimentally known compounds. *Nat. Nanotechnol.* **13**, 246 (2018).

22 Ayari, A., Cobas, E., Ogundadegbe, O. & Fuhrer, M. S. Realization and electrical characterization of ultrathin crystals of layered transition-metal dichalcogenides. *J. Appl. Phys.* **101**, 014507 (2007).

23 Nicolosi, V., Chhowalla, M., Kanatzidis, M. G., Strano, M. S. & Coleman, J. N. Liquid exfoliation of layered materials. *Science* **340**, 1226419 (2013).

24 Zheng, J. *et al.* High yield exfoliation of two-dimensional chalcogenides using sodium naphthalenide. *Nat. Commun.* **5**, 2995 (2014).

25 Balakrishnan, N. *et al.* Engineering p–n junctions and bandgap tuning of InSe nanolayers by controlled oxidation. *2D Mater.* **4**, 025043 (2017).

26 Haigh, S. *et al.* Cross-sectional imaging of individual layers and buried interfaces of graphene-based heterostructures and superlattices. *Nat. Mater.* **11**, 764 (2012).

27 Dean, C. R. *et al.* Boron nitride substrates for high-quality graphene electronics. *Nat. Nanotechnol.* **5**, 722 (2010).

28 Novoselov, K. Nobel lecture: Graphene: Materials in the flatland. *Rev. Mod. Phys.* **83**, 837 (2011).

29 Mudd, G. W. *et al.* High broad-band photoresponsivity of mechanically formed InSe-graphene van der Waals heterostructures. *Adv. Mater.* **27**, 3760 (2015).

30 Jamet, M. *et al.* High-Curie-temperature ferromagnetism in self-organized $Ge_{1-x}Mn_x$ nanocolumns. *Nat. Mater.* **5**, 653 (2006).

31 Dietl, T. & Ohno, H. Dilute ferromagnetic semiconductors: Physics and spintronic structures. *Rev. Mod. Phys.* **86**, 187 (2014).

32 Ikeda, S. *et al.* A perpendicular-anisotropy CoFeB-MgO magnetic tunnel junction. *Nat. Mater.* **9**, 721 (2010).

33 Kress-Rogers, E., Nicholas, R. J., Portal, J. C. & Chevy, A. Cyclotron resonance studies on bulk and two-dimensional conduction electrons in InSe. *Sol. State Commun.* **44**, 379 (1982).

34 Mudd, G. W. *et al.* Tuning the bandgap of exfoliated InSe nanosheets by quantum confinement. *Adv. Mater.* **25**, 5714 (2013).

35 Tamalampudi, S. R. *et al.* High performance and bendable few-layered InSe photodetectors with broad spectral response. *Nano Lett.* **14**, 2800 (2014).

36 Feng, W., Zheng, W., Cao, W. & Hu, P. Back gated multilayer InSe transistors with enhanced carrier mobilities via the suppression of carrier scattering from a dielectric interface. *Adv. Mater.* **26**, 6587 (2014).

37 Mudd, G. W. *et al.* The direct-to-indirect band gap crossover in two-dimensional van der Waals Indium Selenide crystals. *Sci. Rep.* **6**, 39619 (2016).

38 Seixas, L., Rodin, A. S., Carvalho, A. & Neto, A. H. C. Multiferroic two-dimensional materials. *Phys. Rev. Lett.* **116**, 206803 (2016).

39 Chhowalla, M. *et al.* The chemistry of two-dimensional layered transition metal dichalcogenide nanosheets. *Nat. Chem.* **5**, 263 (2013).

40 Fiori, G. *et al.* Electronics based on two-dimensional materials. *Nat. Nanotechnol.* **9**, 768 (2014).

41 Jariwala, D., Sangwan, V. K., Lauhon, L. J., Marks, T. J. & Hersam, M. C. Emerging device applications for semiconducting two-dimensional transition metal dichalcogenides. *ACS Nano* **8**, 1102 (2014).

42 Zhang, H. Ultrathin two-dimensional nanomaterials. *ACS Nano* **9**, 9451 (2015).

43 Wallace, P. R. The band theory of graphite. *Phys. Rev.* **71**, 622 (1947).

44 Neto, A. H. C., Guinea, F., Peres, N. M. R., Novoselov, K. S. & Geim, A. K. The electronic properties of graphene. *Rev. Mod. Phys.* **81**, 109 (2009).

45 Saito, R., Dresselhaus, G. & Dresselhaus, M. S. *Physical properties of carbon nanotubes*. (World Scientific, 1998).

46 Geim, A. K. & Novoselov, K. S. in *Nanoscience and Technology: A Collection of Reviews from Nature Journals.* (World Scientific, 2010).

47 Zhu, Y. *et al.* Graphene and graphene oxide: synthesis, properties, and applications. *Adv. Mater.* **22**, 3906 (2010).

48 Wang, L. *et al.* One-dimensional electrical contact to a two-dimensional material. *Science* **342**, 614 (2013).

49 Chen, J.-H., Jang, C., Xiao, S., Ishigami, M. & Fuhrer, M. S. Intrinsic and extrinsic performance limits of graphene devices on SiO_2. *Nat. Nanotechnol.* **3**, 206 (2008).

50 Du, X., Skachko, I., Barker, A. & Andrei, E. Y. Approaching ballistic transport in suspended graphene. *Nat. Nanotechnol.* **3**, 491 (2008).

51 Betz, A. C. *et al.* Supercollision cooling in undoped graphene. *Nat. Phys.* **9**, 109 (2013).

52 Zhang, Y., Brar, V. W., Girit, C., Zettl, A. & Crommie, M. F. Origin of spatial charge inhomogeneity in graphene. *Nat. Phys.* **5**, 722 (2009).

53 Hwang, E., Adam, S. & Sarma, S. D. Carrier transport in two-dimensional graphene layers. *Phys. Rev. Lett.* **98**, 186806 (2007).

54 Chen, J.-H. *et al.* Charged-impurity scattering in graphene. *Nat. Phys.* **4**, 377 (2008).

55 Hwang, E. H. & Sarma, S. D. Acoustic phonon scattering limited carrier mobility in two-dimensional extrinsic graphene. *Phys. Rev. B* **77**, 115449 (2008).

56 Ponomarenko, L. A. *et al.* Effect of a high-κ environment on charge carrier mobility in graphene. *Phys. Rev. Lett.* **102**, 206603 (2009).

57 Gorbachev, R. V. *et al.* Hunting for monolayer boron nitride: optical and Raman signatures. *Small* **7**, 465 (2011).

58 Decker, R. *et al.* Local electronic properties of graphene on a BN substrate via scanning tunneling microscopy. *Nano Lett.* **11**, 2291 (2011).

59 Xue, J. *et al.* Scanning tunnelling microscopy and spectroscopy of ultra-flat graphene on hexagonal boron nitride. *Nat. Mater.* **10**, 282 (2011).

60 Ju, L. *et al.* Photoinduced doping in heterostructures of graphene and boron nitride. *Nat. Nanotechnol.* **9**, 348 (2014).

61 Novoselov, K. S., Mishchenko, A., Carvalho, A. & Neto, A. H. C. 2D materials and van der Waals heterostructures. *Science* **353**, aac9439 (2016).

62 Watanabe, K., Taniguchi, T. & Kanda, H. Direct-bandgap properties and evidence for ultraviolet lasing of hexagonal boron nitride single crystal. *Nat. Mater.* **3**, 404 (2004).

63 Song, L. *et al.* Large scale growth and characterization of atomic hexagonal boron nitride layers. *Nano Lett.* **10**, 3209 (2010).

64 Cao, Y. *et al.* Quality heterostructures from two-dimensional crystals unstable in air by their assembly in inert atmosphere. *Nano Lett.* **15**, 4914 (2015).

65 Britnell, L. *et al.* Electron tunneling through ultrathin boron nitride crystalline barriers. *Nano Lett.* **12**, 1707 (2012).

66 Britnell, L. *et al.* Resonant tunnelling and negative differential conductance in graphene transistors. *Nat. Commun.* **4**, 1794 (2013).

67 Britnell, L. *et al.* Field-effect tunneling transistor based on vertical graphene heterostructures. *Science* **335**, 947 (2012).

68 Ikari, T., Shigetomi, S. & Hashimoto, K. Crystal structure and Raman spectra of InSe. *Phys. Status Solidi B* **111**, 477-481 (1982).

69 Mancini, A. M., Micocci, G. & Rizzo, A. New materials for optoelectronic devices: Growth and characterization of indium and gallium chalcogenide layer compounds. *Mater. Chem. Phys.* **9**, 29 (1983).

70 Debbichi, L., Eriksson, O. & Lebègue, S. Two-dimensional indium selenides compounds: An ab initio study. *J. Phys. Chem. Lett.* **6**, 3098 (2015).

71 Han, G., Chen, Z. G., Drennan, J. & Zou, J. Indium selenides: structural characteristics, synthesis and their thermoelectric performances. *Small* **10**, 2747 (2014).

72 Kuhn, A., Chevy, A. & Chevalier, R. Crystal structure and interatomic distances in GaSe. *Phys. Status Solidi A* **31**, 469 (1975).

73 Segura, A., Guesdon, J. P., Besson, J. M. & Chevy, A. Photoconductivity and photovoltaic effect in indium selenide. *J. Appl. Phys.* **54**, 876 (1983).

74 Martínez-Pastor, J., Segura, A., Valdes, J. L. & Chevy, A. Electrical and photovoltaic properties of indium-tin-oxide/p-InSe/Au solar cells. *J. Appl. Phys.* **62**, 1477 (1987).

75 Segura, A., Chevy, A., Guesdon, J. P. & Besson, J. M. Photovoltaic efficiency of InSe solar cells. *Sol. Energy Mater.* **2**, 159 (1979).

76 Segura, A., Guesdon, J. P., Besson, J. M. & Chevy, A. Photovoltaic effect in InSe-Application to Solar Energy Conversion. *Rev. Phys. Appliquée* **14**, 253 (1979).

77 Bringuier, E., Bourdon, A., Piccioli, N. & Chevy, A. Optical second-harmonic generation in lossy media: Application to GaSe and InSe. *Phys. Rev. B* **49**, 16971 (1994).

78 Sánchez-Royo, J. F., Segura, A. & Muñoz, V. Anisotropy of the refractive index and absorption coefficient in the layer plane of gallium telluride single crystals. *Phys. Status Solidi A* **151**, 257 (1995).

79 Ferrer-Roca, C., Bouvier, J., Segura, A., Andrés, M. V. & Muñoz, V. Light-induced transmission nonlinearities in gallium selenide. *J. Appl. Phys.* **85**, 3780 (1999).

80 Allakhverdiev, K. R., Yetis, M. Ö., Özbek, S., Baykara, T. K. & Salaev, E. Y. u. Effective nonlinear GaSe crystal. Optical properties and applications. *Laser Phys.* **19**, 1092 (2009).

81 Segura, A., Bouvier, J., Andrés, M. V., Manjón, F. J. & Munoz, V. Strong optical nonlinearities in gallium and indium selenides related to inter-valence-band transitions induced by light pulses. *Phys. Rev. B* **56**, 4075 (1997).

82 Shi, W., Ding, Y. J., Fernelius, N. & Vodopyanov, K. Efficient, tunable, and coherent 0.18–5.27-THz source based on GaSe crystal. *Opt. Lett.* **27**, 1454 (2002).

83 Kübler, C., Huber, R., Tübel, S. & Leitenstorfer, A. Ultrabroadband detection of multi-terahertz field transients with GaSe electro-optic sensors: Approaching the near infrared. *Appl. Phys. Lett.* **85**, 3360 (2004).

84 Buscema, M. *et al.* Photocurrent generation with two-dimensional van der Waals semiconductors. *Chem. Soc. Rev.* **44**, 3691 (2015).

85 Liu, F. *et al.* High-sensitivity photodetectors based on multilayer GaTe flakes. *ACS Nano* **8**, 752 (2014).

86 Hu, P. A. *et al.* Highly responsive ultrathin GaS nanosheet photodetectors on rigid and flexible substrates. *Nano Lett.* **13**, 1649 (2013).

87 Katerinchuk, V. N. & Kovalyuk, M. Z. InSe p-n Homojunction Diodes. *Phys. Status Solidi A* **133**, K45 (1992).

88 Millot, M., Broto, J.-M., George, S., González, J. & Segura, A. Electronic structure of indium selenide probed by magnetoabsorption spectroscopy under high pressure. *Phys. Rev. B* **81**, 205211 (2010).

89 Kovalyuk, Z. D., Katerinchuk, V. N. & Betsa, T. V. Photoresponse spectral investigations for anisotropic semiconductor InSe. *Opt. Mater.* **17**, 279 (2001).

90 Dmitriev, A. I. *et al.* Investigation of the morphology of the van der Waals surface of the InSe single crystal. *Phys. Solid State* **53**, 622 (2011).

91 Volykhov, A. A. *et al.* Study of the atomically clean InSe (0001) surface by X-ray photoelectron spectroscopy. *Russ. Microelectron.* **41**, 521 (2012).

92 Madelung, O., Rössler, U. & Schulz, M. Non-tetrahedrally bonded elements and binary compounds I. *Springer Berlin Heidelberg* **3** (1998).

93 Sánchez-Royo, J. F. *et al.* Electronic structure, optical properties, and lattice dynamics in atomically thin indium selenide flakes. *Nano Research* **7**, 1556 (2014).

94 Lei, S. *et al.* Evolution of the electronic band structure and efficient photo-detection in atomic layers of InSe. *ACS Nano* **8**, 1263 (2014).

95 Zólyomi, V., Drummond, N. D. & Fal'Ko, V. I. Electrons and phonons in single layers of hexagonal indium chalcogenides from ab initio calculations. *Phys. Rev. B* **89**, 205416 (2014).

96 Rasmussen, F. A. & Thygesen, K. S. Computational 2D materials database: electronic structure of transition-metal dichalcogenides and oxides. *J. Phys. Chem. C* **119**, 13169 (2015).

97 Mudd, G. W. *et al.* Quantum confined acceptors and donors in InSe nanosheets. *Appl. Phys. Lett.* **105**, 221909 (2014).

98 Cui, X. *et al.* Multi-terminal transport measurements of MoS_2 using a van der Waals heterostructure device platform. *Nat. Nanotechnol.* **10**, 534 (2015).

99 Wu, Z. *et al.* Even–odd layer-dependent magnetotransport of high-mobility Q-valley electrons in transition metal disulfides. *Nat. Commun.* **7**, 12955 (2016).

100 Mak, K. F., Lee, C., Hone, J., Shan, J. & Heinz, T. F. Atomically thin MoS_2: a new direct-gap semiconductor. *Phys. Rev. Lett.* **105**, 136805 (2010).

101 Tongay, S. *et al.* Thermally driven crossover from indirect toward direct bandgap in 2D semiconductors: $MoSe_2$ versus MoS_2. *Nano Lett.* **12**, 5576 (2012).

102 Zhao, W. *et al.* Evolution of electronic structure in atomically thin sheets of WS_2 and WSe_2. *ACS Nano* **7**, 791 (2012).

103 Lopez-Sanchez, O., Lembke, D., Kayci, M., Radenovic, A. & Kis, A. Ultrasensitive photodetectors based on monolayer MoS_2. *Nat. Nanotechnol.* **8**, 497 (2013).

104 Zhu, Z. Y., Cheng, Y. C. & Schwingenschlögl, U. Giant spin-orbit-induced spin splitting in two-dimensional transition-metal dichalcogenide semiconductors. *Phys. Rev. B* **84**, 153402 (2011).

105 Xiao, D., Liu, G.-B., Feng, W., Xu, X. & Yao, W. Coupled spin and valley physics in monolayers of MoS_2 and other group-VI dichalcogenides. *Phys. Rev. Lett.* **108**, 196802 (2012).

106 Zeng, H., Dai, J., Yao, W., Xiao, D. & Cui, X. Valley polarization in MoS_2 monolayers by optical pumping. *Nat. Nanotechnol.* **7**, 490 (2012).

107 Shan, W.-Y., Lu, H.-Z. & Xiao, D. Spin hall effect in spin-valley coupled monolayers of transition metal dichalcogenides. *Phys. Rev. B* **88**, 125301 (2013).

108 Suzuki, R. *et al.* Valley-dependent spin polarization in bulk MoS_2 with broken inversion symmetry. *Nat. Nanotechnol.* **9**, 611 (2014).

109 Mak, K. F., McGill, K. L., Park, J. & McEuen, P. L. The valley Hall effect in MoS_2 transistors. *Science* **344**, 1489 (2014).

110 Mak, K. F., He, K., Shan, J. & Heinz, T. F. Control of valley polarization in monolayer MoS_2 by optical helicity. *Nat. Nanotechnol.* **7**, 494 (2012).

111 Novoselov, K. S. *et al.* Two-dimensional atomic crystals. *Proc. Natl. Acad. Sci. U.S.A.* **102**, 10451 (2005).

112 Radisavljevic, B. & Kis, A. Mobility engineering and a metal–insulator transition in monolayer MoS_2. *Nat. Mater.* **12**, 815 (2013).

113 Fallahazad, B. *et al.* Shubnikov–de Haas oscillations of high-mobility holes in monolayer and bilayer WSe_2: Landau level degeneracy, effective mass, and negative compressibility. *Phys. Rev. Lett.* **116**, 086601 (2016).

114 Xu, S. *et al.* Universal low-temperature Ohmic contacts for quantum transport in transition metal dichalcogenides. *2D Mater.* **3**, 021007 (2016).

115 Qiao, J., Kong, X., Hu, Z.-X., Yang, F. & Ji, W. High-mobility transport anisotropy and linear dichroism in few-layer black phosphorus. *Nat. Commun.* **5**, 4475 (2014).

116 Liu, H. *et al.* Phosphorene: an unexplored 2D semiconductor with a high hole mobility. *ACS Nano* **8**, 4033 (2014).

117 Tayari, V. *et al.* Two-dimensional magnetotransport in a black phosphorus naked quantum well. *Nat. Commun.* **6**, 7702 (2015).

118 Li, L. *et al.* Quantum oscillations in a two-dimensional electron gas in black phosphorus thin films. *Nat. Nanotechnol.* **10**, 608 (2015).

119 Gillgren, N. *et al.* Gate tunable quantum oscillations in air-stable and high mobility few-layer phosphorene heterostructures. *2D Mater.* **2**, 011001 (2014).

120 Li, X. *et al.* Strain modulations of magnetism in Fe-doped InSe monolayer. *Physica E* **94**, 153 (2017).

121 Li, X., Xia, C., Du, J. & Xiong, W. Magnetism induced by 3d transition metal atom doping in InSe monolayer. *J. Mater. Sci.* **53**, 3500 (2018).

122 Wang, T., Li, J., Jin, H. & Wei, Y. Tuning the electronic and magnetic properties of InSe nanosheets by transition metal doping. *Phys. Chem. Chem. Phys.* **20**, 7532 (2018).

123 Fu, Z. *et al.* Tuning the Physical and Chemical Properties of 2D InSe with Interstitial Boron Doping: A First-Principles Study. *J. Phys. Chem. C* **121**, 28312 (2017).

124 Carteaux, V., Moussa, F. & Spiesser, M. 2d Ising-like ferromagnetic behaviour for the lamellar $Cr_2Si_2Te_6$ compound: a neutron scattering investigation. *Europhy. Lett.* **29**, 251 (1995).

125 Carteaux, V., Ouvrard, G., Grenier, J. C. & Laligant, Y. Magnetic structure of the new layered ferromagnetic chromium hexatellurosilicate $Cr_2Si_2Te_6$. *J. Magn. Magn. Mater.* **94**, 127 (1991).

126 Li, X. & Yang, J. $CrXTe_3$ (X= Si, Ge) nanosheets: two dimensional intrinsic ferromagnetic semiconductors. *J. Mater. Chem. C* **2**, 7071 (2014).

127 Lin, M.-W. *et al.* Ultrathin nanosheets of $CrSiTe_3$: a semiconducting two-dimensional ferromagnetic material. *J. Mater. Chem. C* **4**, 315 (2016).

128 Zacharia, R., Ulbricht, H. & Hertel, T. Interlayer cohesive energy of graphite from thermal desorption of polyaromatic hydrocarbons. *Phys. Rev. B* **69**, 155406 (2004).

129 Shi, X. *et al.* Introducing Magnetism into 2D Nonmagnetic Inorganic Layered Crystals: A Brief Review from First-Principles Aspects. *Crystals* **8**, 24 (2018).

130 Dillon Jr, J. F. & Olson, C. E. Magnetization, resonance, and optical properties of the ferromagnet CrI3. *J. Appl. Phys.* **36**, 1259 (1965).

131 Hansen, W. N. Some Magnetic Properties of the Chromium (III) Halides at 4.2 °K. *J. Appl. Phys.* **30**, 304S (1959).

132 McGuire, M. A., Dixit, H., Cooper, V. R. & Sales, B. C. Coupling of crystal structure and magnetism in the layered, ferromagnetic insulator CrI_3. *Chem. Mater.* **27**, 612 (2015).

133 Huang, B. *et al.* Layer-dependent ferromagnetism in a van der Waals crystal down to the monolayer limit. *Nature* **546**, 270 (2017).

134 Janssen, T. J. B. M., Tzalenchuk, A., Lara-Avila, S., Kubatkin, S. & Fal'ko, V. I. Quantum resistance metrology using graphene. *Rep. Prog. Phys.* **76**, 104501 (2013).

135 Klitzing, K. V., Dorda, G. & Pepper, M. New method for high-accuracy determination of the fine-structure constant based on quantized Hall resistance. *Phys. Rev. Lett.* **45**, 494 (1980).

136 Poirier, W. & Schopfer, F. Resistance metrology based on the quantum Hall effect. *Eur. Phys. J. Spec. Top.* **172**, 207 (2009).

137 Landau, L. D. & Lifshitz, E. M. *Quantum Mechanics: Non-relativistic Theory*. (Oxford: Pergamon, 1981).

138 Tsui, D. C., Stormer, H. L. & Gossard, A. C. Two-dimensional magnetotransport in the extreme quantum limit. *Phys. Rev. Lett.* **48**, 1559 (1982).

139 Goerbig, M. O. Electronic properties of graphene in a strong magnetic field. *Rev. Mod. Phys.* **83**, 1193 (2011).

140 Zheng, Y. & Ando, T. Hall conductivity of a two-dimensional graphite system. *Phys. Rev. B* **65**, 245420 (2002).

141 Zhang, Y., Tan, Y.-W., Stormer, H. L. & Kim, P. Experimental observation of the quantum Hall effect and Berry's phase in graphene. *Nature* **438**, 201 (2005).

142 Gusynin, V. & Sharapov, S. Magnetic oscillations in planar systems with the Dirac-like spectrum of quasiparticle excitations. II. Transport properties. *Phys. Rev. B* **71**, 125124 (2005).

143 Novoselov, K. S. *et al.* Two-dimensional gas of massless Dirac fermions in graphene. *Nature* **438**, 197 (2005).

144 Janssen, T. J. B. M. *et al.* Precision comparison of the quantum Hall effect in graphene and gallium arsenide. *Metro.* **49**, 294 (2012).

145 Cage, M. E. *et al.* Dissipation and dynamic nonlinear behavior in the quantum Hall regime. *Phys. Rev. Lett.* **51**, 1374 (1983).

146 Ebert, G., Von Klitzing, K., Ploog, K. & Weinmann, G. Two-dimensional magneto-quantum transport on GaAs-$Al_xGa_{1-x}As$ heterostructures under non-ohmic conditions. *J. Phys. C: Sol. State Phys.* **16**, 5441 (1983).

147 Jeckelmann, B. & Jeanneret, B. The quantum Hall effect as an electrical resistance standard. *Rep. Prog. Phys.* **64**, 1603 (2001).

148 Haug, R. J. Edge-state transport and its experimental consequences in high magnetic fields. *Semicond. Sci. Technol.* **8**, 131 (1993).

149 Büttiker, M. Absence of backscattering in the quantum Hall effect in multiprobe conductors. *Phys. Rev. B* **38**, 9375 (1988).

150 Nachtwei, G. Breakdown of the quantum Hall effect. *Physica E: Low Dimens. Syst. Nanostruct.* **4**, 79 (1999).

151 Streda, P. & Von Klitzing, K. Critical non-dissipative current of quantum Hall regime. *J. Phys. C: Sol. State Phys.* **17**, L483 (1984).

152 Komiyama, S., Takamasu, T., Hiyamizu, S. & Sasa, S. Breakdown of the quantum Hall effect due to electron heating. *Sol. State Commun.* **54**, 479 (1985).

153 Eaves, L. & Sheard, F. W. Size-dependent quantised breakdown of the dissipationless quantum Hall effect in narrow channels. *Semicond. Sci. Technol.* **1**, 346 (1986).

154 Komiyama, S. & Kawaguchi, Y. Heat instability of quantum Hall conductors. *Phys. Rev. B* **61**, 2014 (2000).

155 Eaves, L. Quantum Hall effect breakdown steps: evidence for an instability induced by inter-Landau level scattering. *Physica B* **298**, 1 (2001).

156 Baker, A. M. R., Alexander-Webber, J. A., Altebaeumer, T. & Nicholas, R. Energy relaxation for hot Dirac fermions in graphene and breakdown of the quantum Hall effect. *Phys. Rev. B* **85**, 115403 (2012).

157 Baker, A. M. R. *et al.* Energy loss rates of hot Dirac fermions in epitaxial, exfoliated, and CVD graphene. *Phys. Rev. B* **87**, 045414 (2013).

158 Alexander-Webber, J. A. *et al.* Phase space for the breakdown of the quantum Hall effect in epitaxial graphene. *Phys. Rev. Lett.* **111**, 096601 (2013).

159 Janssen, T. J. B. M. *et al.* Anomalously strong pinning of the filling factor ν= 2 in epitaxial graphene. *Phys. Rev. B* **83**, 233402 (2011).

160 Tzalenchuk, A. *et al.* Towards a quantum resistance standard based on epitaxial graphene. *Nat. Nanotechnol.* **5**, 186 (2010).

161 Janssen, T. J. B. M. *et al.* Operation of graphene quantum Hall resistance standard in a cryogen-free table-top system. *2D Mater.* **2**, 035015 (2015).

162 Kopylov, S., Tzalenchuk, A., Kubatkin, S. & Fal'ko, V. I. Charge transfer between epitaxial graphene and silicon carbide. *Appl. Phys. Lett.* **97**, 1121091 (2010).

163 Ribeiro-Palau, R. *et al.* Quantum Hall resistance standard in graphene devices under relaxed experimental conditions. *Nat. Nanotechnol.* **10**, 965 (2015).

164 Alexander-Webber, J. A. *et al.* Giant quantum Hall plateaus generated by charge transfer in epitaxial graphene. *Sci. Rep.* **6**, 30296 (2016).

165 Blundell, S. *Magnetism in condensed matter*. (Oxford University Press, 2001).

166 Cullity, B. D. & Graham, C. D. *Introduction to magnetic materials*. (John Wiley & Sons, 2011).

167 Kittel, C. *Introduction to solid state physics*. Vol. 8 (Wiley New York, 1976).

168 Kittel, C. Physical theory of ferromagnetic domains. *Rev. Mod. Phys.* **21**, 541 (1949).

169 Ashcroft, N. W. & Mermin, N. D. Solid state physics (Brooks Cole, 1976). *Google Scholar* (2008).

170 Callister, W. D. & Rethwisch, D. G. *Materials science and engineering*. Vol. 5 (John Wiley & Sons NY, 2011).

171 Gilbert, T. L. A phenomenological theory of damping in ferromagnetic materials. *IEEE Trans. Mag.* **40**, 3443 (2004).

172 Lenz, K. *et al.* Two-magnon scattering and viscous Gilbert damping in ultrathin ferromagnets. *Phys. Rev. B* **73**, 144424 (2006).

173 Woltersdorf, G., Buess, M., Heinrich, B. & Back, C. H. Time resolved magnetization dynamics of ultrathin Fe (001) films: spin-pumping and two-magnon scattering. *Phys. Rev. Lett.* **95**, 037401 (2005).

174 Eaton, G. R., Eaton, S. S., Barr, D. P. & Weber, R. T. *Quantitative EPR*. (Springer, 2010).

175 Buschow, K. H. J. & Boer, F. R. *Physics of magnetism and magnetic materials*. Vol. 92 (Springer, 2003).

176 Koksharov, Y. A. *et al.* Electron paramagnetic resonance of ferrite nanoparticles. *J. Appl. Phys.* **89**, 2293 (2001).

177 Ishii, T. High quality single crystal growth of layered InSe semiconductor by Bridgman technique. *J. Cryst. Growth* **89**, 459 (1988).

178 Boledzyuk, V. *et al.* Preparation of Nanocomposite Magnetic Compounds Based on Layered Semiconductors by Means of Electrochemical Intercalation in a Gradient Magnetic Field. *Acta Phys. Pol., A* **130**, 773 (2016).

179 Patane, A. & Balkan, N. *Semiconductor Research: Experimental Techniques*. Vol. 150 (Springer, 2012).

180 Martin, Y. & Wickramasinghe, H. K. Magnetic imaging by force microscopy with 1000 Å resolution. *Appl. Phys. Lett.* **50**, 1455 (1987).

181 Puttock, R. *et al.* V-shaped domain wall probes for calibrated magnetic force microscopy. *IEEE T. Magn.* **53**, 1 (2017).

182 Turyanska, L., Makarovsky, O., Eaves, L., Patanè, A. & Mori, N. Mobility enhancement of CVD graphene by spatially correlated charges. *2D Mater.* **4**, 025026 (2017).

183 Starnberg, H. & Brauer, H. *Electron Spectroscopies Applied to Low-Dimensional Materials ed HP Hughes and HI Starnberg*. (Kluwer Academic Dordrecht, 2000).

184 Adam, S., Hwang, E. H., Galitski, V. M. & Sarma, S. D. A self-consistent theory for graphene transport. *Proc. Natl. Acad. Sci. U.S.A.* **104**, 18392 (2007).

185 Reed, M., Kirk, W. & Kobiela, P. Investigation of parallel conduction in GaAs/$Al_xGa_{1-x}As$ modulation-doped structures in the quantum limit. *IEEE J. Quantum Electronics* **22**, 1753 (1986).

186 Zhou, S., Liu, C.-C., Zhao, J. & Yao, Y. Monolayer group-III monochalcogenides by oxygen functionalization: a promising class of two-dimensional topological insulators. *npj Quantum Materials* **3**, 16 (2018).

187 Novoselov, K. S. *et al.* Room-temperature quantum Hall effect in graphene. *Science* **315**, 1379-1379 (2007).

188 Misiorny, M., Hell, M. & Wegewijs, M. R. Spintronic magnetic anisotropy. *Nat. Phys.* **9**, 801 (2013).

189 Sun, S., Murray, C. B., Weller, D., Folks, L. & Moser, A. Monodisperse FePt nanoparticles and ferromagnetic FePt nanocrystal superlattices. *Science* **287**, 1989 (2000).

190 Goodwin, C. A., Ortu, F., Reta, D., Chilton, N. F. & Mills, D. P. Molecular magnetic hysteresis at 60 kelvin in dysprosocenium. *Nature* **548**, 439 (2017).

191 Donati, F. *et al.* Magnetic remanence in single atoms. *Science* **352**, 318 (2016).

192 Tserkovnyak, Y., Brataas, A. & Bauer, G. E. Enhanced Gilbert damping in thin ferromagnetic films. *Phys. Rev. Lett.* **88**, 117601 (2002).

193 Abufager, P. N., Robles, R. & Lorente, N. $FeCoCp_3$ molecular magnets as spin filters. *J. Phys. Chem. C* **119**, 12119 (2015).

194 Kawakami, R. K. Spin amplification by controlled symmetry breaking for spin-based logic. *2D Mater.* **2**, 034001 (2015).

195 Lei, S. *et al.* Optoelectronic memory using two-dimensional materials. *Nano Lett.* **15**, 259 (2015).

196 Kress-Rogers, E., Nicholas, R. J., Portal, J. C. & Chevy, A. Cyclotron resonance studies on bulk and two-dimensional conduction electrons in InSe. *Sol. State Commun.* **44**, 379 (1982).

197 Manjón, F. J. *et al.* Band structure of indium selenide investigated by intrinsic photoluminescence under high pressure. *Phys. Rev. B* **70**, 125201 (2004).

198 Pilbrow, J. *Transition ion electron paramagnetic resonance*, *Clarendon*. (Oxford, 1990).

199 Belmeguenai, M. *et al.* Temperature dependence of magnetic properties of $La_{0.7}Sr_{0.3}MnO_3/SrTiO_3$ thin films on silicon substrates. *Phys. Rev. B* **81**, 054410 (2010).

200 Butera, A., Zhou, J. N. & Barnard, J. A. Ferromagnetic resonance in as-deposited and annealed Fe-SiO_2 heterogeneous thin films. *Phys. Rev. B* **60**, 12270 (1999).

201 Zakeri, K. *et al.* Spin dynamics in ferromagnets: Gilbert damping and two-magnon scattering. *Phys. Rev. B* **76**, 104416 (2007).

202 Zhao, H., Loren, E. J., Van Driel, H. & Smirl, A. L. Coherence control of Hall charge and spin currents. *Phys. Rev. Lett.* **96**, 246601 (2006).

203 Keune, W., Halbauer, R., Gonser, U., Lauer, J. & Williamson, D. L. Antiferromagnetism of fcc Fe thin films. *J. Magn. Magn. Mater.* **6**, 192 (1977).

204 Halbauer, R. & Gonser, U. Antiferromagnetism of fcc iron films. *J. Magn. Magn. Mater.* **35**, 55 (1983).

205 Hines, W. A. *et al.* Magnetic and structural study of fcc γ-Fe precipitates in Cu. *Phys. Status Solidi B* **246**, 2154 (2009).

206 Gonser, U., Meechan, C. J., Muir, A. H. & Wiedersich, H. Determination of Néel temperatures in fcc iron. *J. Appl. Phys.* **34**, 2373 (1963).

207 Gradmann, U., Kümmerle, W. & Tillmanns, P. Epitaxial growth and ferromagnetic order of fcc iron films on (111) Cu. *Thin Solid Films* **34**, 249 (1976).

208 Pinski, F. J., Staunton, J., Gyorffy, B. L., Johnson, D. D. & Stocks, G. M. Ferromagnetism versus antiferromagnetism in face-centered-cubic iron. *Phys. Rev. Lett.* **56**, 2096 (1986).

209 Fu, C. L. & Freeman, A. J. Electronic and magnetic properties of the fcc Fe (001) thin films: Fe/Cu (001) and Cu/Fe/Cu (001). *Phys. Rev. B* **35**, 925 (1987).

210 Gerhard, L. *et al.* Magnetoelectric coupling at metal surfaces. *Nat. Nanotechnol.* **5**, 792 (2010).

211 Rado, G. T. & Suhl, H. *Magnetism: A treatise on modern theory and materials*. (Elsevier, 1963).

212 Maxwell, L. R. & McGuire, T. R. Antiferromagnetic resonance. *Rev. Mod. Phys.* **25**, 279 (1953).

213 Kittel, C. Theory of antiferromagnetic resonance. *Phys. Rev.* **82**, 565 (1951).

214 Seidel, G. & Keesom, P. Specific heat of gallium and zinc in the normal and superconducting states. *Phys. Rev.* **112**, 1083 (1958).

215 Shaw, R. W., Mapother, D. E. & Hopkins, D. C. Critical fields of superconducting tin, indium, and tantalum. *Phys. Rev.* **120**, 88 (1960).

216 Eisenstein, J. Superconducting elements. *Rev. Mod. Phys.* **26**, 277 (1954).

217 El-Sayed, K., Heiba, Z., Sedeek, K. & Hantour, H. Magnetic, electric and crystallographic properties of diluted magnetic $InSe_{(1-x)}Fe(Co)_x$ semiconductor. *J. Alloys Compd.* **530**, 102 (2012).

218 Koppens, F. *et al.* Photodetectors based on graphene, other two-dimensional materials and hybrid systems. *Nat. Nanotechnol.* **9**, 780 (2014).

219 Yan, F. *et al.* Fast, multicolor photodetection with graphene-contacted p-GaSe/n-InSe van der Waals heterostructures. *Nanotechnol* **28**, 27LT01 (2017).

220 Goossens, S. *et al.* Broadband image sensor array based on graphene–CMOS integration. *Nat. Photonics* **11**, 366 (2017).

221 Ando, K. & Saitoh, E. Observation of the inverse spin Hall effect in silicon. *Nat. Commun.* **3**, 629 (2012).

222 Chen, L., Matsukura, F. & Ohno, H. Direct-current voltages in (Ga, Mn) As structures induced by ferromagnetic resonance. *Nat. Commun.* **4**, 2055 (2013).

223 Geim, A. K. & Grigorieva, I. V. Van der Waals heterostructures. *Nature* **499**, 419 (2013).

224 Withers, F. *et al.* Light-emitting diodes by band-structure engineering in van der Waals heterostructures. *Nat. Mater.* **14**, 301 (2015).